



MONASH University

Defect Identification on The Underside of a Flat Plate using Moving Heat Source

YI CHIN TAN

This thesis is submitted in the fulfilment of the requirements for the degree of

Masters in Engineering Science (Research)

May 2016

Copyright Notice

© Yi Chin Tan (2016). Except as provided in the Copyright Act 1968, this thesis may not be reproduced in any form without the written permission of the author.

I certify that I have made all reasonable efforts to secure copyright permissions for third-party content included in this thesis and have not knowingly added copyright content to my work without the owner's permission.

Abstract

The causes of rail line accidents are apparent over the years, and there is a need to address this situation. One of the common factors is the lack of knowledge on rail base defects. Current technologies and methodologies on the inspection of rail track health are limited, and often require extended hours of inspection and labour effort. To enhance the detectability and efficiency of defect detection on rail systems, a heat source mounted on a moving platform was proposed and tested with computational modelling.

A flat plate model with underside defect was used for the investigation to simulate and represent a complex rail base structure. The presence of defects was determined by analysing surface temperature responses. The second order peak derivative method estimated the defect depth while the Full Width Half Maximum (FWHM) method predicted the actual size of the defect located at the underside of test plate.

The results on stationary heating showed that the prediction of underside defect size and depth location were most accurate when investigating for a case where a large size defect is positioned near the inspection surface. When defect depth is increased, this prediction ability deteriorates. For a defect at 7 mm depth, the predicted defect size is not justified. The results on stationary test were used as a reference for moving heat source test. The moving heat source was set up by creating sequential stationary heating of small segments separated by a constant delay. It was found that when this time delay was removed, the prediction of defect depth and size was similar to the test results on stationary heating. In fact, due to the high-speed heating, lateral heat diffusion can be assumed negligible, resulting in similar outcome as stationary test. The minimum heating speed for this to be true is 18km/hr. The tests in this thesis were validated with mathematical model and previously established findings.

Edge effects are one of the main factors in affecting the prediction accuracy of defect size and depth location. A small defect size will experience earlier occurrence and significant edge effect whereas a large defect size will behave oppositely. In this study, other factors such as maximum achievable temperature and temperature contrast were also considered.

The use of high-speed moving heat source for defect detection and measurement is feasible given that it is approximated to stationary heating. It allows the moving heat source test method to determine minimum detectable defect size and maximum detectable defect depth.

Declaration

This thesis contains no material which has been accepted for the award of any other degree or diploma at any university or equivalent institution and that, to the best of my knowledge and belief, this thesis contains no material previously published or written by another person, except where due reference is made in the text of the thesis.

Signed: _____

Date: _____

Acknowledgements

I would like to thank my thesis supervisor Professor Wing Kong Chiu of the Department of Mechanical & Aerospace Engineering at Monash University, for his guidance throughout the course of completing this thesis. He has been very supportive and constantly providing advices in terms of research directions whenever I needed help. Not to also mention that his knowledge and insight has been very helpful in achieving the research objective.

I would also like to express appreciation to my fellow peers who has been encouraging over the past years. They have provided valuable assistance and feedback on my journey to completing this thesis.

I am very grateful to the Department of Mechanical & Aerospace Engineering of Monash University for generously providing scholarship funding for my invaluable experience in undertaking a post-graduate opportunity. On top of that, I am extremely thankful of the available facilities and staff support that played a big role in achieving the thesis objective.

Last but not least, I would like to express my gratitude to my family members and friends who has given me their time and support throughout my research study. Their presence has definitely lifted my motivation and determination in completing this research and thesis.

Contents

Copyright Notice	1
Abstract.....	2
Declaration.....	3
Acknowledgements.....	4
List of Figures	8
List of Tables	12
1. Introduction	13
2. Literature Review	18
2.1 Contact Methods	18
2.1.1 Vibration analysis.....	18
2.1.2 Ultrasonic waves	18
2.1.3 Acoustic Emission (AE)	19
2.1.4 Others.....	20
2.2 Non-contact Methods.....	20
2.2.1 Visual Inspection (VI).....	20
2.2.2 Eddy Current testing (EC)	21
2.2.3 Radiography inspection	21
2.2.4 Ultrasonic guided-waves.....	21
2.2.5 Thermal loading	22
2.3 Infrared Thermography NDE technique.....	23
2.3.1 Active Thermography.....	25
2.3.2 Passive Thermography	25
2.3.3 Step-Heating Thermography.....	25
2.3.4 Lock-in Thermography	26
2.3.5 Pulsed Thermography	27
2.4 Post-processing Techniques.....	29
2.4.1 Observation.....	29
2.4.2 Temperature contrast method	30
2.4.3 Contrast derivative method	30
2.4.4 Log second derivative method/Thermal Signal Reconstruction (TSR).....	30
2.4.5 Pulse Phase Thermography (PPT)	30
2.5 Chapter Conclusion	31
3. Theory and Methodology	32

3.1 Fundamentals of Heat Transfer	32
3.1.1 Conduction	32
3.1.2 Convection	33
3.2 Transient Heat Conduction in Solids	33
3.2.1 One-dimensional approach	33
3.2.2 Two-dimensional approach	35
3.2.3 Three-dimensional approach	35
3.3 Logarithmic Second Order Derivative Method	36
3.4 Full Width Half Maximum (FWHM)	39
3.5 Resolution of Thickness Measurement	40
3.6 Depth Limit	40
3.7 Minimum Input Energy	41
3.8 Chapter Conclusion	41
4. Model Setup and Validation	43
4.1 Model Setup	44
4.2 Simulation Setup	46
4.2.1 Material properties	46
4.2.2 Model constraints	47
4.2.3 Mesh setup	48
4.2.4 Analysis Manager	50
4.3 Nodal Results	50
4.3.1 Defect depth	52
4.3.2 Defect size	52
4.4 Comparison to Mathematical Model I	55
4.5 Comparison to Mathematical Model II	57
4.6 Chapter Conclusion	58
5. Stationary Heating	60
5.1 Defect Depth Prediction	60
5.1.1 Thin plate test	61
5.1.2 Thick plate test	63
5.1.3 Thick plate test with near surface defect	65
5.2 Defect Size Prediction	66
5.2.1 Thin plate test	66
5.2.2 Thick plate test	67

5.2.3 Thick plate test ($d = 1 \text{ mm}$)	71
5.2.4 Thick plate test ($d = 2 \text{ mm}$)	75
5.2.5 Thick plate (large t_p) with $d = 4 \text{ mm}, 6 \text{ mm}$	76
5.2.6 Proposed modifications for prediction improvement	77
5.3 Chapter Conclusion	81
6. Moving Heat Source.....	83
6.1 Defect Depth Prediction.....	85
6.1.1 Thin plate test	85
6.1.2 Thick plate test.....	86
6.2 Defect Size Prediction	88
6.2.1 Thin plate test	88
6.2.2 Thick plate with near surface defect.....	92
6.2.3 Speed Effect	98
6.3 Effect of Heating Segment Size (l_s).....	99
6.3.1 Segment size, $l_s = 10 \text{ mm}$, heat source speed, $v = 36 \text{ km/hr}$	99
6.3.2 Segment size, $l_s = 15 \text{ mm}$, heat source speed, $v = 54 \text{ km/hr}$	100
6.4 Effect of Heating Duration per Segment.....	104
6.5 Chapter Conclusion	107
7. Conclusion and Recommendations.....	108
7.1 Main Findings and Discussions.....	108
7.2 Implications.....	111
7.3 Limitations and Future Works.....	112
.....	113
8. References	114
Appendix A: Sample calculation of moving heat source speed	119
Appendix B: Minimum Energy	121
Appendix C: MATLAB Script	122
Second order peak derivative method	122
Full Width Half Maximum (FWHM)	130

List of Figures

Figure 1.1 Schematic of rail fastening system [9].	14
Figure 1.2 Examples of images of rail track base with damages. Circled regions indicated a layer of material thinning and a ‘chip’ on the side of the track. Arrows indicate corrosion pitting along the rail.	16
Figure 2.1 Phenomenon of Acoustic Emission (AE) [15].	19
Figure 2.2 Step-heating thermography showing a gradual increase in temperature response [20].	26
Figure 2.3 Lock-in thermography heating input response – t_1, t_2, t_3, t_4 represent random time interval [36].	27
Figure 3.1 Three stages of logarithmic temperature-time decay plot.	37
Figure 3.2 Left: Raw temperature data in logarithm form. Middle: First order derivative of log temperature versus log time plot. Right: Second order derivative of log temperature versus log time [30].	38
Figure 3.3 Illustration of Gaussian-like shape of a typical FWHM plot.	39
Figure 4.1 Two-dimensional front view of the plate model with an underside defect.	43
Figure 4.2 Comparison of FWHM measurements for long and short plates.	44
Figure 4.3 Top view of plate model.	45
Figure 4.4 Surface divided to set up for moving heat source test. Each segment is 5 mm in width.	46
Figure 4.5 Heating period for a stationary heating source.	48
Figure 4.6 Heating period for segment 1 of moving heat source test.	48
Figure 4.7 Heating period for segment 2 (adjacent to segment 1 in Figure 4.6) of moving heat source test (1 ms delay).	48
Figure 4.8 (Left) Tetrahedral meshing - uneven heating. (Right) Hexagonal meshing - uniform heating.	49
Figure 4.9 FWHM measurements at $t = 0.1$ s after heating for a range of element numbers.	50
Figure 4.10 Top view of the plate model with the location where nodal results were recorded (red line).	51
Figure 4.11 Bottom view: Edge effect tests by varying the defect length. (left to right: $\frac{1}{4}$ width, $\frac{1}{2}$ width, $\frac{3}{4}$ width and full width)	51
Figure 4.12 Results from the second order peak derivative with the local material thickness of each node. The uneven structure thickness (material thinning) was also displayed.	52
Figure 4.13 Gaussian curve fitting - the curve fit constantly exceeds the maximum point of the plot.	53

Figure 4.14 Fourier curve fitting (8th order) - curve fit exceeds maximum points and has wiggle ends.	53
Figure 4.15 Low temperature contrast at observation time of 0.1 s.	54
Figure 4.16 Larger temperature contrast at observation time of 1.0 s. This is a typical temperature versus spatial graph for FWHM measurement.	54
Figure 4.17 A plot for FWHM measurements obtained from Figure 4.16 at a range of observation time. The y-intercept is the predicted defect size.	54
Figure 4.18 Temperature response during the early time for moving heat source test: (left) original plot, (right) plot with time delay removed.	55
Figure 4.19 Temperature response at late observation time for moving heat source test: (left) original plot, (right) plot with time delay removed.	55
Figure 4.20 Log temperature-time plot for 4 nodal points across the surface of the sample model. .	57
Figure 4.21 First order derivative of the log temperature-time plots of Figure 4.20.	58
Figure 5.1 (a) Original log temperature-time plot. (b) First order derivative of log temperature-time plot (c) Second order derivative of log temperature-time plot for 5 mm defect size test model.....	61
Figure 5.2 Approximated thickness for the plate model with (a) $D_s = 5$ mm and (b) $D_s = 10$ mm for $t_p =$ 1.5 mm and $d = 1$ mm.	62
Figure 5.3 Approximated plate thickness measurement for a defect at 1.5 mm, 3.5 mm and 7.5 mm depth (a.1, b.1, c.1). The thickness measurement was then offset to display relative thickness using prior knowledge of sound plate (a.2, b.2, c.2).	63
Figure 5.4 Approximated plate thickness for $t_p = 8$ mm with (a) $d = 1$ mm and (b) $d = 2$ mm.	65
Figure 5.5 FWHM measurements over an observation time of up to 1.4 s for $t_p = 1.5$ mm and $d = 1$ mm.	66
Figure 5.6 Plots for defect depth, d at 1.5 mm, 3.5 mm, 5.5 mm and 7.5 mm (a, b, c, d). In each plot, t_R is kept at 0.5 mm, while plate thickness, t_p is varied to simulate the proposed defect depth. The effect of different defect sizes, D_s was also tested.....	70
Figure 5.7 One-dimensional illustration of the defect dimension and location.	71
Figure 5.8 Temperature contrast for various defect sizes at $d = 1$ mm in a plate of $t_p = 8$ mm.	71
Figure 5.9 FWHM measurement plots up to 1.4 s for $d = 1$ mm and $t_p = 8$ mm, with different defect sizes, D_s	72
Figure 5.10 Magnified view of the circled region in Figure 5.9 with the polynomial curve fitting technique.	72
Figure 5.11 One-dimensional view of the plate model for meshing inspection. Dotted lines separate the plate model into two sections: upper and lower deck.....	73

Figure 5.12 Illustration of differences in mesh setup for all 3 cases.	74
Figure 5.13 FWHM measurement plots for defect at $d = 2$ mm, $t_p = 8$ mm with varying underside defect sizes, D_s	75
Figure 5.14 Comparison of FWHM measurements for $d = 4$ mm and $d = 6$ mm with $D_s = 10$ mm in an 8 mm thick plate.	76
Figure 5.15 FWHM measurements for 0.002 s heating period (short heating). $t_p = 8$ mm, $d = 6$ mm, $t_R = 2$ mm and $D_s = 10$ mm.	78
Figure 5.16 FWHM measurements for 0.4 s heating period (long heating). $t_p = 8$ mm, $d = 6$ mm, $t_R = 2$ mm and $D_s = 10$ mm.	79
Figure 5.17 Resultant temperature response after 1.0 s of long heating (0.4 s) applied. Image extracted from FEMAP. The maximum contrast between the defective and sound area is 20.6 °C. $t_p = 8$ mm, $d = 6$ mm, $t_R = 2$ mm and $D_s = 10$ mm.	80
Figure 5.18 Resultant temperature response after 1.0 s of short heating (0.002 s) applied. Image extracted from FEMAP. The maximum contrast between defective and sound area is 0.08 °C. $t_p = 8$ mm, $d = 6$ mm, $t_R = 2$ mm and $D_s = 10$ mm.	80
Figure 6.1 The image sequence shows how a moving heat source test develops. (a) The stage where heat has not been applied yet and the test plate is in ambient condition. (b) The heat source initiates from the left end of the plate. (c) – (f) Heat source gradually moves from left to right. (g) - (i) Development of the ‘hot region’, indicating the presence of an underside defect.	84
Figure 6.2 Temperature-time profile of each node for (a) stationary heating and (b) moving heat source.	85
Figure 6.3 Approximated plate thickness for $t_p = 1.5$ mm with (a) $D_s = 5$ mm and (b) $D_s = 10$ mm, both with $d = 1$ mm.	86
Figure 6.4 Heating speed of 18 km/hr for a $t_p = 8$ mm model with (a) $d = 1$ mm and (b) $d = 2$ mm. Both cases have $D_s = 5$ mm.	87
Figure 6.5 Overview of a thin plate with defect at $d = 1$ mm.	88
Figure 6.6 FWHM measurements for plate with $t_p = 1.5$ mm, tested with $D_s = 5$ mm and $D_s = 10$ mm at $d = 1$ mm using moving heat source.	88
Figure 6.7 FWHM measurements comparison for stationary and moving heat source test. $t_p = 1.5$ mm, $d = 1$ mm, $D_s = 5$ mm.	89
Figure 6.8 Comparison of temperature contrast profile in stationary and moving heat source test for $t_p = 1.5$ mm, $d = 1$ mm, $D_s = 5$ mm.	90
Figure 6.9 Image sequence of moving heat source with slow speed at 0.2 km/hr. Figure (a) at 0.18 s and (b) at 0.38 s.	91

Figure 6.10 FWHM measurements for model $t_p = 8$ mm with $D_s = 10$ mm at $d = 1$ mm. Moving heat source speed at 18 km/hr.	92
Figure 6.11 The curve fitting and back-extrapolation for the descending trend of FWHM measurements.	93
Figure 6.12 FWHM measurements for $t_p = 8$ mm model with $D_s = 10$ mm at $d = 2$ mm. Moving heat source speed at 18 km/hr.	94
Figure 6.13 A ‘hot spot’ illustration during the transient cooling of the material.	95
Figure 6.14 Curve fitting and back-extrapolation for the $t_p = 8$ mm model with $D_s = 10$ mm at $d = 2$ mm. Moving heat source speed at 18 km/hr.	95
Figure 6.15 Screenshot of transient cooling for a moving heat source test at observation time (a) 1.4 s and (b) 1.5 s with temperature contour at 25 °C – 26.75 °C. Model setup with $t_p = 8$ mm, $d = 6$ mm, $D_s = 10$ mm.	97
Figure 6.16 Defect depth location in a plate model ($t_p = 8$ mm) with 54 km/hr heating speed.	98
Figure 6.17 Plateau temperature.	99
Figure 6.18 FWHM measurements for a model with $l_s = 10$ mm, $t_p = 8$ mm, $d = 1$ mm and $D_s = 10$ mm.	100
Figure 6.19 Curve fitting and back-extrapolation for defect size estimation.	100
Figure 6.20 FWHM measurements for $l_s = 15$ mm, $t_p = 8$ mm, $d = 1$ mm and $D_s = 10$ mm.	101
Figure 6.21 Curve fitting and back-extrapolation for defect size estimation.	101
Figure 6.22 FWHM measurement profile for 3 setups with different heating segment sizes, l_s and resulting heating speed, v . Model plate has a thickness of $t_p = 8$ mm, $D_s = 10$ mm, $d = 1$ mm.	102
Figure 6.23 FWHM measurement profile for 1 ms heating duration per segment for a model of $t_p = 8$ mm, $d = 1$ mm and $D_s = 10$ mm.	104
Figure 6.24 Curve fitting and back-extrapolation for defect size estimation.	104
Figure 6.25 Comparison of temperature contrast for three different heating duration setup.	105
Figure 6.26 FWHM measurement profile comparison for three different heating duration in a model of $t_p = 8$ mm, $d = 1$ mm and $D_s = 10$ mm.	106
Figure 7.1 Illustration of multiple heating sources stacked one after another.	113

List of Tables

Table 2.1 Results on heating technique for an experimental test conducted by Vavilov et al. [21]. ...	23
Table 2.2 Typical application of different excitation sources.	26
Table 2.3 Summarised comparison between flash thermography and transient thermography.	29
Table 4.1 Abbreviations and definitions.	43
Table 4.2 Range of dimensions for the defect at the underside of plate model. The dimension symbols can be referred at Figure 4.1.	45
Table 4.3 Thermal properties of mild steel used in simulation [47].	47
Table 4.4 Variables for meshing convergence test.	49
Table 4.5 Theoretical temperatures at different observation time and thermal energy application. .	56
Table 4.6 Comparison of theoretical calculated surface temperature and simulated surface temperature at different observation time.	56
Table 5.1 A table summary for the Fourier number time domain and measured material thickness range for respective plate model thickness.	64
Table 5.2 Comparison of actual and predicted outcome of defect size	66
Table 5.3 Summary table for differences between actual and predicted defect sizes.	72
Table 5.4 Meshing inspection for upper and lower deck as described in Figure 5.12.	73
Table 5.5 Comparison between $d = 1$ mm and 2 mm in a plate model.	75
Table 5.6 Defect size prediction for $d = 4$ mm and $d = 6$ mm with $D_s = 10$ mm in an 8 mm thick plate.	77
Table 5.7 Differences in FWHM measurement at respective observation time when heating period is increased.	78
Table 5.8 Comparison results of defect size prediction, D_{SE} for 2 ms and 0.4 s heating. Coefficients of determination value of curve fitting are provided in brackets.	79
Table 6.1 Results of moving heat source test for thin plates with defect at $d = 1$ mm.	89
Table 6.2 Comparison of predicted defect sizes at different depth location into the material volume using moving heat source.	96
Table 6.3 Defect size prediction for different sizes of heating segment size.	102
Table 6.4 Temperature contrast.	103
Table 6.5 Maximum achievable temperature.	103
Table 6.6 Summary for defect size prediction under different heating duration per segment.	106

1. Introduction

Rail travel is a popular and efficient form of passenger and courier transport. It is used to mass transport people and goods over a long distance at minimal cost [1]. According to statistics, the rail line owned by Network Rail in the United Kingdom carries 1.3 billion journeys and 28 billion kilometres every year [2]. Meanwhile, in Australia, the rail systems are extremely important in connecting suburbs with the city centre and transporting mining materials to processing plants. It is evident that any disruption or failure of the rail network will lead to massive financial losses or even fatalities.

Like any other transportation modes, rail travels are prone to various problems. The frequent use of rail travel means the greater possibility of failures due to wear and tear over time. Minor failures can cause a train to cease operations, whereas major failures can lead to train derailments. US Federal Railroad Administration released a safety statistics data indicating that 2700 derailments occurred during the 1992-2002 decade, costing a total loss of \$441 million [3]. One of the recent cases of train derailment occurred in Raigad district, India where at least 18 people were killed and 124 injured. Earlier in that year, another incident happened in India with 3 casualties and 37 injuries [4]. To date, Africa's deadliest train crash was the derailment accident in Ethiopia on January 14, 1985. Approximately 428 lives were lost with all other passengers on board wounded. Such tragic incident has served as a lesson for better rail system integrity and maintenance. Nonetheless, train derailments are still a worrisome issue in the railway industry, including first World countries.

To increase the safety level of rail travels, the manufacturing and maintenance of rail parts must be taken into serious care. For new rail line projects, rail tracks and bogies must be manufactured to zero-defect precision, before being authorised for commercial purposes. For existing rail line projects, there is a need to perform scheduled monitoring on the structural integrity of the rail track. This can be achieved with advanced structural inspection methods that utilise Non-destructive Evaluation (NDE) approach. Rail tracks in poor conditions can be replaced or maintained timely to prevent further damages or failure. The objectives of these precautionary steps ensure the smooth operation of the rail network and minimises opportunity cost of network downtime and preventative maintenance [2].

Catastrophic train accident could be caused due to the failure of bogie or rail track systems. Transverse defects along the rail track are reportedly the primary cause of train accidents [2, 3] as compared to the longitudinal defects. These defects are often found in the rail head, rail web and rail base. Some damages are also caused by wear and tear, and corrosion over time [5]. For example, rail tracks constructed in a tunnel will have a higher tendency to corrode at a faster rate as it has an enclosed room from sunlight which promotes a damped environment for rapid corrosion. Other defects are caused by the intense dynamic loading of operating trains.

When comparing the bogie and rail track system, the latter was found to be a greater challenge and concern in terms of structural inspection. It has an extended structural length and fixed-to-ground nature. In fact, many studies [1-3, 6-8] have been made to address the structural inspection of rail tracks and most of them resulted in a positive outcome. One of the studies were done on the inspection of squats on rail steel head by Peng and Jones [6]. Rail squats are common in rail heads due to the increase in operating loads, traffic and train speeds. The study established a relationship between squat depth and thermal image phase angle using lock-in thermography [6]. As for rail web components, researchers were able to perform reliable inspection with the use of ultrasonic energy. Ultrasonic transducers were mounted at the rail base while measured signals from rail end reflection indicated the condition of the track [2]. One of the area which however lacked knowledge on is the rail base. It is often difficult to detect cracks at the rail base, especially at the underside.

Figure 1.1 illustrates a typical rail base structure. As rainwater accumulates within the rubber pad and rail foot, the tendency for corrosion to occur is high. Over time, this corrosion will develop an air gap in the form of a defect as depicted in Figure 1.2. The continuous operation of the train will increase dynamic loading on the system, resulting in a potential fatigue failure.

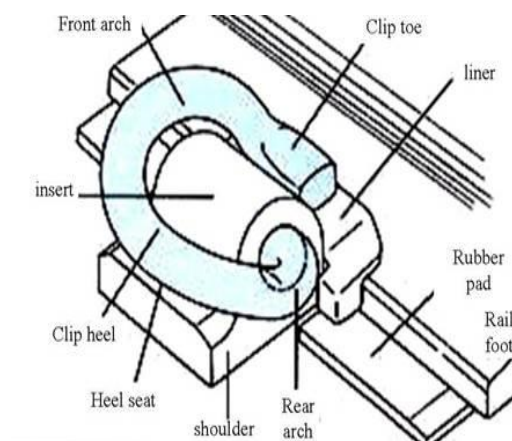


Figure 1.1 Schematic of rail fastening system [9].





Figure 1.2 Examples of images of rail track base with damages. Circled regions indicated a layer of material thinning and a 'chip' on the side of the track. Arrows indicate corrosion pitting along the rail.

The existing rail track extends to a few thousands of kilometres across the country with numerous amount of clips attached along this length of track. To perform a manual inspection on the condition of these sections of the track will require an unrealistic amount of time and labour effort. Besides, the fixed-to-ground nature of rail base also proves as a challenge for many existing structural evaluation methods to be implemented. Therefore, there is a need for an efficient and convenient system to address this problem and improve the structural integrity of rail tracks.

The aim of this thesis is to develop a moving heat source technique for the quantitative and qualitative measuring of defects at the underside of a flat plate. A typical structural defect is identified as corrosion air gaps, delamination, voids, inclusions or impact damages. It is anticipated that this technique will be suitable for a long distance of inspection with minimum supervision and cost at a short time frame. The flat plate is used as a simple representation of a rail base in this study. Despite this substitution, tests were focused on analysing model thickness of 8 mm to resemble a rail base thickness. In this research, a study on the use of a stationary heat source was conducted to establish a basic understanding of the results for Infrared Thermography technique. Next, a moving heat source was used to perform heating across the top surface of the plate model at a range of speed. Temperature responses, spatial positions and observation time are the main sets of raw data collected and analysed throughout this study.

2. Literature Review

The importance of the structural health in the rail industry can be clearly seen in the previous chapter. Without the timely maintenance or sufficient knowledge on the subject condition, it may lead to many negative consequences. Structural inspection can be performed using the contact or non-contact evaluation method. Both methods are generally the exact opposites of each other at which the latter does not involve any physical touch between the test material and equipment.

2.1 Contact Methods

Contact methods are commonly associated with the need of physical loading or the attachment of sensor devices for signal measurement. This method can often cause wear and tear to the inspected material, due to physical loading over an extended period. Nonetheless, if the contact method only involves the attachment of sensor devices, then the material will not be damaged physically.

2.1.1 Vibration analysis

One of the common contact methods is the use of vibration analysis. It is a non-destructive short term testing method. However, if pursue over a longer period, will cause fatigue failure as a result of repeated loading [10]. The vibration analysis test method relies on the changes in structural vibration resulting from a defective structure [10].

Tsunashima et al. [7], developed the idea of 'probe-vehicle' system where a driver steers the system across a railway track to gather information on track conditions. The system is equipped with GPS system, sensors, map-matching algorithm, strain gauges, and signal processing system. As the vehicle travels across an irregular rail surface, any changes in displacement will be detected as vibration by the sensors and converted into vertical and lateral accelerations. Using the plots of acceleration in real-time, one can determine the position of track irregularities and perform necessary maintenance. In addition, the roll angle of the vehicle and spectral peak from cabin noise will provide information on track level irregularity and rail corrugation. Nonetheless, the probe-vehicle method is only capable of measuring surface dent or defect. Subsurface or rear side defect of the rail track is unlikely to be detected [7].

2.1.2 Ultrasonic waves

The idea of contact methods also includes the attachment of recording and measuring equipment, even if the subject did not have physical contact with external stimuli. For example, the use of ultrasonic guided-waves as a Non-Destructive Evaluation (NDE) tool is categorised as a contact method since the recording sensors were attached to the subject of inspection. Rose et al. [1] proposed to use fixed sensors to monitor the structural integrity of the rail track. Then, an operating

train emits ultrasound source while traveling across the inspected regions. Ultrasonic signals recorded by the installed sensors is used to determine any irregularities along the track. The major disadvantage of this method is that it needs a good number of sensors installation along the rail track for a long distance inspection.

2.1.3 Acoustic Emission (AE)

Acoustic emission is another form of non-destructive contact evaluation method. It requires the mounting of piezoelectric sensors on the inspected subject to detect elastic strain waves within the structure [11]. A simple sketch on the phenomenon of acoustic emission can be seen in Figure 2.1. Unlike active approach detection, AE is a passive damage detection approach that does not involve any actuation [12].

Acoustic emission (AE) is elastic stress waves that usually ranges between 20 kHz to a few MHz [11, 13]. When a crack propagates in a material, molecular bonds are broken to release energy [14]. It is the dynamic deformation process in the solid which generates strain waves within the material. A typical AE event has a voltage-time history that consists of peak voltage amplitude, rise time, event duration and hit counts [15]. This is used to determine whether a crack is present or growing. Meanwhile, to locate the position of the crack in a subject, the arrival time of strain waves at the piezoelectric sensors is analysed. Multiple sensors will provide an improved estimation of the crack location [15]. Nonetheless, these detected waves are complex as a result of wave dispersion and geometry boundaries effect [14].

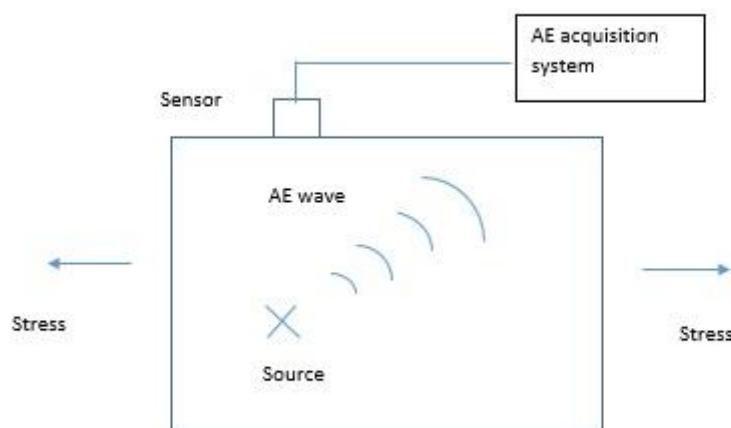


Figure 2.1 Phenomenon of Acoustic Emission (AE) [15].

AE is commonly used to monitor locations with potential cracks while offering real-time evolutionary of defects. One of the advantages of AE is its ability to detect crack early with its high sensitivity. Moreover, it can perform continuous monitoring even if the structure operates at normal rate [15]. Examples of AE evaluation technique is commonly found when detecting movement of fibre leakage, crack initiation and propagation, matrix cracking and delamination in laminated composite plates [11, 13].

One of the problems encountered in AE is the effect of high background noises, often affecting the accuracy of AE results [11]. AE also struggles to deal with complex geometries and multiple cracks [16]. Kaphle et al. [15] discussed the approaches used in attempting to differentiate various background noises from a genuine signal for accurate identification of crack initiation rate and position. Rabiei et al. [16] reported quantitative methods for AE monitoring.

2.1.4 Others

Liquid or Dye Penetrant Inspections (LPI or DPI) utilises a special dye for inspection of materials. This is usually implemented for weld surfaces. The dye is spread over the target area and allowed to dwell in. If there is a defect or crack on the surface, the dye will leak inside and flow back out which can be visually observed. Often these dyes may give a permanent coloured stain to the structure [17].

Magnetic Particle Inspection (MPI) is a visual technique that uses the magnetic field of ferrous particles to detect defects. These ferrous particles will align accordingly near the defect or crack due to a change in magnetic flux [17]. However, this method is only applicable to ferrous material structure.

2.2 Non-contact Methods

The non-contact method is usually a non-destructive evaluation (NDE) technique. The specimen under investigation for discontinuities or differences in characteristics does not lose its serviceability after being inspected [18]. This popular method has been used to monitor the integrity of composite structures such as aircraft and prosthetics [19] during their operational life-cycle and to predict failure before occurrence [20]. Some examples include enhanced visual techniques, ultrasonic (sensors not attached to specimen), eddy current inspection and thermal loading [21].

2.2.1 Visual Inspection (VI)

Visual inspection (VI) is the most fundamental technique for inspection of material structural integrity where it is conducted with 'naked eye' [13]. The method is only capable to locate large surface damages or dents when cleaning is required for a dusty surfaces [17]. On the downside, VI offers very limited information. It is unable to inform underside defects nor delamination in composite structures. Also, the quantitative measurements of surface damage is difficult [17]. For large scale inspection that

extends to a few kilometres, VI can be very time-consuming and labour expensive [17]. Overall, it is a convenient initiative in detecting defects, however not an approach for structural health maintenance planning.

2.2.2 Eddy Current testing (EC)

Eddy current (EC) testing is an electromagnetic method that uses the concept of electrical impedance within an electrically conducting material [13]. It follows the principle of Faraday's Law and Lenz's Law. First, an alternating current (AC) is induced in a wire coil to create a changing magnetic field. Then, this magnetic field is brought close to the surface of the inspected material, to induce the flow of eddy currents in the material. The frequency of the AC will determine the penetration depth of eddy current in the material. If a defect is present, it will obstruct the flow of eddy current, causing a change in magnetic field that will fluctuate output voltages. The EC testing is a low-cost method that is able to detect small defects. Nevertheless, it is limited to near surface inspection [17].

2.2.3 Radiography inspection

Radiography inspection relies on X-ray or gamma ray as the source of inspection. The technique requires the energy source on one side of the inspected material and a recording film on the other side. There are also studies suggesting the design of having both source and recording film at the same side of radiography inspection. During X-ray inspection, a concentrated beam of electrons is targeted at the material. The total amount of radiation absorbed by the recording film is dependent on the material density [22].

This inspection method is able to detect corrosion or defects in the weld. For materials with an insulation layer, X-ray can penetrate through. In some cases of composites, radiography, can however be, very ineffective due to the low absorbing ability of X-rays. Reviews showed promising results by introducing penetrants such as zinc iodide solution that enhances material surface for X-ray inspection [13]. The major concern and drawback for this method is the hazardous use of X-ray which could cause chemical and biological changes to the human body. Besides that, the inspection method always requires bulk equipment which is not portable, in addition to the high operating cost [17]. Nowadays, traditional radiographs are replaced with a more reliable digital radiography that is able to remove unwanted reflections during the development of radiograph film.

2.2.4 Ultrasonic guided-waves

The application of ultrasonic waves can also be used in a non-contact and non-destructive evaluation (NDE) manner. This can be achieved by ensuring that the emitting and sensing device are not attached to the inspected body. In general, ultrasonic waves are a form of sound energy that is produced by

the rapid vibration of a piezoelectric piece [3]. Terminologies such as transmission waves and reflection waves are helpful in this context. Many studies have been performed to utilise this method in structural health monitoring [1, 3]. In the rail industry, Rose et al. [1] used ultrasonic guided waves as a non-contact evaluation method to inspect rail conditions. This is achieved by mounting two transducers on each end of the rail inspection car. On the front end, ultrasound energy is emitted from the transducer onto the rail track. On the other end, a transducer is used to receive the transmitted signal over the rail track. An appropriate signal processing technique will be required to analyse the output signals.

The ultrasonic wave relies on the working principle of pulse echo and through-transmission. Pulse echo refers to a situation where the ultrasonic transducer and sensor are located at the same position. The reflected ultrasonic signal is able to indicate the condition of the rail track. Alternatively, the through-transmission method implements the idea of having ultrasonic transducer on one end, while a sensor on the opposite end.

To summarise, if a defect is encountered by an ultrasonic wave, the transmitted or reflected signal will be distorted as shown in Figure 2.2. The propagation distance of a travelling wave is dependent on the wave frequency. The extent to which the frequency and amplitude of the signals change is used to determine defect sizes via appropriate signal processing algorithm such as Discrete Wavelet Transform (DWT) [1, 3]. The downside of using wave guided inspection is the restricted propagation path. In addition, only some types of defect can be detected depending on how ultrasound is emitted [3, 8].

2.2.5 Thermal loading

Thermal loading is referred to the application of heat on inspected subjects. The types of heating method include optical heating, convective heating, contact heating and electromagnetic induction heating [23]. Generally, these are categorised as surface heating at which the specimen was induced with an external heat source. For example, Baek et al. [24], utilised the electromagnetic heat induction method to detect steel corrosion in reinforced concrete (RC) structures. This is a non-contact method as heat was not applied in direct contact with the specimen. A power source is used to generate high-frequency alternating current in an induction heating coil. Then, the magnetic field in the vicinity of the coil changes rapidly to produce eddy currents in the specimen that intercepts the induced magnetic field. This eventually leads to Joule heating [24]. As the specimen surface is heated, the IR radiation emitted at the opposite end was measured using an infrared (IR) camera. The measured temperature indicates the severity of steel corrosion based on the differences in the thermal characteristic of a corroded and non-corroded region. Using this method, Baek et al. [24] successfully

detected corrosion of a bare rebar and RC structures with different cover depths and corrosion amount. In summary, the higher the corrosion level, the higher the rate of heating, cooling, peak IR intensities and temperature [24].

Optical heating was attempted by Vavilov et al. [21] to detect corrosion in thick metals. Optical heating converts electrical energy into light source which in turns create thermal energy. Table 2.1 illustrates the results of different heating techniques.

Table 2.1 Results on heating technique for an experimental test conducted by Vavilov et al. [21].

Heating Techniques	Number of defect detected from a total of 9
Air blower	5
Halogen lamp (500 W)	4
Halogen lamp (5000 W)	5
Line heater (2 mm from surface, speed at 40 mm/s)	0
Planar contact heater	2
Xenon lamp	3

Flash lamps are a type of short duration optical heating. It covers a large area of inspection however suffers from afterglow [25]. There are also heat lamps that can be used for longer duration or laser that has much higher intensity. Unfortunately, both sources are expensive and hazardous to the user [25].

As a rule of thumb, longer heat excitation will result in greater amount of heat energy transfer and signal-to-noise ratio. Then again, temperature measurements for long period heating must account for the possible effect of surface reflection during heating and heat saturation [23].

2.3 Infrared Thermography NDE technique

Based on the literature comparisons made earlier, the use of infrared thermography with thermal loading for the inspection of underside defects is more suitable than other methods. The infrared thermography method has a fast inspection rate, therefore best suited for the objective of long

distance rail tracks inspection. In addition, infrared thermography is more capable to detect defects in complex geometries [25].

Infrared Thermography is a non-destructive evaluation (NDE) and non-contact method where it can be stimulated by optical energy, ultrasonic energy or electromagnetic [26]. It utilises the inconsistency of heat conductivity throughout the specimen thickness with the defect to draw conclusions on structural conditions. The local temperature differences due to alteration in heat conductivity created in the vicinity of a defect can be measured using an IR camera. Previous studies show that the measurement of front or back surface (reflection or transmission mode) is able to produce promising results [27]. Typical IR camera measures infrared wavelength in the range of 0.9 to 13 μm [24]. When an object is heated, the state of an atom in the object will experience an increased in potential energy and frequency. Areas at a lower temperature will have a lower frequency. Using the differences in frequency level due to temperature difference, an IR camera can convert this radiation level to thermal images for observation [24].

Temperature gradients are often useful in determining defect sizes [28], in addition to characterising the severity of corrosion [21]. When compared to other inspection methods, infrared thermography offers large area inspections in a short time, while providing full field images in a non-contact form [23]. The term 'infrared' in Infrared Thermography indicates the absence of hazardous radiation unlike radiography, therefore categorised as a safe NDE method [29]. Initial efforts relied on visual or numerical identification of surface temperature contrast for qualitative and quantitative measurement. However, this can be improved by evaluating the temperature-time history response of each pixel [23]. It is now widely used for structural evaluation test on ceramics and composites, while developing in use with metals [21, 25, 30].

Nonetheless, there are a few limitations to date with the infrared thermography technique.

- (i) Materials with low emissivity tend to cause reflection upon heating optical radiation (Inspection guideline recommends the use of test materials with emissivity greater than 0.6 - 0.7. Otherwise, a dye can be used to improve surface emissivity [21]).
- (ii) Short observation times require high-speed infrared camera [21]
- (iii) For thick samples, an optimum amount of heat and heating time is required to provide sufficient energy absorbed [21]

2.3.1 Active Thermography

Pulsed thermography is an example of active thermography [31]. In active thermography, an external heat source is applied on the sample surface where the temperature changes are monitored for any significant contrasts. When thermal wave diffuses into the sample, an embedded defect will act as an obstacle with higher thermal impedance. The affected wave will experience changes in heat diffusion rate. Subsequently, a local accumulation of heat energy increases the surface temperature adjacent to the underside defect. This is used to determine the substructure condition of the sample [20]. This mode of thermography is widely used in engineering applications [28]. In another scenario, when detecting surface defects, thermal wave enters the crack and undergoes multiple reflections within the crack. This causes more thermal waves to be absorbed in this region, resulting in a high-temperature zone. Broberg et al. [25], found that the smallest surface crack that could be detected was approximately 5-10 μm .

2.3.2 Passive Thermography

The passive mode of thermography does not require any form of external heat source. It relies entirely on the thermal radiation within the object [28]. Using passive thermography, any anomalies can be observed by analysing the temperature profiles during normal operation of the structure. Examples of passive thermography include the overheating of engines and electrical circuits [32]. It is also often used for materials that are naturally at a different temperature compared to an ambient condition such as the sea [33, 34]. The drawback of this technique is its inability to perform quantitative measurements.

2.3.3 Step-Heating Thermography

Step heating utilises a continuous and uniform heat flux over a long period of time. Figure 2.3 shows the gradual increment in temperature with respect to time when step heating is applied. The use of low intensity heating stimulation allows heating to take place longer without being invasive to the specimen. As a result, it can detect deeper defects since saturated thermal waves can propagate further into the sample. Early studies suggested that the time at which temperature over the defective area is higher than the surroundings can be used to evaluate the defect depth [20].

Badghaish et al. [20], determined the defect depth in a glass fibre reinforced composites (GFRP) using the step heating thermography. Flat-bottom holes and embedded defects were induced to understand the effect of finite and infinite thermal impedance. Using the 'early time' detection method on one-dimensional analytical solution, finite element models and experimental tests, the test measurement on GFRP thickness up to 13 mm was successful. These observations were made during the heating period to observe for temperature-time slope deviation or temperature contrast.

For defect radius to thickness ratio smaller than 2, it is important to consider the theory of three-dimensional heat transfer instead of the early time detection method. The effect of lateral diffusion is significant for a small defect at short observation time, therefore will cause inaccurate analysis. Nonetheless, step heating method has limited success due to back-reflect radiation and difficulty in providing sufficient thermal energy in a short time [21].

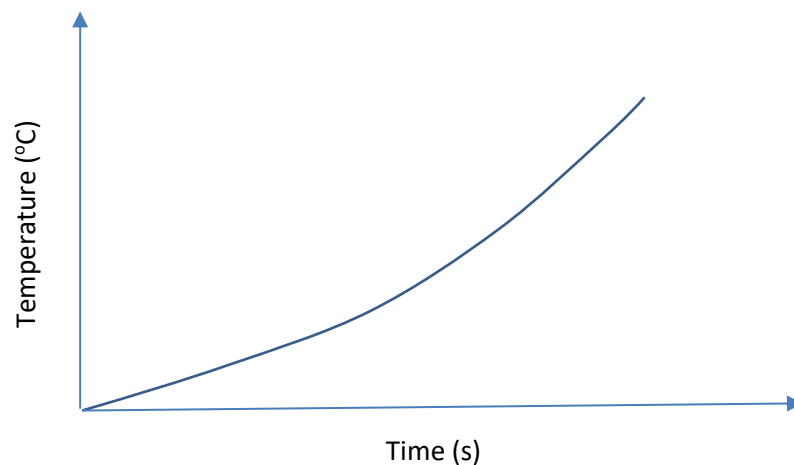


Figure 2.2 Step-heating thermography showing a gradual increase in temperature response [20].

2.3.4 Lock-in Thermography

Lock-in thermography uses the repetitive heating method at which the source can be sinusoidal (for example Figure 2.4) or rectangular waveform depending on the objective of inspection. The frequency of wave ranges from 0.01 Hz up to 20 Hz, with a possible duration of seconds to hours [19]. Halogen lamps, ultrasound heating and mechanical stimulation are among the type of external stimulus that can be used for lock-in thermography. An internal thermal stimulus can be introduced via thermo-elastic effect [6]. The cheapest type of heat source is the halogen lamps, whereas care must be taken if applying ultrasound heating. Excessive heating can lead to a significant rise in temperature. Eventually, it will be destructive to the sample inspected or dangerous to the user.

Table 2.2 Typical application of different excitation sources.

Excitation Source	Typical Application
Halogen lamp heating	Voids in multi-ply structures
Ultrasound heating	Deep cracks
Mechanical stimulation heating	Stress patterns

During lock-in thermography, thermal waves will constantly experience reflection, hence creating an interference between incident and reflected waves. The resultant surface temperature recorded is then Fourier-transformed into amplitude and phase. It is then used to produce an image for further analysis [29].

The advantages of using this non-contact method are that it allows for wider area inspection and produces results that are easily interpretable. Peng et al. [6] tested rail specimens with squats using the lock-in thermography method. It was found that the heating amplitudes and effect of convection losses did not alter the phase response of the material surface. This suggested that only the material properties and defect geometry were affecting the results. A general trend was established that for a larger defect diameter with small depth, the phase contrast is the largest. Ultimately, the lock-in thermography was useful in detecting the presence and location of rail squats [6]. The downside of this thermography technique was its inability to deal with non-uniform heating and non-uniform surface emissivity problems [35].

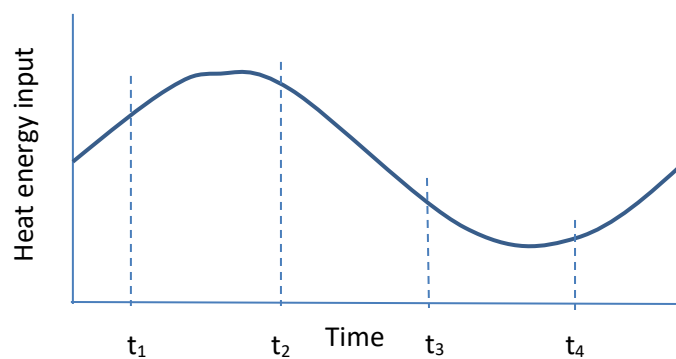


Figure 2.3 Lock-in thermography heating input response – t_1 , t_2 , t_3 , t_4 represent random time interval [36].

2.3.5 Pulsed Thermography

Pulsed thermography, also known as flash thermography or transient thermography, has recently replaced the traditional use of ultrasonic inspection. In pulsed thermography (PT), the inspected surface is heated for a short period with a high-intensity flash. A flash duration of 3-10 ms is sufficient to inspect a thin aluminium [21]. The heated surface temperature response over time is recorded using an infrared camera to study the transient cooling behaviour of the material [30, 35]. The transient flow of heat from the surface into the specimen will be obstructed if a thermal discontinuity is met, resulting in a local temperature rise [30]. In terms of application, a xenon flash lamp can be used as a source of flash thermography for inspection of corrosion behind paints. Meanwhile, the use of halogen lamp for transient thermography in detecting delamination is the most popular approach in composite inspection to date [29]. Metals, which have high thermal diffusivity, are usually a better material for flash heating inspection. The detail differences between flash and transient thermography is outlined in Table 2.3. Materials with low thermal diffusivity such as composite limits the detection

of deep defects [19]. When compared to other thermography methods, pulsed thermography is easily affected by non-uniform heating and irregular surface condition [26], in addition to greater limitations in material depth measurements [37]. Further studies have since then evolved about developing methods to overcome the aforementioned issues. This includes the concept of Thermographic Signal Reconstruction (TSR), Pulse Phase Thermography (PPT) and others.

Pulsed thermography is one of the more favourable imaging technique as it offers a large area inspection, faster inspection time, repeatability and higher sensitivity than other testing methods [38, 39]. Apart from being non-contact, it has the better ability to inspect features with curvature [30]. Its inspection ability has since been enhanced greatly by the improvements in IR camera technology and post signal processing methods. Moreover, it is able to measure sample thickness, surface and subsurface defect, and thermal diffusivity of a specimen [30, 37]. Lastly, the experimental set up for this technique allows for the flexible positioning of detector and heat source [38].

Shepard [30] reported that pulsed thermography is most effective when the diameter of a subsurface defect is greater than its depth beneath the surface. This is essential to ensure sufficient temperature contrast between defective and non-defective areas in overcoming background noise level. Nonetheless, there are existing signal processing methods that are able to filter undesired noises [30].

Lichun et al. [26], discovered the appearance of artifacts in the form of noise, induced by the reflection of flash thermography. Materials with metallic properties mostly have highly reflective shiny surfaces [26]. The best approach to overcome this problem is by coating the surface with black paint to lower reflectivity and increase the emissivity [21, 26]. However, this is not ideal for some cases. Instead, various signal processing methods such as spatial filtering, image subtraction, and frequency domain filtering can be used to suppress the effect of artifacts and other noises [40].

Table 2.3 Summarised comparison between flash thermography and transient thermography.

	Flash thermography	Transient thermography
Heating duration	Milliseconds	Seconds to minutes
Similarity	<ul style="list-style-type: none"> Utilises the transient cooling behaviour of a material to determine its thermos-physical properties or thickness 	
Advantages	<ul style="list-style-type: none"> Short inspection time Depth-resolved inspection Inspection of thin layers Detection of shallow defects 	<ul style="list-style-type: none"> Large area inspection Affordable heat sources Low thermal loading due to slow heating
Disadvantages	<ul style="list-style-type: none"> Limited inspection area Only shallow defects High thermal loading 	<ul style="list-style-type: none"> Not suitable for thick layers (however able to inspect thicker layers than flash thermography due to the larger amount of energy)

2.4 Post-processing Techniques

The objective of post-processing techniques is to analyse and improve detected temperature signals by suppressing noises [21]. Whether it is infrared thermography or traditional ultrasonic technology, there is a need to post-process raw data to produce comprehensible information. In this context, the post-processing techniques will be mainly focused on infrared thermography.

2.4.1 Observation

This is the simplest form of retrieving information on the substructure of a sample. Using an infrared camera, a 'hot spot' can be found over a defective region in a sample. This is a brief approximation of the defect location, however, unable to provide further information on the size and depth of defect.

2.4.2 Temperature contrast method

The temperature contrast method utilises the temperature differences between a defective and non-defective region. The mathematical equation is given as:

$$TC_{abs} = T_{def} - T_{ND} \quad \text{Equation 2.1}$$

TC_{abs} is the absolute temperature contrast and def is the abbreviation for defective, whereas ND is non-defective. The time at which the maximum temperature contrast occurs is a function of the defect depth. The deeper the defect, the longer the time taken for this peak contrast to occur [29, 38]. However, for a deep defect, the temperature contrast will be less significant than the shallow defect. This is due to the lower amount of reflected thermal wave energy reaching at the inspected surface. A New Absolute Contrast (NAC) method was later introduced to improve this Temperature Contrast Method [31].

2.4.3 Contrast derivative method

The contrast derivative method is a similar alternative to the temperature contrast method. The only difference is the use of first derivative of temperature contrast. Using the peak time, t_s for maximum contrast derivative and Equation 2.2, the defect depth, x can be determined from Equation 2.2 [29].

$$t_s = \frac{3.64x^2}{\pi^2\alpha} \quad \text{Equation 2.2}$$

2.4.4 Log second derivative method/Thermal Signal Reconstruction (TSR)

The logarithmic second order derivative method utilises the logarithmic form of a one-dimensional heat diffusion equation. During cooling, the log plot will yield a constant -0.5 slope. If obstructed by any subsurface discontinuity, the slope will deviate to 0. The time at which this occurs can be used to determine the defect depth [29]. The advantage of this method is that it does not require any prior knowledge on the non-defective area as compared to temperature contrast method and contrast derivative method.

2.4.5 Pulse Phase Thermography (PPT)

PPT uses the Fourier transformation technique on raw temperature data to create useful phase images. Using the phase and magnitude values, PPT predicts defect depth based on the differences in phase among each pixel over the sample surface. The biggest advantage of PPT is its ability to detect deeper defects as it uses the frequency domain for analysis. Nonetheless, the use of Fourier transformation removes temporal information from result data, resulting in difficulty when making quantitative measurements [41].

2.5 Chapter Conclusion

The inspection of structural defects is important in setting up preventive measures for structural failure or maintenance planning of structures. This can be carried out with a contact or non-contact methods which can also be categorised into destructive or non-destructive test method. The contact methods as discussed earlier include vibration analysis, ultrasonic waves, acoustic emission (AE) and liquid or dye penetrant inspection (LPI/DPI). Meanwhile, non-contact methods include visual inspection, eddy current (EC) testing, radiography inspection, thermal loading and ultrasonic guided waves (without sensor attachment). When comparing all advantages, a non-contact method is preferred as it will not cause destruction to the inspected subject. In addition, it will less likely interfere with the routine operation of the subject. The thermal loading method is more attractive method as it has the ability to detect surface, embedded and underside defects. It is also one of the safest method and easy to implement technique at low cost.

The thermal loading method, also known as infrared thermography refers to the application of heat and use of an infrared camera to observe temperature changes. Infrared thermography can be subdivided into step-heating thermography, lock-in thermography and pulsed thermography that has respective advantages and disadvantages. Ultimately, pulsed thermography is preferred over lock-in and step-heating thermography given that temperature is easier to detect with the elimination of reflection effect. Lastly, a set of post-processing technique was outlined. It was aimed to convert temperature response data into useful information for defect sizing. The next chapter will further elaborate on the choice of post-processing technique used for this research study. It will also include theory on heat transfer to provide a relevant explanation of results obtained in later chapters.

3. Theory and Methodology

The previous chapter suggested that infrared thermography is the most appropriate technique for achieving the aim of this thesis. In conjunction to that, the study on heat transfer is inevitable. In this chapter, the fundamentals of heat transfer and relevant theories will be discussed. The discussion will include mathematical equations that will be useful to explain and describe the heat transfer behaviour during the transient cooling period of heating. Besides, processing algorithms that are used to perform quantitative measurement of defects were elaborated. The elaboration is important as raw results are usually saturated with background noises and require filtering and processing.

3.1 Fundamentals of Heat Transfer

The phenomenon of heat transfer usually occurs when there is a temperature gradient between two objects sharing one interface or within the object itself [42]. Due to this difference, the higher thermal energy from the hotter region will propagate in waveform to the colder region to reach thermal equilibrium. Thermal equilibrium is achieved at a steady-state condition where observation time extends to infinite. This is particularly an important aspect in computational research as it confirms the convergence of a thermal analysis system [43]. During heat transfer, the hotter region will gradually experience a drop in temperature due to energy dissipation, whereas the colder region will have an increase in temperature. There is a need to address and understand the two principal modes of heat transfer, which are conduction and convection.

3.1.1 Conduction

Heat conduction is the heat transfer between two solid objects or within one solid object. During heat conduction, the hotter region with molecules of higher kinetic energy will randomly collide with low speed molecules in the colder region to induce more energetic vibration. This energy will be transferred to the colder region which eventually causes all molecules in the colder region to vibrate at similar frequency. This is known as heat diffusion. The kinetic energy of the molecules is associated with the temperatures of the region [42]. Depending on the thermal conductivity of the colder region, it may require a larger amount of thermal energy to increase the surface temperature of the colder region.

The heat transfer equation for conduction can be derived and solved using the one-dimensional approximation with appropriate assumptions for a steady-state scenario. The effect of two-dimensional and three-dimensional heat diffusion is briefly discussed in Section 3.2.1, 3.2.2 and 3.2.3, describing its impact on temperature rise and contrast in a thermal analysis.

3.1.2 Convection

Heat convection, on the other hand, involves the heat transfer between a solid surface element and fluid. It is similar to conduction regarding thermal energy transfer between structural molecules. Also, the bulk motion of the fluid is another form of energy transfer in this context. Such fluid motion will contribute to the total heat transfer of convection. In general, stationary fluid will have a lower convection heat transfer coefficient as compared to a moving fluid. This is an important aspect of this study as room temperature is often a major factor for a non-adiabatic system, at which heat dissipation to the surrounding cannot be neglected.

3.2 Transient Heat Conduction in Solids

The theory of thermal detection requires the solving of the general differential heat diffusion equation, governed by Fourier Law:

$$\frac{1}{\alpha} \left(\frac{\partial T}{\partial t} \right) = \left(\frac{\partial^2 T}{\partial x^2} \right) + \left(\frac{\partial^2 T}{\partial y^2} \right) + \left(\frac{\partial^2 T}{\partial z^2} \right) \quad \text{Equation 3.1}$$

where, α is the thermal diffusivity of material, x, y, z are the Cartesian coordinates representation, t is the time variable and T is the temperature. As thermal waves propagate into the material via conduction after heating, the surface temperature will slowly decrease. If a defect is encountered, the reflection and local accumulation of thermal waves will cause a relatively higher temperature over the defective region [29].

For a small size defect, it is important that the three-dimensional approach is used. Otherwise, a one-dimensional approximation is reasonable for most cases [21]. Vavilov et al.[21], showed that metals have a short and specific heat transient time; therefore a good resolution time up to millisecond is required.

3.2.1 One-dimensional approach

The one-dimensional approximation was claimed to be an acceptable method in analysing heat transfer behaviour [21]. When using the one-dimensional approach, it is assumed that lateral heat diffusion is negligible due to the rapidity of thermal events. Therefore, the impact of edge effects was also not accounted for in this part of the analysis [21].

For an adiabatic plate with finite thickness, L heated with a Dirac pulse function (flash heating), the solution is well-known as Equation 3.2. The heat applied was assumed to be uniform and completely absorbed by the surface [44]:

$$T_s = \left(\frac{W\alpha}{kL}\right) [1 + 2 \sum \exp(-n^2 \pi^2 Fo)] \quad \text{Equation 3.2}$$

where T_s is the surface temperature, W is the absorbed energy, k is the sample heat conductivity, L is the sample thickness, $n = 1, 2, 3...$ and Fo represents a dimensionless time. The expression for α and Fo can be expressed as below:

$$\text{Thermal Diffusivity, } \alpha = \frac{k}{\rho c_p} \quad \text{Equation 3.3}$$

$$\text{Fourier Number, } Fo = \left(\frac{\alpha \tau}{L^2}\right) \quad \text{Equation 3.4}$$

with ρ as the material density, C_p as the specific heat capacity of the material, τ as the time constant.

Meanwhile, for a defective area, the above equation transforms into:

$$T_s = \left(\frac{W\alpha}{kL}\right) \left(\frac{1}{1-M}\right) [1 + 2 \sum \exp\left(-n^2 \pi^2 \left(\frac{Fo}{(1-M)^2}\right)\right)] \quad \text{Equation 3.5}$$

where, M refers to the material loss by an expression of $M = 1 - l/L$, l is the remained thickness.

As the time constant approaches infinity, the temperature difference, ΔT between the surface of a non-defective area and defective area can be denoted as:

$$\Delta T = \left(\frac{W\alpha}{kL}\right) \left(\frac{L}{l} - 1\right) \quad \text{Equation 3.6}$$

Meanwhile, for a semi-infinite body that is defect free where the thickness extends to infinite, the surface temperature of the body heated with a uniform instantaneous heat pulse can be derived as below [45]:

$$T(x, t) - T_i = \frac{e_s}{k \sqrt{\frac{\pi t}{\alpha}}} \exp\left(-\frac{x^2}{4\alpha t}\right) \quad \text{Equation 3.7}$$

where, $T(x, t)$ is the temperature response for spatial and temporal variable ($^{\circ}\text{C}$), T_i is the initial temperature ($^{\circ}\text{C}$), e_s is the input energy per unit area (J/m^2) and x is the distance from input source (m).

3.2.2 Two-dimensional approach

For the case of two-dimensional approach, a defect in the plane can be assumed as a slot with infinite length in one direction. The maximum temperature signal is expected to be lower as compared to the one-dimensional approach. This is because lateral heat diffusion and edge effects is considered. The temperature versus spatial profile will have a Gaussian-like distribution [21]. In fact, these defect edge effects will affect the lateral extent of the defect size image [46]. The governing equation for thermal diffusion length describes the extent of this effect. For a small radius error compared to the effective thermal diffusion length, the edge effect will extend from opposite edges inward to the centre and overlap [47]. The effective thermal diffusion length, μ_{eff} is derived as:

$$\mu_{eff} = 2\sqrt{\alpha t} \quad \text{Equation 3.8}$$

The equation describes the effective distance that thermal wave diffuses over a time of interest.

When edge effect occurs, the surface temperature response can no longer be treated or analysed as valid one-dimensional heat diffusion since two-dimensional heat flow is now predominant. These effects on defect sizing will be further discussed and investigated in the thesis results section.

3.2.3 Three-dimensional approach

The three-dimensional approach allows for simulation and detection of defects with any sizes and shapes. When compared to one-dimensional and two-dimensional approach, the three-dimensional approach resulted in the lowest maximum temperature measurements. This is because of the additional lateral heat diffusion. Edge effects have also become more significant due to the effect from the additional coordinate axis. Overall, the maximum temperature signal is weak, proving difficult for measurement to be taken especially for small defect sizes [21].

3.3 Logarithmic Second Order Derivative Method

Among the available techniques, the log second order derivative method is one of the easier and more accurate technique for defect depth measurement [30]. Fundamentally, the heat equation with one-dimensional approximation is solved to find the relationship between temperature change over time and material's local thickness. In this case lateral heat diffusion is assumed to cancel out in the defect-free region [48]. For a semi-infinite homogeneous plate with adiabatic boundary condition and heated by an instantaneous heat pulse, the relevant transient heat transfer equation has been derived as Equation 3.9 [29, 30, 44, 45]. An instantaneous heat pulse, also known as Dirac delta heat pulse, generates a full spectrum of thermal waves of all frequencies. Hence, any derivation of results assumes that the transient solution is characterised by a single frequency component of a certain time of interest [47].

Using temperature responses only from the surface of the subject, the x variable in Equation 3.7 will equate 0, resulting in:

$$T(0, t) - T_i = \frac{e_s}{k \sqrt{\frac{\pi t}{\alpha}}} \quad \text{Equation 3.9}$$

Taking the natural logarithm of Equation 3.9, any small changes in temperature response can be amplified in the log plot. It is able to describe the change in cooling behaviour of the thermal system [30] using Equation 3.10.

$$\ln \Delta T = \ln \frac{e_s \sqrt{\alpha}}{k} - \ln \sqrt{\pi t} \quad \text{Equation 3.10}$$

A defect is usually defined as a substructure discontinuity (void) or a large air gap. Air, at room temperature, has a low thermal conductivity of approximately 0.0257 W/m.K in comparison to metals. During transient cooling, the log graph of Equation 3.10 will have a linear slope of -0.5 as mentioned earlier in the literature review [45]. This represents the heat propagation behaviour in a non-defective region with one-dimensional assumption and adiabatic boundary conditions. This slope value is invariant with material thermal properties, geometry or energy input. In reality, however this decay curve is different due to the stronger effect of three-dimensional conduction [35, 49]. When a defect is present, propagation of thermal waves is inhibited since there is a large mismatch in thermal conductivity between the inspected subject (commonly metal) and air [50]. In this case, the assumption of one-dimensional heat diffusion will no longer be valid [30, 37]. The surface above this defect will experience a rise in temperature compared to surrounding sound regions due to a change in conduction behaviour [35]. Regarding log plot, the linear slope of -0.5 will deviate at a certain time.

This point in time, t^* will indicate the depth at which thermal wave has travelled and reflected off the back surface. It is used to measure the local thickness of material [20, 30, 35].

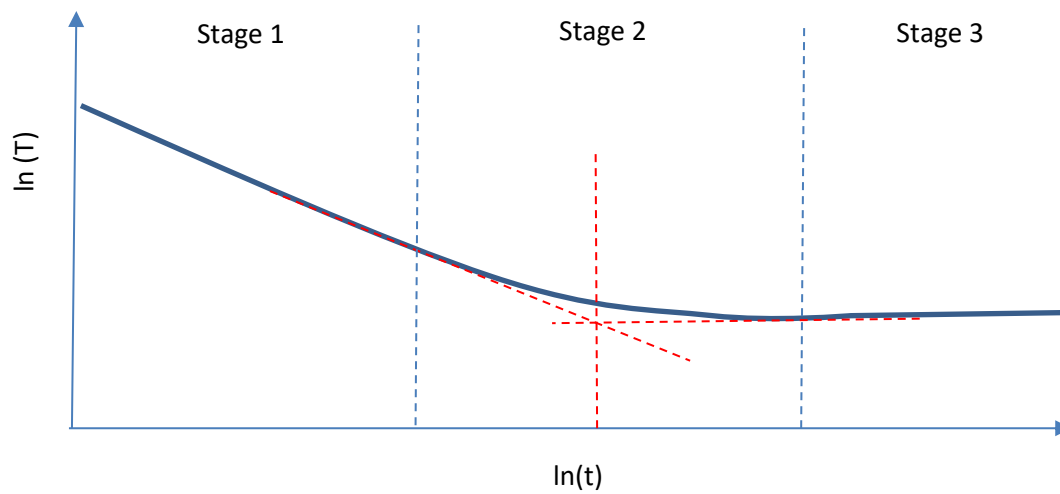


Figure 3.1 Three stages of logarithmic temperature-time decay plot.

The raw natural logarithmic temperature versus time graph can be separated into 3 different stages as seen in Figure 3.1. The initial stage (stage 1) is the -0.5 slope which indicates a semi-infinite medium region where free one-dimensional heat diffusion occurs from the surface of the specimen into the volume [23]. The next stage is the transition from semi-infinite to a finite thickness of the solid where the slope gradually decreases. Finally, the zero slope line refers to the presence of an adiabatic subsurface interface where diffusion is terminated [40]. Balageas [40], suggested that the second derivative method is more complex and inaccurate at times if the defect is laterally limited.

Next, the differentiation of the log temperature and log time plot can provide more significant information. Figure 3.2 best illustrates the 3 types of logarithm plots [31]. Many other studies have also discussed this method using similar plots of graphs [51-53]. The first order derivative represents the cooling rate of a pulsed heated object, while the second order derivative represented the rate of change of cooling rate of the object [30]. Each of these derivative images is able to reveal smaller and deeper defects that are not possible via raw images [39]. An optimum observation frame rate must be selected as temperature contrast of small defects disappears quickly compared to large defects [37-39]. The time at which the inflection point and the maximum point of the first order and second order derivative respectively occurred after heating should ideally be similar to t^* . It is used to determine the local thickness of the object. This is also an indication that the heat from the surface has interacted with the back wall surface [51]. To evaluate the thermal diffusivity instead, the same method can be used, given that the material thickness is known. Equation 3.11 is derived from a series of solution for surface temperature that governs for a sample with finite thickness, L [45]:

$$L = \sqrt{\pi \alpha t^*} \quad \text{Equation 3.11}$$

where, t^* is the measured time when the -0.5 slope deviation occurs. This solution is used for a one-dimensional approximation, making an assumption that no edge effects have occurred.

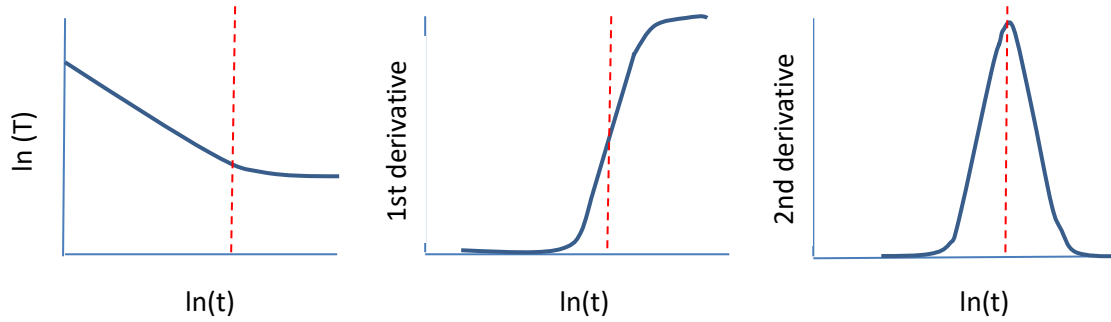


Figure 3.2 Left: Raw temperature data in logarithm form. Middle: First order derivative of log temperature versus log time plot. Right: Second order derivative of log temperature versus log time [30].

Thermal Signal Reconstruction (TSR) utilises the logarithmic second order derivative method to reconstruct each pixel over a sample surface, with a view to display results on the subsurface structure of the sample.

The TSR method collects raw temperature data at each pixel on the inspected surface and transforms them into natural logarithm form. Then, using a least squared fit of low order polynomial such as 4 or 5, the logarithm temperature decay curve can be smoothed and represented by an equation. The selection criteria for polynomial order is determined using the coefficient of determination r^2 where it should be close to unity [40]. The downside of data fitting is the risk of losing essential information. This can be overcome by restricting and sectioning data collected using the Fourier number with the domain size of 0.05 – 1.6, before performing curve fitting [39, 40]. Such setup is able to compress the amount of data for analysis in a few seconds. Equation 3.12 is a layout of the reconstructed surface temperature after being processed by the natural logarithm and the Fourier number time domain.

$$\ln T = a_0 + a_1 \ln t + a_2 (\ln t)^2 + a_3 (\ln t)^3 + \dots + a_n (\ln t)^n \quad \text{Equation 3.12}$$

$$\Delta T(t) = \exp[a_0 + a_1 \ln t + a_2 (\ln t)^2 + a_3 (\ln t)^3 + \dots + a_n (\ln t)^n]$$

There are a few advantages of using the TSR method [23, 30, 39, 48, 49]:

- (i) Increase in spatial and temporal resolutions.
- (ii) Retains the quality of a thermal event.

- (iii) Significant data compression. For instance, storage space is reduced from roughly 49 MB to approximately 5 MB.
- (iv) Provides signals that are unaffected by ambient conditions, surface structure or input heat energy.
- (v) Able to inspect surfaces with low emissivity since reflection effects are reduced.
- (vi) Very good repeatability.
- (vii) Does not need a reference point to identify a defect using temperature response data.

3.4 Full Width Half Maximum (FWHM)

The use of Full Width at Half Maximum (FWHM) technique was introduced by Wetsel and McDonald in 1984 while conducting test runs on photo-thermal imaging resolution [54]. This technique has then been adopted over many other studies attempting to perform subsurface discontinuity sizing. In general, a line profile is drawn across the sample surface with underside defective region and the temperature responses were recorded. The half rise of a temperature-spatial profile at a time of interest is observed to determine the FWHM value [29]. This profile is usually Gaussian-like as seen in Figure 3.3. The peak of the graph indicates the centre point of a defect, while the flat profile represents the sound area of the sample inspected.

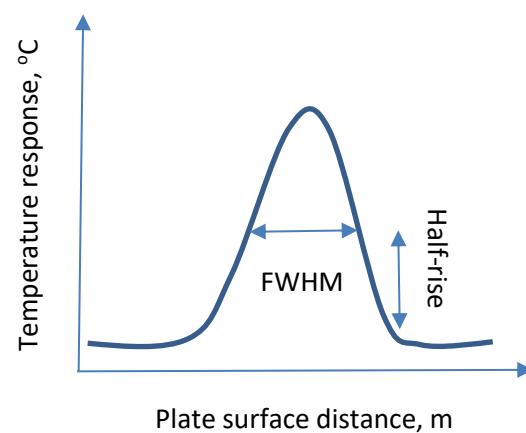


Figure 3.3 Illustration of Gaussian-like shape of a typical FWHM plot.

The one-dimensional analytical model expects that the FWHM measurement shrinks over time. Such phenomenon has been proven experimentally, however at a limiting defect size and depth [47]. This shrinkage is due to the rounding of temperature profile as a result of lateral heat flow above the defect to its adjacent cooler region or underside of crack consequently leading to the gradual drop in temperature [27, 47]. Later, the FWHM measurement is expected to increase due to edge effect overlapping at the centre, causing rapid heat diffusion from the centre of the defect outwards. In fact,

at a longer observation time after heating, the validity of FWHM becomes doubtful as the system transitions from one-dimensional to two-dimensional [46].

To determine the actual defect size, a series of FWHM measurements can be plotted and back-extrapolated to the vertical axis intercept [29, 46]. Each of the FWHM measurement indicates the apparent defect size at the observation time. The most accurate estimation of defect size can be made by accounting for FWHM measurement at a very short period after heating. This is when edge effects are almost non-existent as discussed earlier, which justifies the higher accuracy. Nonetheless, there are concerns for insufficient temperature contrast just after heating [47].

Previous investigations found that for small diameter defects, edge effect is significant for a short period after heating and often triggers early error. In contrast, large diameter defects suffer the same consequence at a later time after heating [47]. In summary, a larger diameter defect is able to accommodate for longer effective thermal diffusion length before encountering overlapping of edge effects.

3.5 Resolution of Thickness Measurement

Equation 3.11 is able to define the local thickness of a sample based on time measurement. By differentiating and rearranging the terms from the equation, the optimal frame rate required to produce a high-resolution result can be obtained. With appropriate derivations and assuming Δt as the frame period, the resolution of thickness can be rewritten as:

$$\frac{\Delta L}{L} = \frac{1}{2m} \quad \text{Equation 3.13}$$

where, m represents the number of frames. Judging by the equation, it can be deduced that the resolution is only affected by the frame number, and it is independent of the material properties. For a near surface defect, the frame numbers required to detect the defect is small as the defect is visible shortly after heating. This will, however, produce a bad resolution. Thus, there is a need to have a sufficiently large frame numbers for better resolution. The time where deviation from -0.5 slope in the temperature profile occurs, t^* should be delayed to a certain extent [37].

3.6 Depth Limit

When attempting to detect deeper defects, the frame numbers used is large since deep defect will be observed at later times after heating. Instead, there is a need to address the issue where temperature changes become too small to be detected at that point. This ultimately denies the ability to measure local thicknesses [37].

Shepard et al., [37] derived that the resolution, $\frac{\Delta L}{L}$ at the maximum thickness can be related as:

$$\frac{\Delta L}{L} = \frac{1}{n+1} \quad \text{Equation 3.14}$$

The value of n from Equation 3.14 is then used to determine the maximum measurable thickness, L_{max} as below:

$$L_{max} = \frac{Q\sqrt{\alpha}}{en\Delta T_{NETD}} \quad \text{Equation 3.15}$$

where ΔT_{NETD} is noise level and Q is the energy absorbed at the surface. In general, as the resolution is relaxed, the maximum measurable thickness increases considerably. A good balance between the noise level and the amount of input energy is necessary [37].

3.7 Minimum Input Energy

For an infrared thermography test, it is important that the amount of thermal energy supplied to the system is sufficient to meet a certain criterion. First and foremost, the temperature rise measured on the sample surface must be at least a few centigrade above ambient conditions [21]. This is shown and tested in Chapter 4, using the transient heat transfer equation for pulsed heating of Equation 3.9.

Next, the temperature contrast on sample surfaces at a longer time after heating has to be larger than the temperature resolution of a commercial infrared camera of 0.1 °C [55]. This implies that a minimum input energy is required to generate such temperature contrast. The relationship is governed by the equation below [21]:

$$W > \frac{kLT_{res}}{\alpha} \quad \text{Equation 3.16}$$

where, k is the thermal conductivity, L is the sample thickness, T_{res} is the temperature resolution and α is the thermal diffusivity.

3.8 Chapter Conclusion

The nature of study for this thesis revolves mainly around the concept of heat transfer. In the beginning, some fundamentals of heat transfer were presented while heat conduction and convection were focused. Rapid conduction occurs when heat is applied to the surface of the test sample and heat energy diffuses into the solid volume. Meanwhile, convection can be observed between the test sample and its surrounding volume of air. Besides that, the differences in approximating the transient heat conduction analysis with one-dimensional, two-dimensional and three-dimensional cases were discussed. Ultimately, the three-dimensional approximation is the best approach for small defect

identification, however, having issues with small temperature contrast. Using the one-dimensional approximation, two existing methods are utilised to determine the depth and size of an underside defect. First, the second order peak derivative uses the second derivative of a logarithmic temperature-time plot to find a point in time where the transient cooling behaviour begins to deviate. This is used to identify the depth of the defect or the local thickness of a test sample. Next, the Full-Width Half Maximum (FWHM) technique is used to examine surface temperature responses concerning the spatial profile of the test sample. By plotting local temperature measurements and its respective coordinate position across the test sample, an FWHM measurement can be obtained. Using the back-extrapolation method on a range of FWHM values at different observation times, the actual defect size was predicted to a certain accuracy. This chapter also briefly introduced theories behind the resolution of thickness measurement, measurable depth limit and minimum input energy required.

In the next chapter, the setup for computational modelling will be thoroughly discussed. The justification to the setup of boundary conditions will be outlined. In addition, necessary model validation will be displayed and analysed.

4. Model Setup and Validation

The main objective of this thesis can be achieved with two main approaches, which are experimental or computational modelling. The previous chapter showed that raw data collected from either experimental or computational test could be used to find the defect depth and sizes using relevant methodologies. For the course of this thesis, the focus will lie on computational work with the use of FEMAP, NX 7.5 and Nastran Autodesk. The use of computational simulation is a decent approximation to an actual picture, therefore equally important as an experimental method.

This section will discuss the full setup and process required to investigate the ability of moving heat source in predicting underside defect size and depth. Prior to that, the stationary heating case will be investigated. The chapter will carefully describe the procedures in creating a moving heat source simulation up to analysing the results. On top of that, the chapter will also show validation tests in comparison to previous works and theoretical models. The abbreviations and definitions used in this thesis can be found in Table 4.1 and Figure 4.1.

Table 4.1 Abbreviations and definitions.

Underside defect size	D_s
Defect depth measured from plate surface	d
Overall plate thickness	t_p
Material thickness reduction	$t_R = t_p - d$
Width of heating line strip	l_s
Estimated underside defect size	D_{SE}
Plate model with thickness 2 mm or less	Thin plates
Plate model with thickness larger than 2 mm	Thick plates
A few milliseconds after heating	Short observation time
Observation time at 1.0 s or more after heating	Late observation time

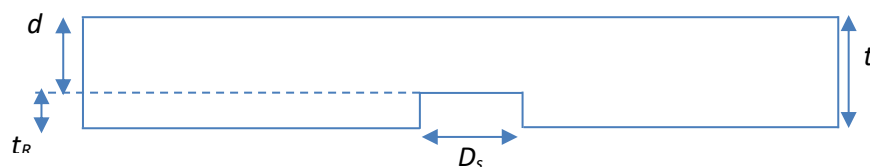


Figure 4.1 Two-dimensional front view of the plate model with an underside defect.

4.1 Model Setup

NX 7.5 was used as the Computer Aided Drawing tool to sketch all the different dimensions of models used for the purpose of this thesis. The shape of the model was referred to the rail base, however in a much simpler form of rectangular plates. Concerning the dimensions, the length of the plate (p) was set at 120 mm and width (w) at 20 mm as shown in Figure 4.3. For a short plate (finite) with large D_s , the temperature-spatial graph is invalid at late observation time. This is due to the effect of plate model edges, affecting the overall temperature contrast changes. Therefore, a sufficiently long plate is necessary for this study to avoid such error and limitation.

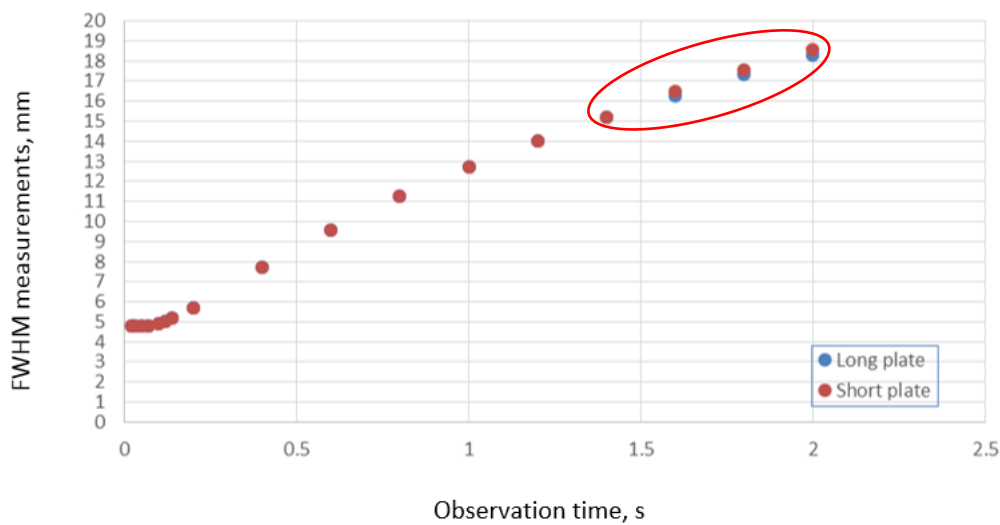


Figure 4.2 Comparison of FWHM measurements for long and short plates.

According to Figure 4.2 and the early measurements on FWHM, both long ($p = 120$ mm) and short plate ($p = 100$ mm) cases show similarity. The use of long plates allow for a larger range of valid FWHM measurements as the effect of plate model edges is delayed. The region circled in red indicates the slight differences in results obtained for both tests. In terms of defect size prediction, both sets of plate length yield matching results. An initial test was also conducted for wider plates ($w > 20$ mm), however, the simulation time and disk space was too large. In addition, it had no impact on the measured temperature responses over the defective region. Figure 4.3 is a two-dimensional sketch of the plate model.

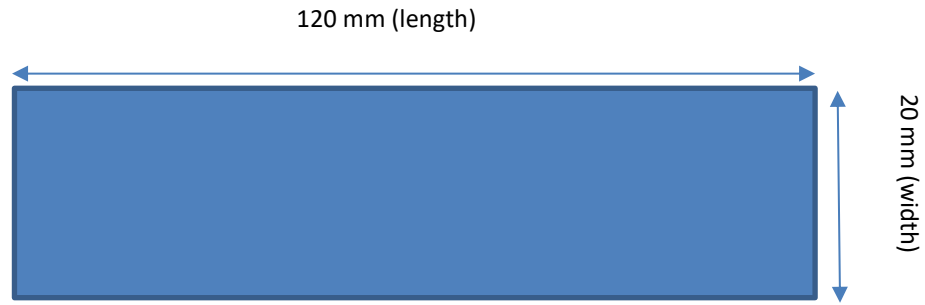


Figure 4.3 Top view of plate model.

The thickness of the plate was one of the many varying variables. As the thesis progress, the thickness, t_p changed between 1.5 mm, 2 mm, 4 mm, 6 mm, and 8 mm. The maximum thickness (8 mm) resembles the typical size of a rail track base, while the minimum thickness (1.5 mm) was used for simulation validation with existing work [47].

To create a defect-like shape for this computational work, a simple rectangular cut-out was modelled at the underside of the plate model [20]. The use of the rectangular shape will eliminate any effect arising from a complex geometry with curvatures. The defect can be seen as a substructure discontinuity, where it will obstruct the propagation of the thermal wave. It is important to note that the heat flow behaviour for a defect and crack-like defect is different in terms of effectively trapping heat [47]. A range of defect dimensions was drafted and implemented in Table 4.2. The arrangement in the table does not indicate the pairings of each dimension.

Table 4.2 Range of dimensions for the defect at the underside of plate model. The dimension symbols can be referred at Figure 4.1.

Width (D_S)	3 mm	5 mm	6 mm	8 mm	10 mm	20 mm
Thickness (t_R)	0.5 mm	2 mm	4 mm	6 mm	7 mm	

To create a moving heat source, the model surface at the opposite side of the defect was ‘face divided’ into even segments. The width of segments, l_s was set at 5 mm, 10 mm or 15 mm, to simulate an intended heating speed. The calculation for the heating speed can be found in Appendix A. Alternatively, the heating duration on each segment also affects the final heating speed. This is discussed in Section 4.2.2. A screenshot of the model with 5 mm segments is shown in Figure 4.4.

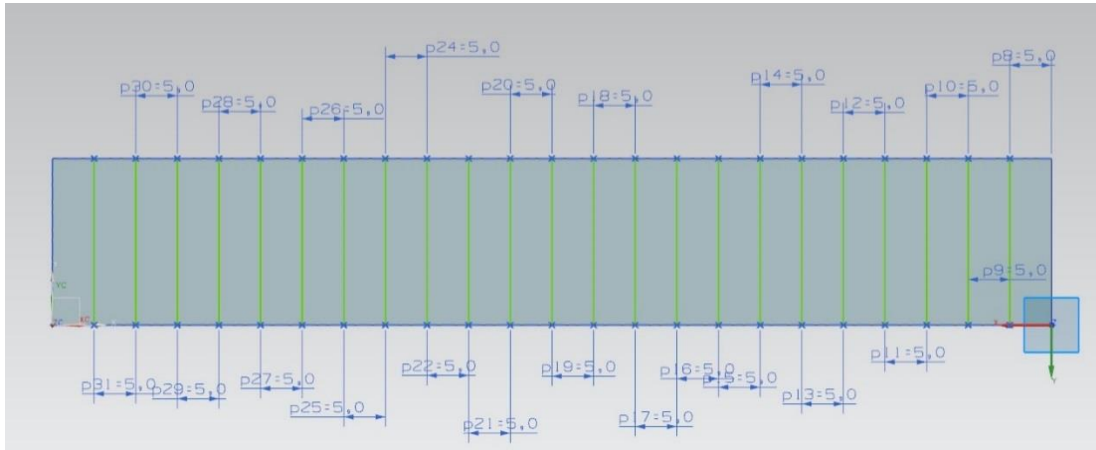


Figure 4.4 Surface divided to set up for moving heat source test. Each segment is 5 mm in width.

The defects created in the test model for the moving heat source test had similar dimensions to Table 4.2. The final sketched model was exported as a parasolid to FEMAP for pre-processing procedures.

4.2 Simulation Setup

The pre-processing stage of this research study mainly involves the use of FEMAP (Finite Element Modelling and Post-processing). FEMAP is one of the many programs that has the advantage of allowing the import and export of solid geometry and finite element model. For example, a model constructed in ANSYS and NX can be directly imported into FEMAP for pre-processing. It is also possible to construct any geometrical changes to the imported solid in FEMAP. In terms of its feasibility in thermal analysis, FEMAP is able to generate a conduction network automatically compared to other programs with manual settings. Lastly, FEMAP offers an easy to use interface where users may improve the element details in tight regions with the available meshing tools [57].

4.2.1 Material properties

The test plate model was set with solid element type in FEMAP and thermal characteristics of a mild steel [47, 56]. The material choice of selection was aimed to closely match the rail track base [58]. FEMAP was pre-set to operate in SI units instead of the default English units. Table 4.3 shows the main properties used for the transient thermal analysis in this study. The physical properties were not emphasised in this context as it was assumed insignificant to the thermal behaviour of the system.

Table 4.3 Thermal properties of mild steel used in simulation [47].

Thermal conductivity, k (W/m.K)	64
Density, ρ (kg/m ³)	7850
Specific heat capacity, C_p (J/kg.K)	580
Thermal diffusivity, α (m ² /s)	1.4057×10^{-5}
Reference temperature, T_{Ref} (°C)	25

4.2.2 Model constraints

Model constraints in this study are an important aspect that affects the simulation outcome drastically. To simulate a stationary heat source, the full surface of the plate was heat loaded simultaneously with a heat flux of 25 MW/m² that is assumed to be absorbed in 100% efficiency. The heating period was set at 2 ms in Figure 4.5 to simulate Dirac delta heating function [23] at which the effect of frequency was negligible [46]. According to Equation 3.16, the minimum required input energy was found to be approximately 4,000 J for this simulation test (refer Appendix B for detailed calculation). Given the heating function in Figure 4.5, the total heat input of 25,000 J was much greater than the minimum requirement. This assures a sufficient temperature rise during simulation. A small temperature rise will otherwise lead to a small temperature contrast between the sound and defective area. Consequently, the measurements of FWHM will have low accuracy. The preferred minimum temperature contrast was at least 0.1°C based on the resolution of most commercial IR camera [21, 55].

For moving heat source test, each segment was heated sequentially. The first segment was initially heated for 2 ms (Figure 4.6). Then, the adjacent segment was heated after a 1 ms time delay (Figure 4.7). This continuous procedure terminates after heat was applied to the full plate surface. The heat flux used for moving heat source test was set at 25 MW/m², similar to stationary heating. To achieve an intended heating speed, the segment sizes (as discussed in Section 4.1) or heating duration were modified accordingly. The heating duration applied on each segment was varied between 1 ms, 1.6 ms and 2 ms.

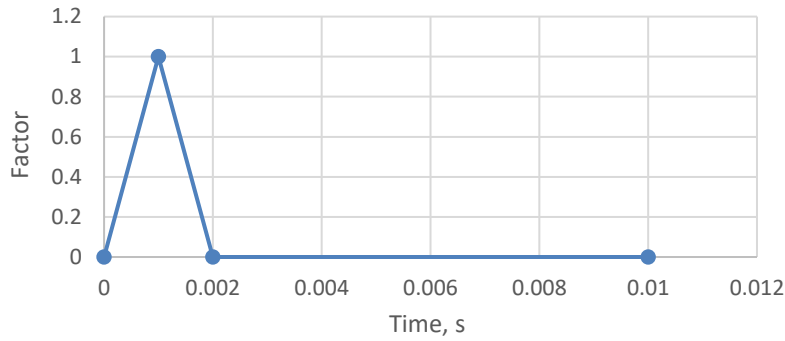


Figure 4.5 Heating period for a stationary heating source.

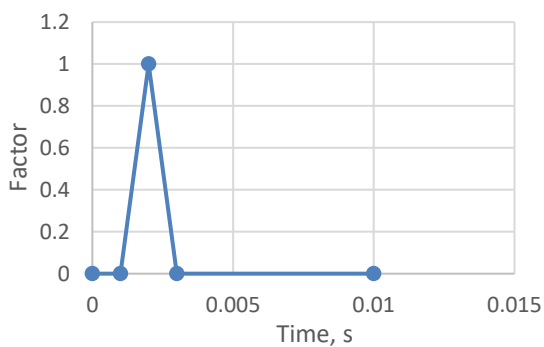


Figure 4.6 Heating period for segment 1 of moving heat source test.

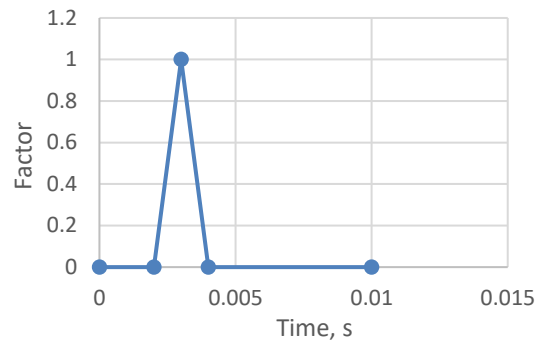


Figure 4.7 Heating period for segment 2 (adjacent to segment 1 in Figure 4.6) of moving heat source test (1 ms delay).

Apart from the discussed loading conditions, it is also necessary to include some essential boundary conditions. To construct the model validation test, an adiabatic system was created with by setting all surfaces to zero heat flux. This is shown and discussed later in Section 4.4. For this test, the similar heating load was used. Later, the adiabatic system was removed and modified to simulate a realistic setup. Convection was taken into account with an ambient temperature set to 25 °C and heat transfer coefficient of air at 20 W/m²K [47]. This was applied to all surfaces of the model. Lastly, the initial condition of room temperature 25 °C was used.

4.2.3 Mesh setup

The setting up of the mesh required appropriate partitioning of the model in FEMAP. This allows the mesh mapping of opposite surfaces to create a uniform mesh [20]. It can be achieved using the ‘split point to edge’ function, ‘embed surface’ and ‘slice’ option in FEMAP. A hexagonal mesh technique is also used for this symmetrical model. Figure 4.8 shows the non-uniform temperature distribution

when tetrahedral meshing was used. This is preferred over the tetrahedral meshing that was unable to simulate the essential assumption of uniform heating. In terms of mesh sizing, a meshing convergence test is carried out to evaluate the feasibility of various mesh sizes.

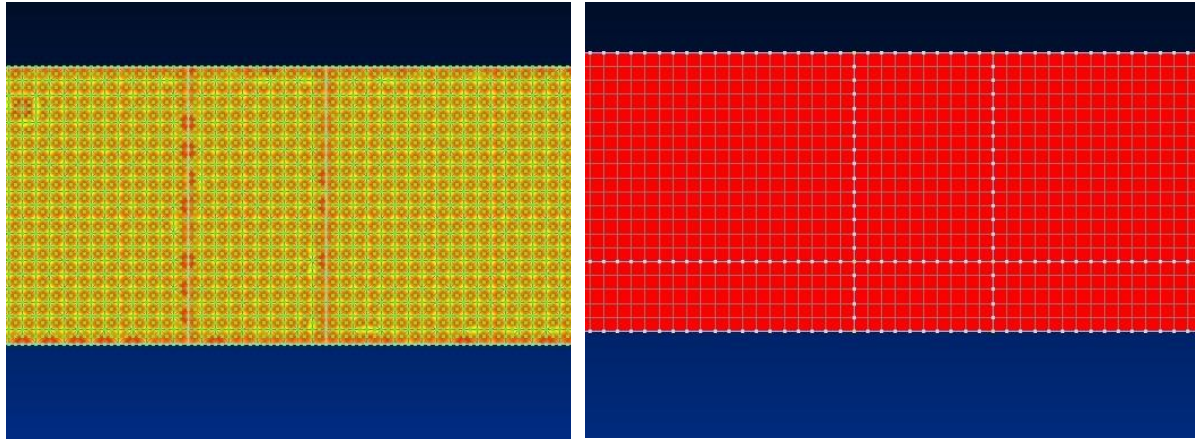


Figure 4.8 (Left) Tetrahedral meshing - uneven heating. (Right) Hexagonal meshing - uniform heating.

The objective of a mesh convergence test is to verify that the FWHM measurement results eventually converges with the increase in mesh density for a valid solution [43, 59]. This is achieved by comparing the number of elements in the system to the convergence of FWHM measurement at $t = 0.1$ s after heating. The various meshing configurations tested can be found in Table 4.4. Apart from the use of different mesh sizes, all other variables remain unchanged. This includes a heat flux of 25 MW/m^2 , heating duration of 2 ms, heat transfer coefficient of air at $20 \text{ W/m}^2\text{K}$ and initial surface temperature of 25°C .

Table 4.4 Variables for meshing convergence test.

Global mesh size	Number of nodes	Number of elements	FWHM measurement
0.4 mm	124740	163454	11.46 mm
0.5 mm	65590	90008	11.53 mm
0.5 mm	85393	111848	11.53 mm
1.0 mm	11817	18324	11.48 mm
1.5 mm	3810	6620	11.42 mm
2.0 mm	2444	4320	11.14 mm

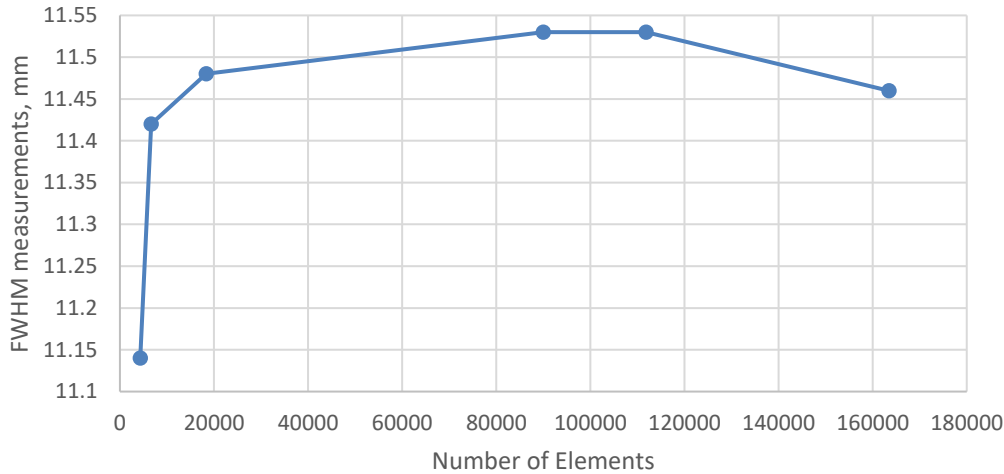


Figure 4.9 FWHM measurements at $t = 0.1$ s after heating for a range of element numbers.

Table 4.4 and Figure 4.9 show that at 0.1 s after heating, most of the measured FWHM values fell between 11.45 mm and 11.55 mm, which is within 1% of each other. A global mesh size of 1.5 mm (6620 number of elements) and 2.0 mm (4320 number of elements) resulted in FWHM measurement that seemed like an outlier to the plot. For the test with 163454 number of elements, the drop in measured FWHM is likely to be contributed by the predominant effect of lateral heat diffusion as a result of small mesh size. Therefore, a global mesh size of 1.0 mm and a minimum of 2 elements can be seen as the minimum meshing size for this study. It allows the careful analysis of small regions.

4.2.4 Analysis Manager

To complete the simulation setup, the analysis is set to perform a transient thermal analysis. A step control of constant interval with 2000 time steps at 1 ms initial and subsequent time interval increment is used to result in a total observation time of 2 s. This period of observation is theoretically sufficient for thermal energy to diffuse through a maximum thickness of 9.4 mm according to Equation 3.11. The 1 ms time interval was chosen in correspondence to short heating function of a few milliseconds. It was also used to attempt detection of small defect which often has a short period of observable temperature contrast [21, 39]. Regarding experiments, the observation time increment is dependent on the camera frame rate whereas the spatial resolution of the camera maps out the meshing pattern across the inspected surface [29].

4.3 Nodal Results

The main form of data collected from this simulation is temperature responses, coordinate positions and observation time. In this study, a line is drawn across the model surface, directly above the underside defect for data recording. This is implemented to reduce data storage size and data

extraction time. Figure 4.10 shows the exact position of the line drawn for results extraction. The rectangular region indicates the defective area at the underside of the model.

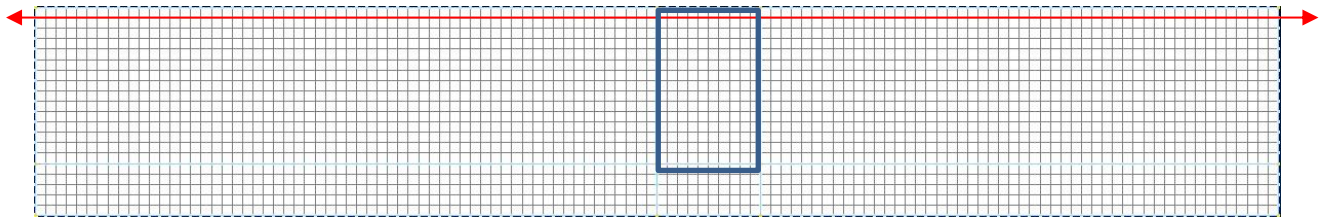


Figure 4.10 Top view of the plate model with the location where nodal results were recorded (red line).

As seen in Figure 4.10, the temperature responses of each node along the ‘red line’ were recorded for every time step. In addition, the respective coordinate positions were tabulated. This data was then exported to Excel and further processed in MATLAB. The MATLAB script can be found in Appendix C.

A short study was conducted to identify the extent and effect of edge effects due to the size of the defect. These findings were helpful in simplifying the three-dimensional model by making appropriate assumptions.

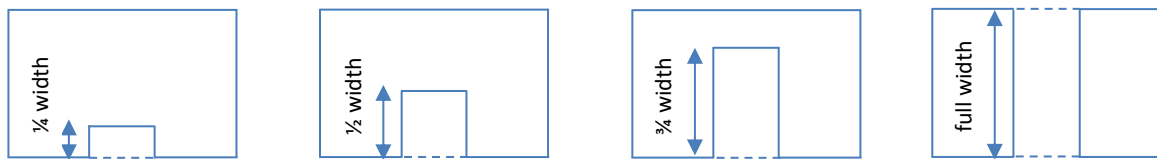


Figure 4.11 Bottom view: Edge effect tests by varying the defect length. (left to right: $\frac{1}{4}$ width, $\frac{1}{2}$ width, $\frac{3}{4}$ width and full width)

The arrows in Figure 4.11 indicate the change in defect length across the width of the plate. It varies between $\frac{1}{4}$ width, $\frac{1}{2}$ width, $\frac{3}{4}$ width and full width. For this test, the nodal results were collected at the similar position as Figure 4.10. When comparing results for all cases, it was found that the $\frac{1}{4}$ width setup had a rapid drop in temperature contrasts and maximum temperature. The FWHM measurements enlarged rapidly after reaching a minimum value. Meanwhile, the test cases for other defect lengths displayed similar results with each other, that differed from the $\frac{1}{4}$ width test. For all cases, edge effect from the side lengths of the defect influences the results. As the defect becomes smaller (i.e. $\frac{1}{4}$ width), the edge effect gradually accounts for all edges of the defect, creating a more significant impact than larger width sizes. This is an indication that the position of nodal observation is affected by plate edges. Given that the study utilises the same line of nodal observation, therefore all results were expected to have a similar relative inaccuracy.

4.3.1 Defect depth

The two main parameters to be measured in this thesis are the depth and size of the defect. First, the depth of the defect is determined using the second order peak derivative method (refer Chapter 3). A polynomial order of 9 is used instead of the recommended 4 or 5 to best fit the curve before performing first order and second order derivatives. This is due to the better coefficient of determination while ensuring that most data points were taken into consideration for analysis. Using the information on the nodal coordinate position and its calculated local thickness, an underside defect can be detected. Moreover, the depth of the defect can be predicted. From the second order peak derivative test method an example of the results is shown in Figure 4.12.

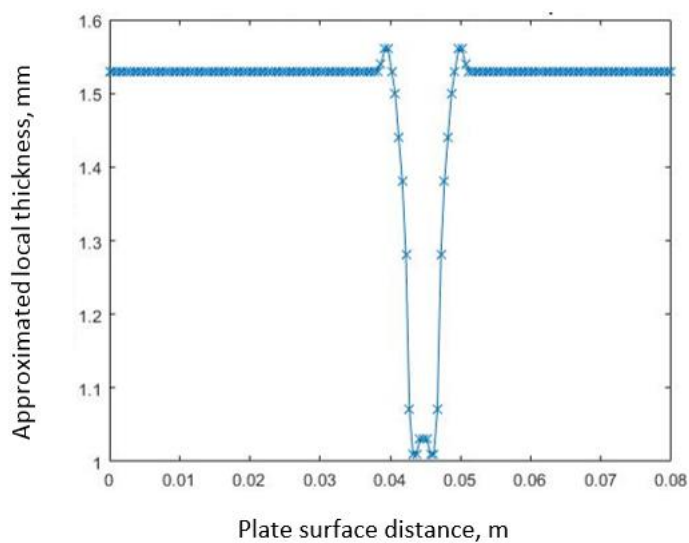


Figure 4.12 Results from the second order peak derivative with the local material thickness of each node. The uneven structure thickness (material thinning) was also displayed.

The two small peaks found on the graph were caused by the defect edges and the partitioning setup for meshing. Otherwise, the plot has successfully mapped the substructure of the actual model by using temperature responses from the plate surface.

4.3.2 Defect size

Defect sizes were estimated using the Full-Width Half Maximum (FWHM) method. The temperature response of each node at a point in time after heating was plotted against its respective coordinate position. In order to measure an FWHM value, the linear interpolation method was used on the temperature-spatial data. Gaussian and Fourier series curve fitting were also attempted for the FWHM method. Nevertheless, these techniques constantly resulted in inaccuracy and inconsistency as depicted in Figure 4.13 and Figure 4.14.

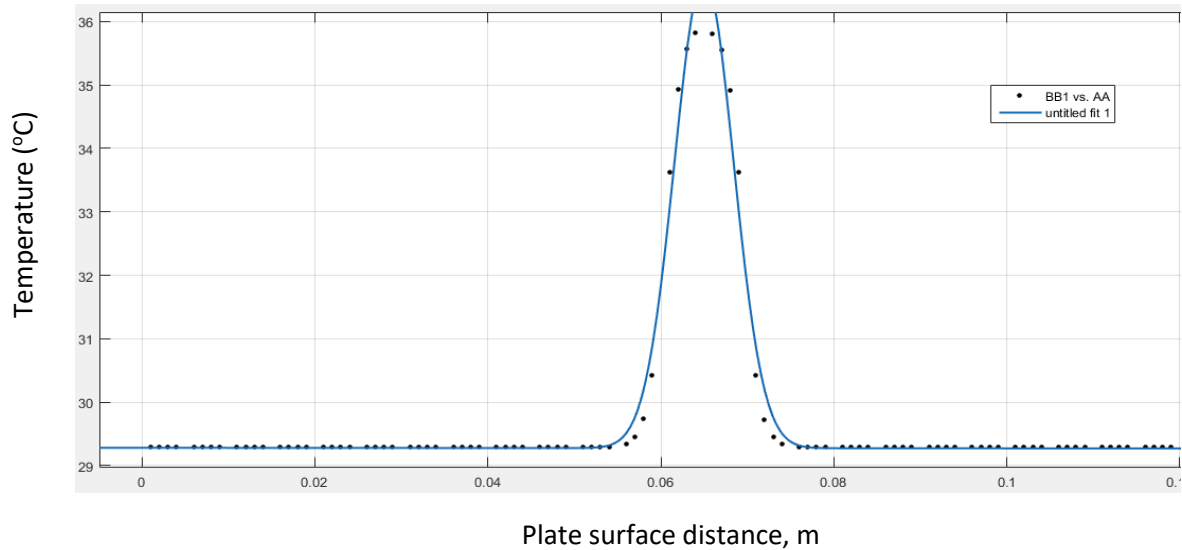


Figure 4.13 Gaussian curve fitting - the curve fit constantly exceeds the maximum point of the plot.

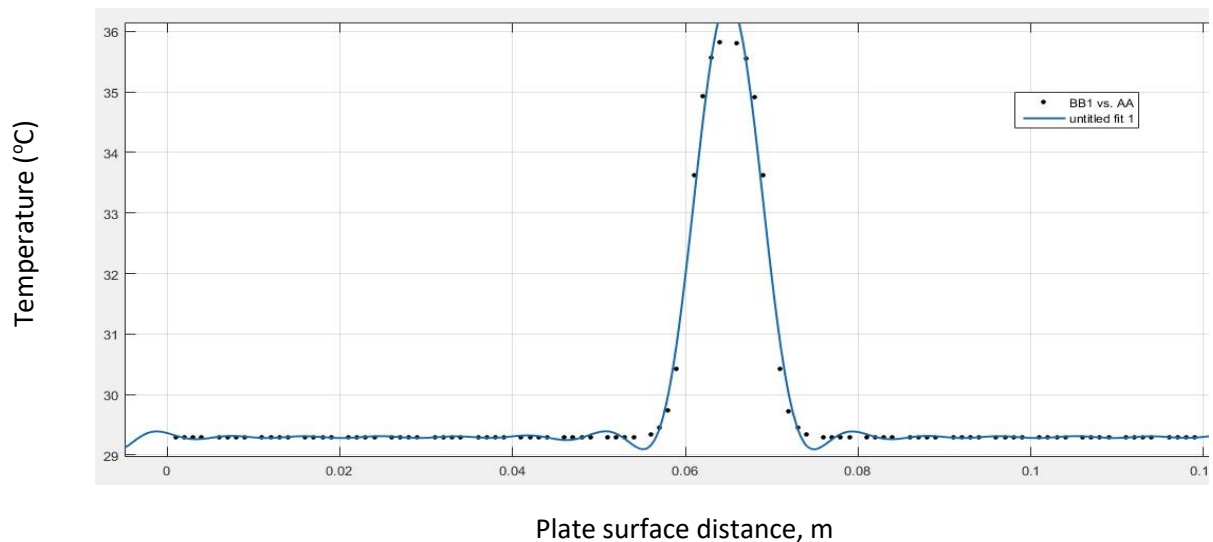


Figure 4.14 Fourier curve fitting (8th order) - curve fit exceeds maximum points and has wobble ends.

The FWHM values were measured and plotted against a range of observation time. However, some of the FWHM measurements were invalid due to low contrast at final observation time, for example in Figure 4.15. A plot with measurable FWHM requires significant temperature contrast at optimum observation time in Figure 4.16. In general, an initial time step interval of 10 was taken for data recording, followed by a time step interval of 100 and 200. For result sets with temperature contrast lesser than 0.1 °C, the data is eliminated as they were deemed insufficient for a valid FWHM measurement. After the tabulation of multiple FWHM values (Figure 4.17), the actual underside defect size was predicted using the back-extrapolation procedure.

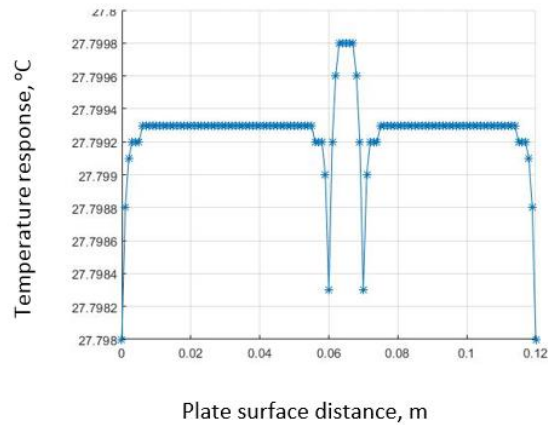


Figure 4.15 Low temperature contrast at observation time of 0.1 s.

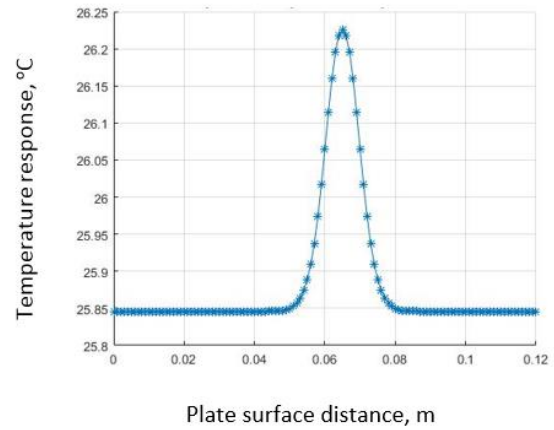


Figure 4.16 Larger temperature contrast at observation time of 1.0 s. This is a typical temperature versus spatial graph for FWHM measurement.

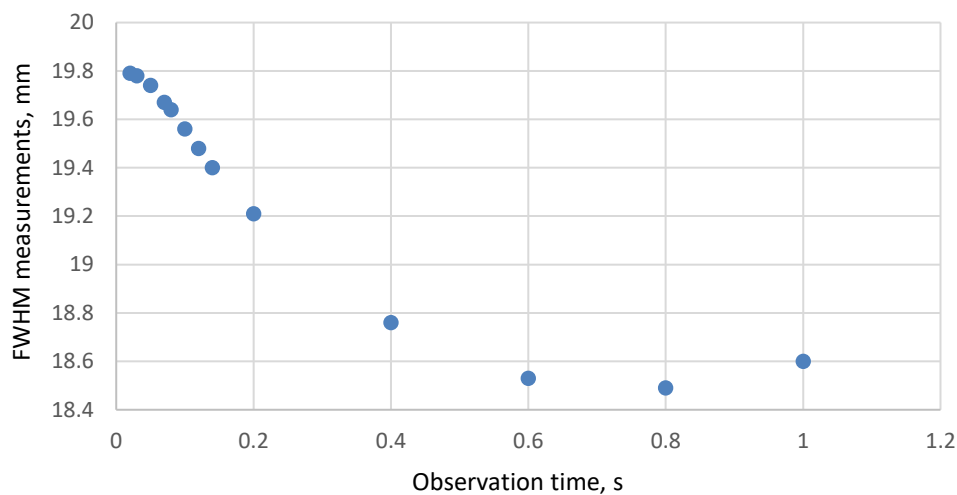


Figure 4.17 A plot for FWHM measurements obtained from Figure 4.16 at a range of observation time. The y-intercept is the predicted defect size.

The results for stationary heating only required simple analysis in which temperature responses were recorded and plotted where necessary. However, this is not the case for moving heat source results as they require additional modifications. Heating time delay that was introduced to simulate a motion heating has to be removed before analysis can be made. This is an important aspect especially during the early time as the temperature responses were strongly affected. Each face segment in the moving heat source model is separated by a fixed heating time delay. This can be removed by subtracting the product of segments away from the first segment and heating time delay constant from the observation time of temperature responses. The resulting set of temperature responses will be

equivalent to a stationary heating setup [23]. Figure 4.18 shows the original temperature profile as a result of motion heating during early observation time. The starting point of heating resulted in a higher rise in temperature as compared to the end point of heating. Meanwhile, Figure 4.19 shows the temperature profile at later observation time where the effect of motion heating has diminished.

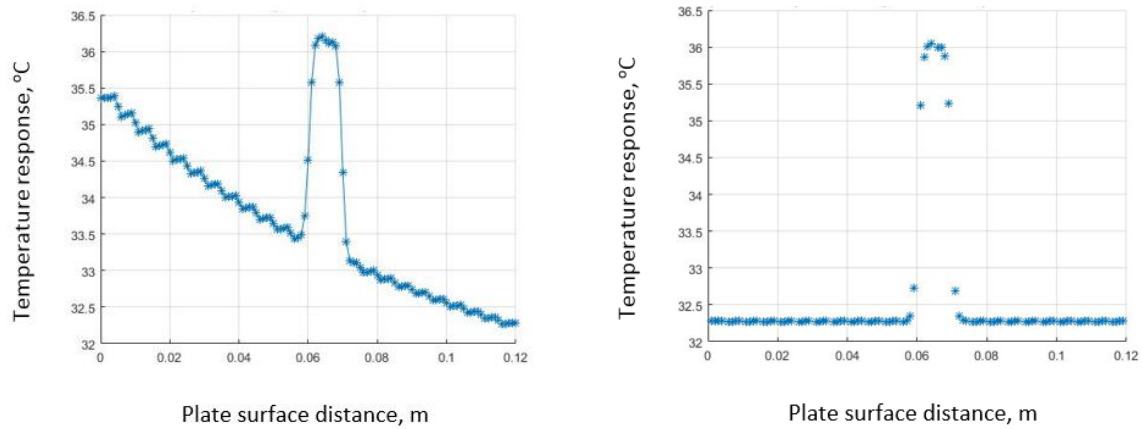


Figure 4.18 Temperature response during the early time for moving heat source test: (left) original plot, (right) plot with time delay removed.

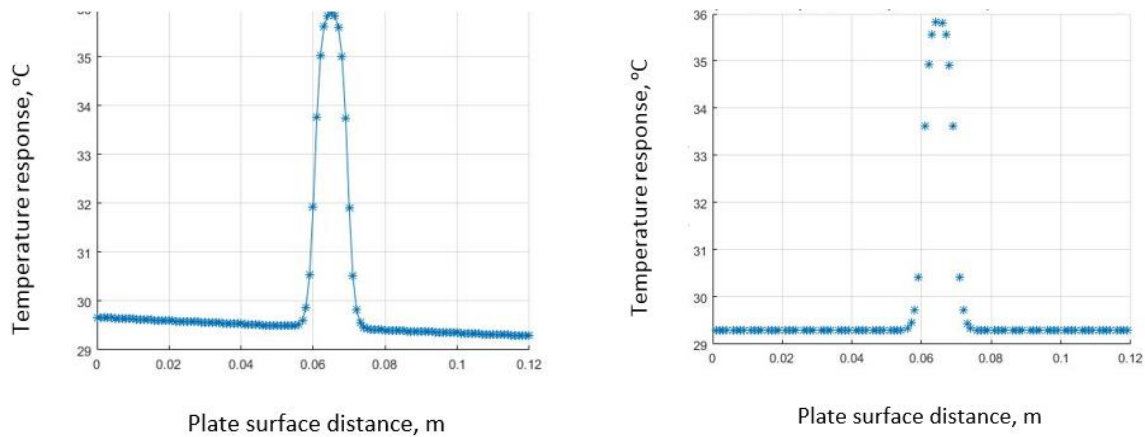


Figure 4.19 Temperature response at late observation time for moving heat source test: (left) original plot, (right) plot with time delay removed.

4.4 Comparison to Mathematical Model I

A model was set up with an adiabatic system where no heat loss occurs to the surrounding, to test for its validity with theoretical model. Given that the input heat flux is 25 MW/m^2 with a heating period of 2 ms in a triangular waveform, the total yielded thermal energy is 2500 J/m^2 . Using the transient heat transfer equation discussed in Section 3.2, the expected surface temperature of the simulated model can be calculated. The thermal properties used for this validation test is based on Table 4.3.

Nonetheless, this comparison becomes invalid at long observation time as a result of the deviation from theoretical assumptions.

Assuming that the initial surface temperature is 25 °C, the subsequent evaluated theoretical surface temperatures was summarised in Table 4.5.

Table 4.5 Theoretical temperatures at different observation time and thermal energy application.

Thermal energy (J/m ²)	2500	25 000	250 000
t = 0.1 s	25.26 °C	27.6 °C	51 °C
t = 1.0 s	25.08 °C	25.83 °C	33.3 °C

First, a random point was selected on the plate surface. Then, the output temperature response of the selected point was recorded at an observation time of 0.01 s, 0.1 s and 0.2 s after heat is removed. Using this information, a comparison was made with theoretical calculation. Temperature responses later than 1.25 s are not accounted for as the infinite plate assumption would no longer be valid. While recording temperature data, it is also important to consider the heating duration. For instance, temperature response at 0.2 s after a heating period of 2 ms must be collected at an observation time of 0.202 s.

Table 4.6 Comparison of theoretical calculated surface temperature and simulated surface temperature at different observation time.

Observation time	Theoretical Temperature	Simulated Temperature	Absolute differences	Percentage error with respect to theory
0.01 s	33.26 °C	33.43 °C	0.17 °C	0.51%
0.1 s	27.59 °C	27.73 °C	0.14 °C	0.51%
0.2 s	26.85 °C	26.88 °C	0.03 °C	0.11%

Table 4.6 shows that for short observation time, the absolute differences between the theoretical and simulated temperature are small. The calculated percentage differences were smaller than 1%. At a longer period of time after heating, these differences grew smaller. It can be deduced that the setup

and constraints for this model are appropriate since the theoretical and simulated temperature responses were closely matched. From there, the model was improved to a realistic model.

4.5 Comparison to Mathematical Model II

The second part of model validation was to address Equation 3.10 that will be widely utilised in this thesis. This is done by proving the similarity between initial model setup and anticipated outcome governed by the theoretical equations.

First, an infinitely thick test model of 50 mm was prepared with a surface dimension of 120 mm x 20 mm. For the purpose of validation, no defect was constructed at the underside of the model. It was a defect free model in ideal cubic shape. Next, the model constraints set up for Finite Element Analysis was tailored to match the assumptions used to derive the theoretical Equation 3.10. This included adiabatic boundary conditions, uniform heating, initial ambient conditions and stationary pulsed heat source. Other setups such as meshing option and observation period were similar to the general setup in this study. During data collection, four points at random location across the model surface was used for measurement. Observations at the edges of the model were not considered.

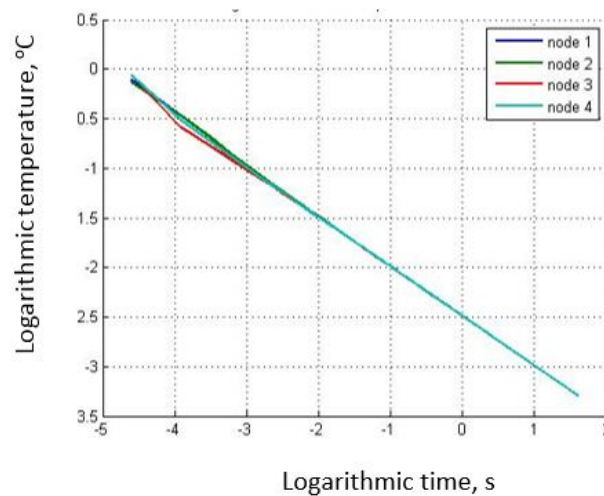


Figure 4.20 Log temperature-time plot for 4 nodal points across the surface of the sample model.

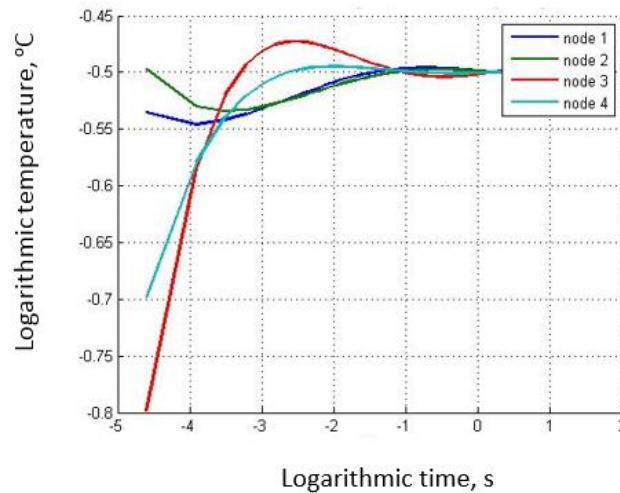


Figure 4.21 First order derivative of the log temperature-time plots of Figure 4.20.

The computational simulation for the infinitely thick plate showed very close resemblance to theoretical expectation. In Figure 4.20, the slope of the log temperature-time graph was constant with no deviation, hence suggesting the absence of any subsurface discontinuity over the given period of observation time [29]. If the observation time was extended to a longer time, a slope deviation would appear to indicate an underside surface boundary. Meanwhile, Figure 4.21 showed that the slope of the previous graph was at approximately -0.5. This is exactly matching with the theoretical derivation. The initial variation in slopes is explained by the short period of heat saturation just after heating was removed.

4.6 Chapter Conclusion

This chapter thoroughly outlined the procedures taken to achieve the objectives present in this study. A rail base-like CAD model was first sketched in a simplified form and a rectangular-shaped defect was created at the underside of the model. The investigated plate sizes and its defect were both shown. Then, meshing convergence was performed to ensure quality meshing. The constraints for the model were carefully set up to meet the criteria of a theoretical model. Furthermore, validations were conducted in two aspects. First, the local nodal temperature responses were compared with a mathematical model. Second, the comparison between the cooling rate of the plate surface and the established theoretical equation was conducted. Both tests were successful, indicating the validity of the initial model setup. Later, the model was modified to simulate a more realistic circumstance at which convection is present. In terms of data collection, a consistent line was drawn across the model surface for analysis of all cases. The moving heat source test was performed by dividing the model surface into equal segments. Subsequently, the heat was applied to each segment sequentially, governed by a constant heating time delay. The delay and the width of the segments are used to

calculate the heating speed. In conclusion, justification of the finite element analysis setup for this study has been discussed.

The following chapter will present computational modelling results for a stationary heat source. The defect depths and sizes will be predicted using the methodology from Chapter 3, then compared to its actual values. Finally, the validity of each results was also discussed.

5. Stationary Heating

The advantages of using infrared thermography for defect detection have been provided in Chapter 2. It was also discussed that subsequent post-processing techniques were required upon simulation to convert raw temperature data into quantitative and qualitative results. Using this knowledge and literature review, an initial investigation was attempted by testing simulation models with stationary heat source. This is an important step to provide in-depth knowledge on the analysis of stationary heating for detecting underside defects using available methodologies. These understandings will later be utilised in a similar manner to study the use of moving heat source in measuring defect quantitatively. Ultimately, two main methods were widely used in this thesis: the second order peak derivative and Full-Width Half Maximum (FWHM).

The second order peak derivative was discovered to be useful in determining the local thicknesses of a plate model. This method was found to be more advantageous over other existing methods as discussed in Chapter 3. The idea of this method is to locate the point where transient cooling deviates from the one-dimensional assumption. This can be achieved by evaluating the peak at the second order derivative of a logarithmic temperature-time plot. Using the relevant equation, the local thicknesses across the plate model can be determined. The FWHM method meanwhile was aimed to perform predictions on underside defect sizes. A series of FWHM measurements at different observation time was initially measured. Subsequently, these data were plotted and back-extrapolated to obtain a prediction of actual defect size.

The use of these two methods in the investigation of stationary heat source is preliminary to the testing on moving heat source. The results in this chapter will be set as a reference and comparison model for moving heat source test. Also, many of the limitations in stationary heating can be correlated to the moving heat source setting. The simulations were used to determine the effect of defect depth location and size on defect prediction accuracy using surface temperature responses.

5.1 Defect Depth Prediction

Earlier, the depth of a defect in a plate is estimated using the second order peak derivative method. For each node on the drawn line profile (refer Section 4.3), the temperature-time relationship was recorded. These data were then converted to its natural logarithmic form before performing second order derivatives. The time at which the peak of the second order derivative graph occurred was used to calculate the local thicknesses across the model surface. If a defect was present, a drop in the material thickness profile could be observed. The depth of the defect corresponds to the local thickness measurement at that point.

5.1.1 Thin plate test

A plate thickness of 1.5 mm was inserted with a defect d of 1 mm as an initial study. Using a 2 ms pulse heat source, the resulting surface temperature responses were analysed via the second order peak derivative method. The local thickness of each node across the drawn line profile was determined. Figure 5.1 shows the transient cooling behaviour for a simulated D_s of 5 mm.

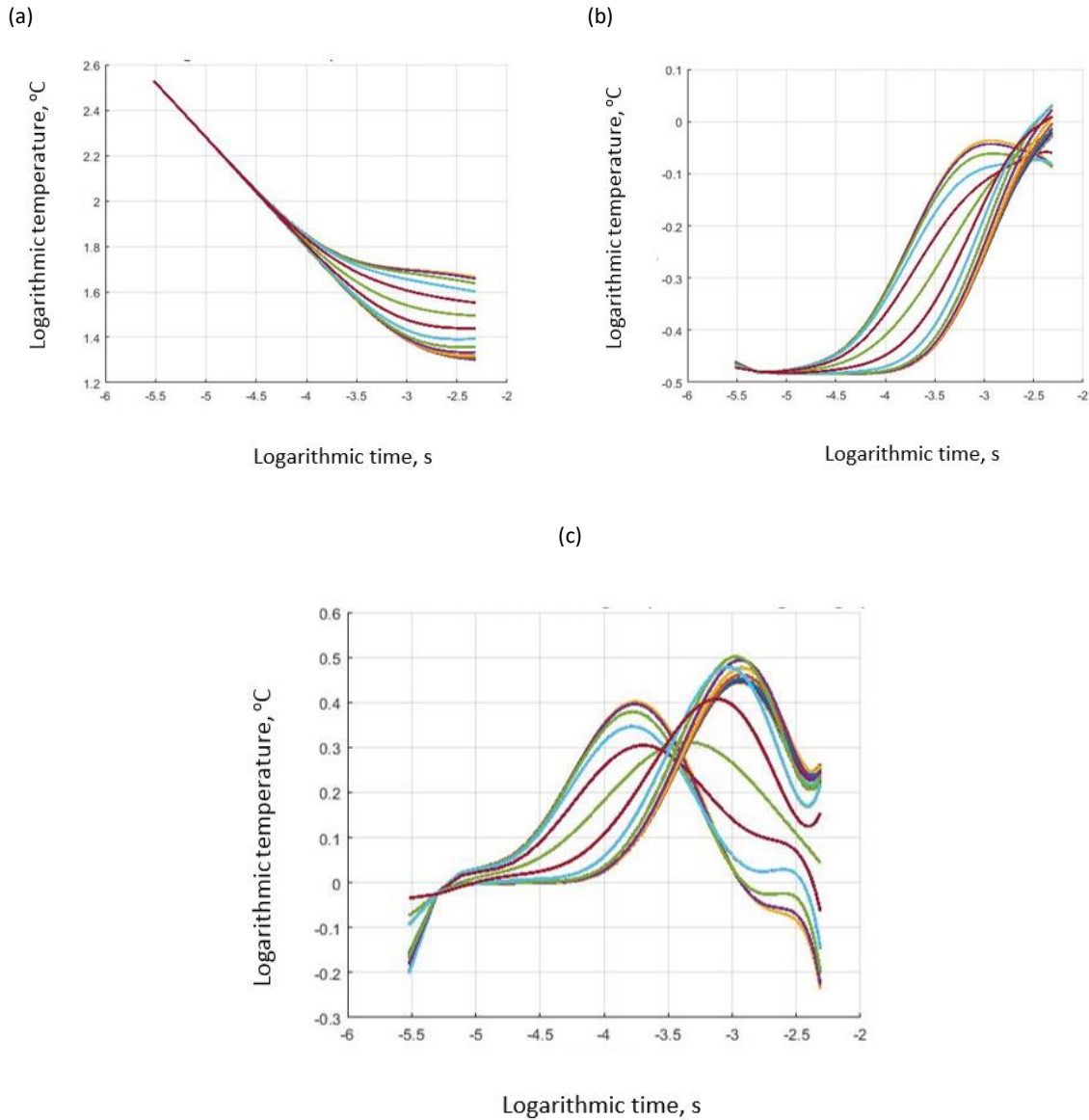


Figure 5.1 (a) Original log temperature-time plot. (b) First order derivative of log temperature-time plot (c) Second order derivative of log temperature-time plot for 5 mm defect size test model.

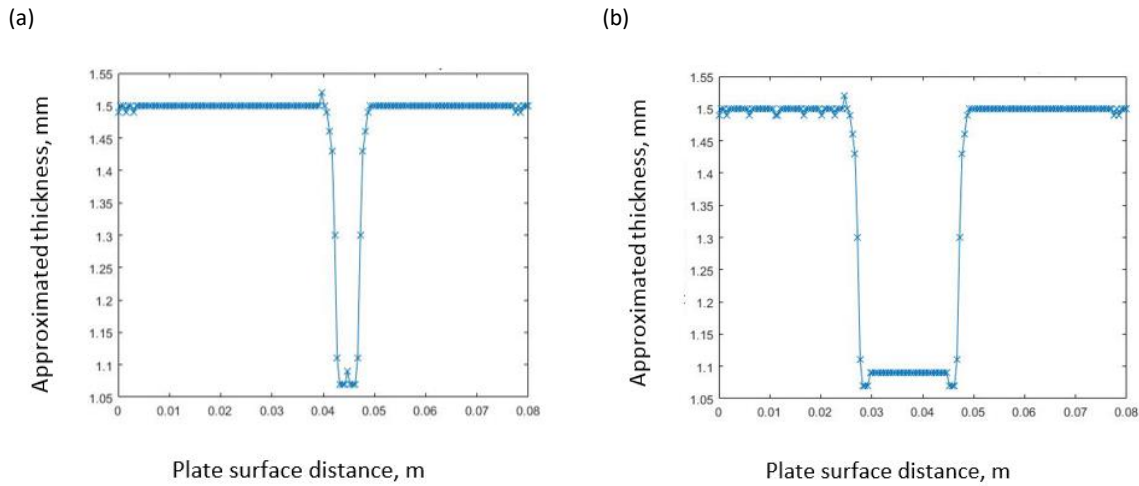


Figure 5.2 Approximated thickness for the plate model with (a) $D_s = 5$ mm and (b) $D_s = 10$ mm for $t_p = 1.5$ mm and $d = 1$ mm.

Balageas [40] suggested the use of an appropriate time domain fitting on the relevant plots to conduct the first and second order derivatives. A large domain size will result in less accurate results; however a small domain size will limit the range of measurable local thicknesses [40]. In this observation set, the time domain was set between 0.005 s to 0.05 s. Since a thin plate was tested, a small time domain can be implemented for high accuracy measurement, while detecting a wide range of local thicknesses.

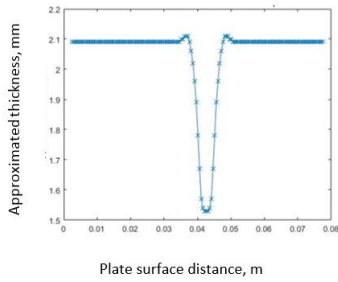
From Figure 5.1a, it is clear that the determination of the point where -0.5 cooling gradient deviates to a plateau temperature was difficult. Meanwhile, it was also challenging to observe this deviation point using the inflection point (i.e. the half rise) of the curve in Figure 5.1b. Nonetheless, the peak logarithmic temperature value as an indication of the -0.5 cooling gradient deviation was achieved with greater ease in Figure 5.1c. It is approximated that the two peaks occurred at a logarithmic time of approximately -3.75 s and -3 s. Using Equation 3.11, the results on the local thicknesses of the model are shown in Figure 5.2.

Figure 5.2 shows that the size of the defect in this setup did not affect the accuracy of defect depth prediction. The analysis to the prediction only accounted for one-dimensional heat flow, which ideally is not affected by the lateral geometry. Meanwhile, the lack in prediction accuracy is due to the effect of the second order peak derivative method. As for the first order derivative of log temperature-time plot (Figure 5.1b), the slope did not register a -0.5 gradient. The effect of convection, in this case, has altered the heat dissipation rate to the surroundings slightly [48].

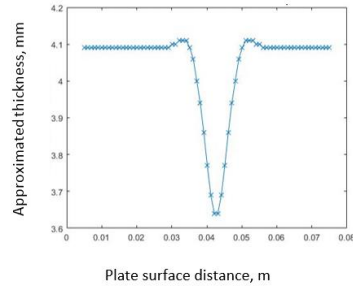
5.1.2 Thick plate test

This next part of the investigation used a thicker plate. Test runs were performed on cases where the defect is positioned at a varying depth in the plate model volume. The same set of constraints for the thin plate test were applied to this instance, except the time domain fittings used to analyse the slope deviation were modified accordingly to the plate thickness used.

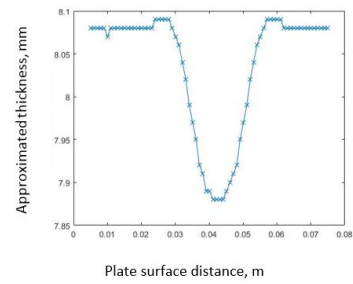
(a.1) $t_p = 2 \text{ mm}$, $d = 1.5 \text{ mm}$



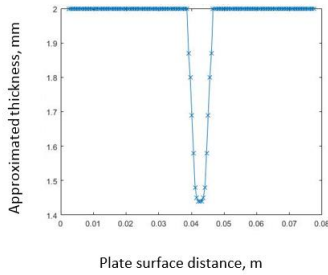
(b.1) $t_p = 4 \text{ mm}$, $d = 3.5 \text{ mm}$



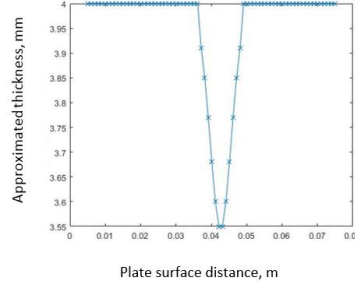
(c.1) $t_p = 8 \text{ mm}$, $d = 7.5 \text{ mm}$



(a.2)



(b.2)



(c.2)

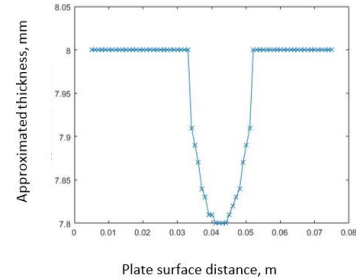


Figure 5.3 Approximated plate thickness measurement for a defect at 1.5 mm, 3.5 mm and 7.5 mm depth (a.1, b.1, c.1). The thickness measurement was then offset to display relative thickness using prior knowledge of sound plate (a.2, b.2, c.2).

Table 5.1 A table summary for the Fourier number time domain and measured material thickness range for respective plate model thickness.

Model thickness, t_p	2 mm	4 mm	8 mm
Defect depth, d	1.5 mm	3.5 mm	7.5 mm
Fourier number time domain	0.014 s - 0.455 s	0.057 s – 1.821 s	0.228 s – 4.0 s
Measured material thickness range (no offset)	1.53 mm – 2.09 mm	3.64 mm – 4.09 mm	7.88 mm – 8.08 mm
Measured material thickness range (with offset)	1.44 mm – 2 mm	3.55 mm – 4 mm	7.8 mm – 8 mm

For the setups shown in Figure 5.3 and Table 5.1, the defect sizes were selected at 5 mm with depth location of 1.5 mm, 3.5 mm and 7.5 mm; respectively. For $d = 7.5$ mm, the maximum observation time was increased to 4 seconds. Theoretically, this is sufficient for thermal energy to diffuse to the base. However, in accordance to the Fourier time domain, it was limited to the detection of 6 mm defect depth. The increase in observation time will improve this detection limit in exchange for a long simulation time and large storage space. Therefore, it was not adopted in this study.

The plots above show a flat surface with a drop in the middle section. The ‘drop’ represents a defect, whereas the remaining material thickness due to defect can be observed from the vertical axis of the plot. There were also small peaks between the transitioning of the flat surface to the drop. It is referred to the model partitioning setup that caused an overlapping effect of heating, thus a local concentration of thermal energy.

Based on the outcomes, it is deduced that as d increases, the defect depth prediction becomes less accurate compared to the actual value. For $d = 1.5$ mm, the error in prediction is 0.03 mm (1.53 mm compared to 1.5 mm) whereas when $d = 3.5$ mm, the error is 0.14 mm (3.64 mm compared to 3.5 mm). The largest error was found when $d = 7.5$ mm, which was 0.38 mm. There are two explanations to this poor accuracy. First, for a deeper defect location, the thermal energy required a longer time to reach the defect. During the diffusion of thermal energy across the material volume, the accumulated heat above the defect will experience lateral diffusion, causing temperature to dissipate and drop more rapidly than early time after heating. As a result, a seemingly alike plateau arrived earlier than anticipated, causing misinterpretation to log temperature-time plots. Furthermore, the time at which

the actual plateau occurs will differ from one-dimensional assumption due to the predominant cooling rate in two-dimensional and three-dimensional [27, 48].

5.1.3 Thick plate test with near surface defect

In this section, the model plate thickness, t_p was increased while positioning the defect nearer to the model surface (small d). The objective of this was to show that the high accuracy prediction in small d is independent of other factors. If d is very small compared to thickness, t_p of the plate model (i.e. 1 mm compared to 8 mm), then the MATLAB script will require modifications. There is a need to use multiple time domains for the analysis of temperature response data. For example, for regions with small thickness, the cooling rate will plateau shortly after heating, prior to attaining a positive value again due to lateral diffusion. The use of a large time domain will neglect the early occurrence of the plateau as it is insignificant. The temperature contrast is relatively small at this point.

Therefore, for an 8 mm thick plate model, an initial time domain range of 0.005 s to 1.45 s was used to determine for any defect depths up to 4 mm. This time domain range will result in an 8 mm thickness measurement for any regions that is undamaged (sound). Finally, the time domain range will change to locate for deeper defects where necessary.

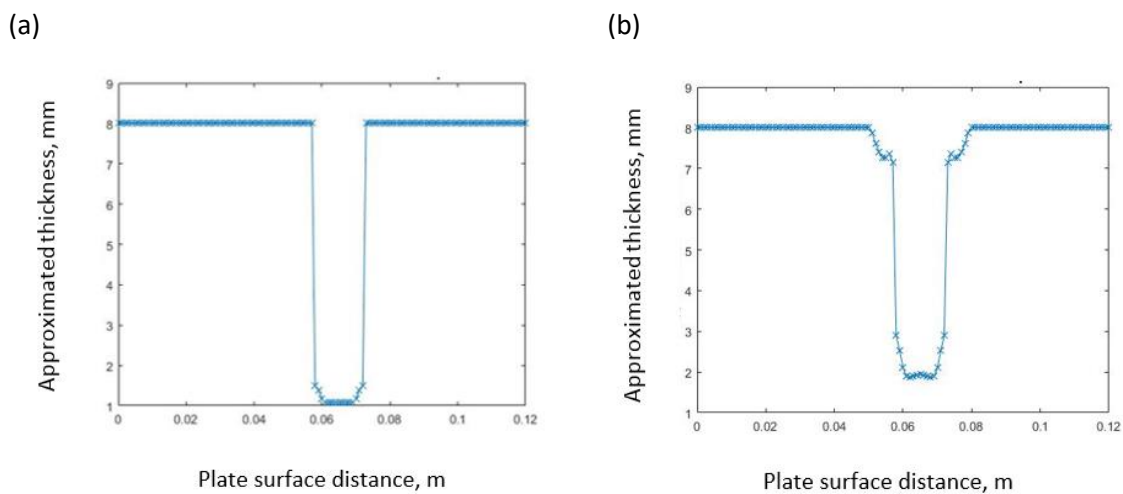


Figure 5.4 Approximated plate thickness for $t_p = 8$ mm with (a) $d = 1$ mm and (b) $d = 2$ mm.

Two tests were conducted for shallow defects and shown in Figure 5.4. The defect depth prediction for the $d = 1$ mm was accurate, whereas when $d = 2$ mm, a small error was observed. It has asserted the inference that the deeper defect location will cause a larger discrepancy in defect location prediction.

5.2 Defect Size Prediction

The other objective of this simulation is to determine the size of underside defects. This is achieved using the FWHM method. The temperature-spatial profile was recorded and the full width at half maximum was measured. The measured width corresponded to the apparent defect size at the time of interest. The series of apparent defect sizes (FWHM measurements) were then plotted over a range of observation time. Finally, the back-extrapolation technique was utilised on the plotted data to gauge the actual defect size.

5.2.1 Thin plate test

The effects of varying underside defect sizes were tested for 3 mm, 5 mm, 8 mm, 10 mm and 20 mm. The fixed parameters were $t_p = 1.5$ mm with $d = 1.0$ mm. The time intervals for the measurement of FWHM values were as suggested in Chapter 4.

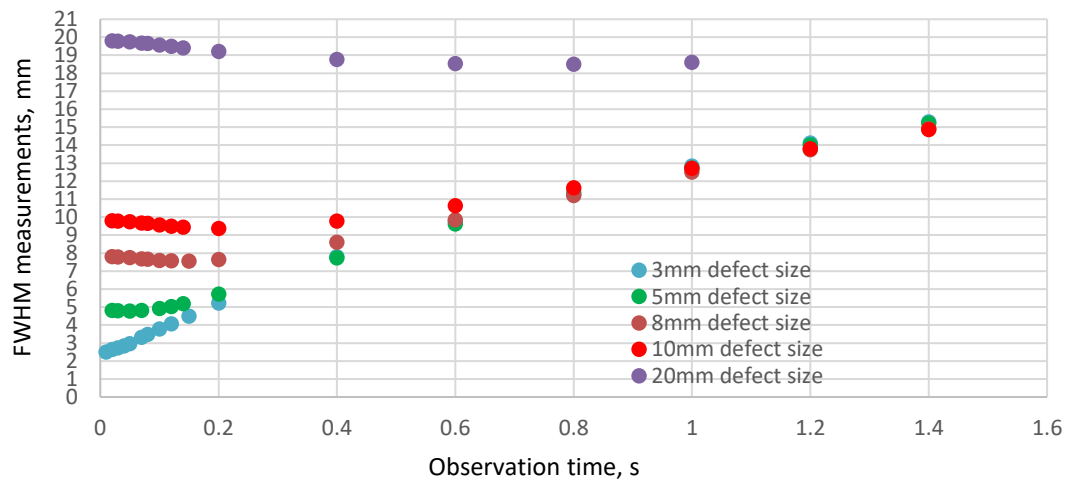


Figure 5.5 FWHM measurements over an observation time of up to 1.4 s for $t_p = 1.5$ mm and $d = 1$ mm.

Table 5.2 Comparison of actual and predicted outcome of defect size

Actual size, D_s (mm)	Predicted size, D_{SE} (mm)	Error (mm)
3	2.34	0.66
5	4.81	0.19
8	7.78	0.22
10	9.8	0.2
20	19.91	0.09

Data points in the region of a decreasing trend were curve fitted with a linear or 3rd order polynomial curve. The coefficient of determination value was used to select the choice of curve fitting. The remaining FWHM measurements were eliminated as it was not useful in defect size prediction. These unwanted data were significantly affected by edge effects, therefore invalid. Using this curve fitted line, the back-extrapolation method was applied by evaluating the y-intercept value to predict the actual underside defect size. There are also unique cases of small defects (i.e. $D_s = 3$ mm and 5 mm) which do not have a clear decreasing trend. For the analysis of such circumstances, all data points on the plot were employed for curve fitting and back-extrapolation. For a short time after heating in the case of shallow defect, thermal waves will coincide with the defect interface and result in wave reflection prior to the significant effects of lateral diffusion and edge effects [47].

From Figure 5.5 and Table 5.2, an evident trend can be observed: as the actual underside defect size, D_s increases, the error in prediction gradually reduces. Previous findings have shown similar evidence [39]. In large defects, the opposite edges of the defect have a greater gap as compared to small defects. When heat diffuses into the material volume, the large gap between the opposite edges delays the overlapping edge effect at the centre plane of the defect. A defect radius has to be larger than the effective thermal diffusion length at any time to postpone the occurrence of edge effects. Consequently, the scenario where FWHM measurement increases was found at later observation time. The advantage of having a large defect is the wider range of valid FWHM measurements. Thus, there is a larger number of data points that fell in the decreasing trend of the FWHM measurement plot. Subsequently, the curve fitting for back-extrapolation could fully describe the thermal diffusion behaviour of the system. This also leads to the better prediction of actual defect size using the one-dimensional assumption.

For D_s of 3 mm and 5 mm, the edges of the defects were in close proximity compared to the D_s at 20 mm. Edge effects have the tendency to occur earlier, in this case, leading to the rapid increase in FWHM measurements. Prediction results from this observation set have an extent of error arising due to the impact of edge effects.

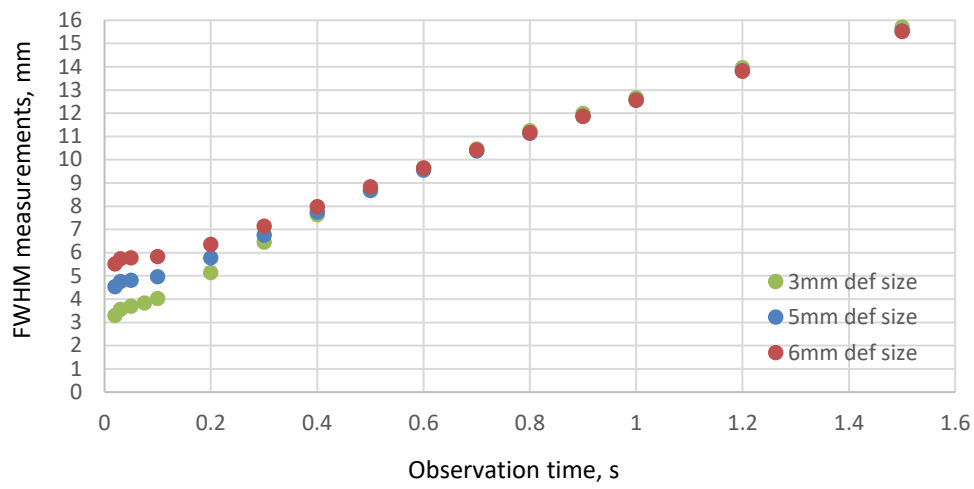
5.2.2 Thick plate test

The next part examines the effect of increasing gap between defect and plate surface, d . The plate thickness, t_p is increased while fixing the material thickness reduction, t_R at 0.5 mm. It is without a doubt that the results deteriorate, identically to earlier tests on defect depth predictions.

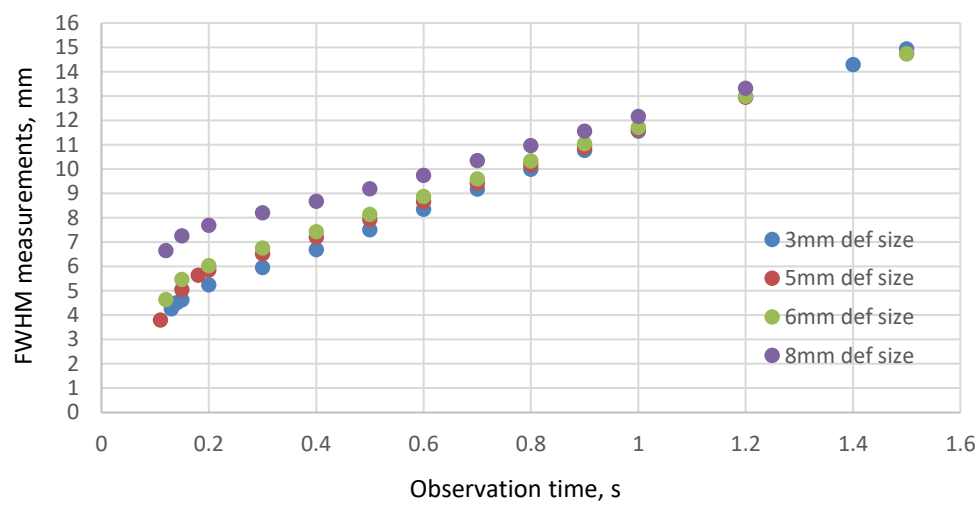
Using the back-extrapolation technique, the first measurable FWHM value was observed at a later observation time as defect depth increased from 1.5 mm to 7.5 mm (Figure 5.6a, b, c, d). This is

correlated to the effective thermal diffusion coefficient. At a defect depth of 1.5 mm, the back-extrapolation technique resulted in good prediction accuracy (Figure 5.6a). Meanwhile, the first recorded FWHM measurement for a defect depth of 7.5 mm was found at approximately 0.7 s after heating (Figure 5.6d). This is due to the large delay in achieving sufficient surface temperature contrast as thermal energy is required to propagate an additional plate thickness before arriving at any substructure discontinuity. At this late observation time, the effective thermal diffusion coefficient for edge effects is achieved. The effect of reverberation which is the spreading of thermal energy becomes significant [47]. It will dissipate most thermal energy on the defective region to its surrounding, leading to a lowered temperature contrast for FWHM measurement. The back-extrapolation of this set of FWHM measurements showed large inaccuracy. With the limited number of FWHM measurements at observation time earlier than 0.7 s, it was difficult to achieve high accuracy defect size prediction for a deep location. Lastly, for an underside defect size of 20 mm at 7.5 mm below the model surface, edge effect was held off for a longer time. However, it did not result in a reasonable defect size prediction (Figure 5.6d).

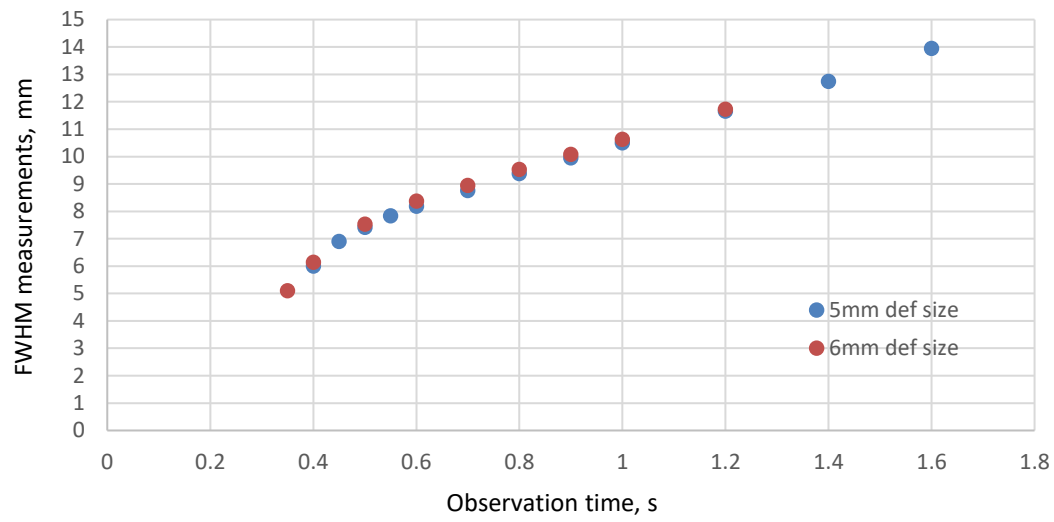
(a)



(b)



(c)



(d)

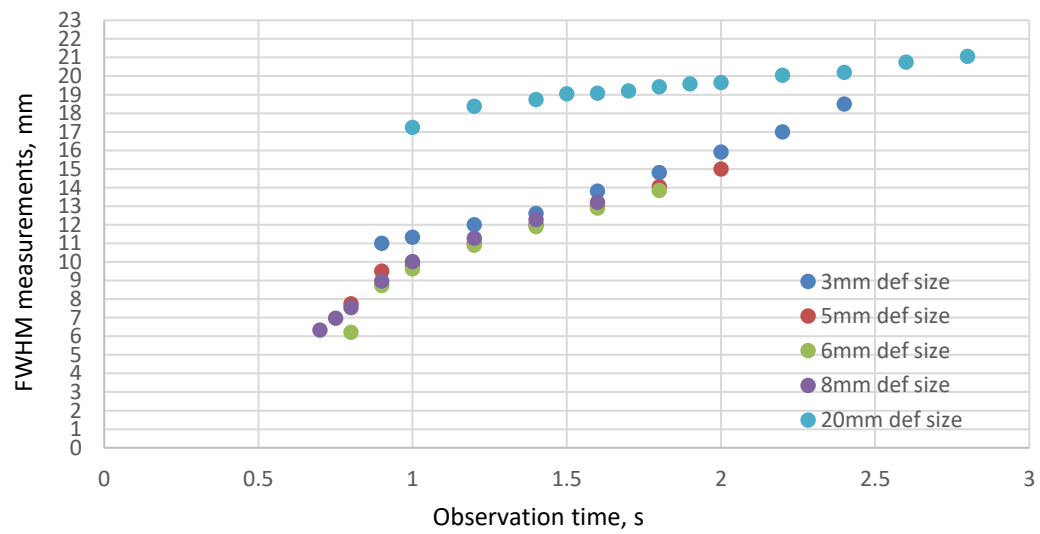


Figure 5.6 Plots for defect depth, d at 1.5 mm, 3.5 mm, 5.5 mm and 7.5 mm (a, b, c, d). In each plot, t_R is kept at 0.5 mm, while plate thickness, t_p is varied to simulate the proposed defect depth. The effect of different defect sizes, D_s was also tested.

5.2.3 Thick plate test ($d = 1$ mm)

Based on an earlier analysis (Section 5.2.1), a shallow defect ($d = 1$ mm) showed a good approximation for defect size prediction except for small defect sizes. When d increased to 7.5 mm in an 8 mm thick plate, the resulting temperature contrasts were small during short observation times. Subsequently, it was not possible to determine a valid FWHM measurement. The underside defect size was not predicted in this case. In this section, the plate thickness was kept at 8 mm to resemble the size of a rail track base closely. The depth of the defect was varied to investigate its limit for high accuracy prediction. A model with $t_p = 8$ mm and $d = 1$ mm was initially tested with varying defect size, D_s of 5 mm, 8 mm, 10 mm and 20 mm as illustrated in Figure 5.7.

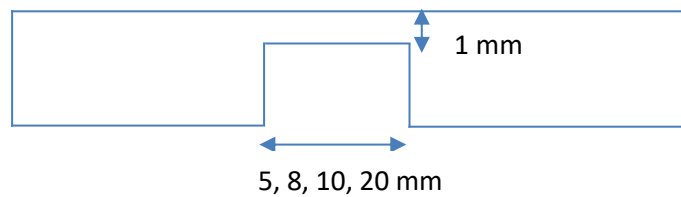


Figure 5.7 One-dimensional illustration of the defect dimension and location.

Temperature contrasts smaller than 0.1 °C were removed from the FWHM analysis as it was insufficient for accurate analysis. Figure 5.8 shows that most range of temperature contrast lies above the threshold of 0.1 °C.

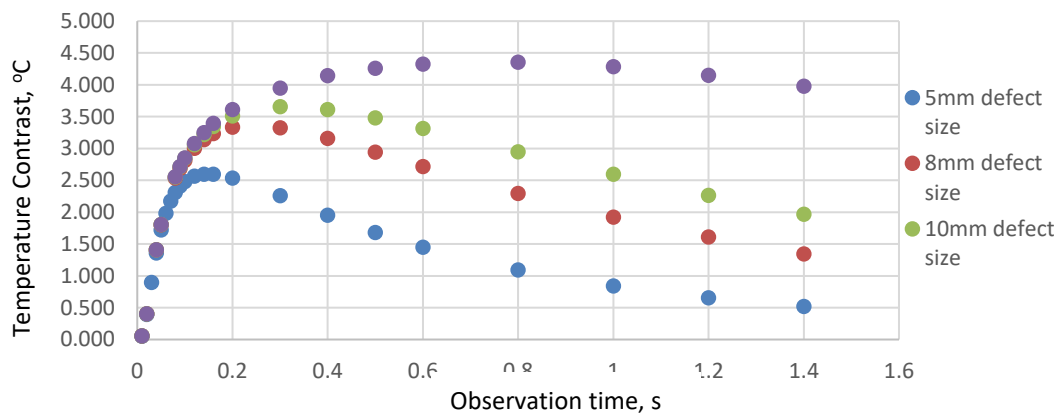


Figure 5.8 Temperature contrast for various defect sizes at $d = 1$ mm in a plate of $t_p = 8$ mm.

In order to predict an underside defect size, the back-extrapolation method was used only for FWHM measurements that had sufficient temperature contrast. A 3rd order polynomial or linear curve was used to best fit the region of FWHM measurements with decreasing trend for instance in Figure 5.10. Most cases as seen in Figure 5.9 follow the general rule of thumb of having an initial diminishing

FWHM measurements trend. The case of small defect sizes behaved otherwise: they experience a gradual increase in FWHM measurements from the start.

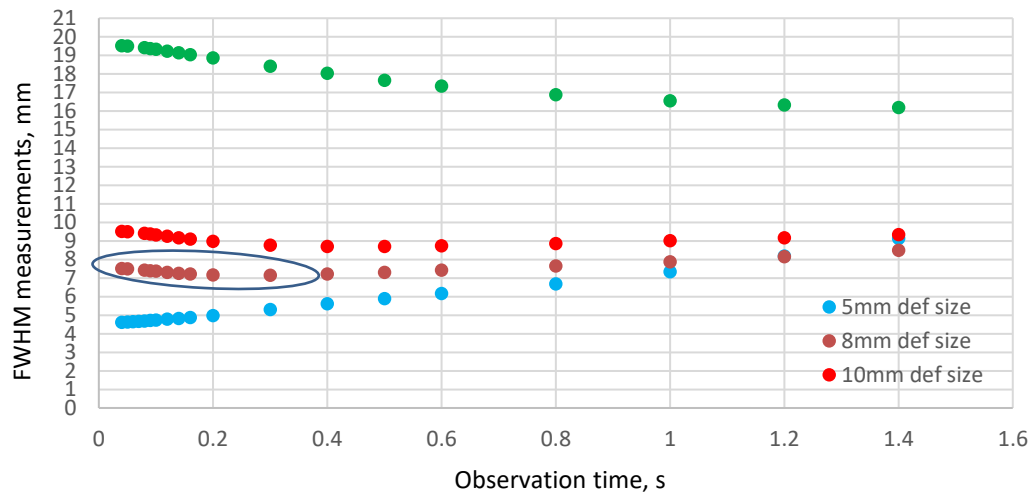


Figure 5.9 FWHM measurement plots up to 1.4 s for $d = 1$ mm and $t_p = 8$ mm, with different defect sizes, D_s .

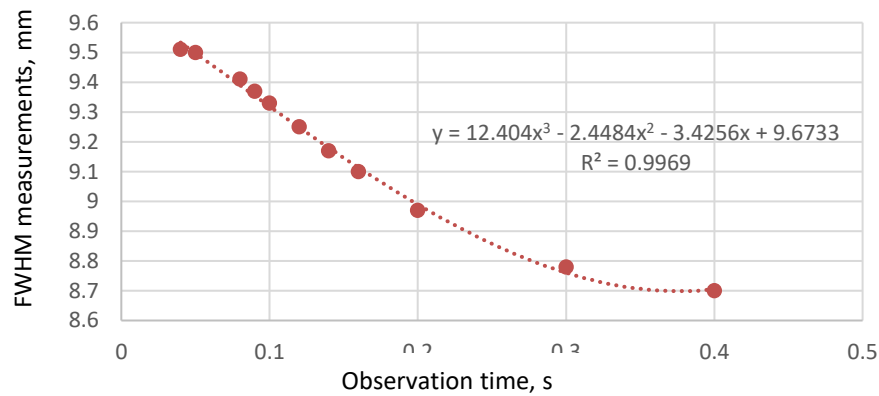


Figure 5.10 Magnified view of the circled region in Figure 5.9 with the polynomial curve fitting technique.

Table 5.3 Summary table for differences between actual and predicted defect sizes.

Actual defect size (D_s)	Predicted defect size (D_{SE})	Prediction differences
5 mm	4.41 mm	0.59 mm
8 mm	7.61 mm	0.39 mm
10 mm	9.67 mm	0.33 mm
20 mm	19.68 mm	0.32 mm

The simulation setup in this section is similar to Section 5.2.1 where a defect depth of 1 mm was used. However, in this section, an 8 mm thick plate was investigated instead. From Table 5.3, it is evident that the larger defect sizes allow for higher defect size prediction accuracy. This is, in fact, an identical trend to the thin plate investigation, where $t_p = 1.5$ mm and defect depth at 1 mm (Section 5.2.1). At $D_s = 20$ mm, the predictions differed by 0.09 mm (refer Table 5.2) compared to 0.32 mm (refer Table 5.3). This is explained by the additional volume in the $t_p = 8$ mm test model that permitted for greater heat dissipation which eventually lowered the overall surface temperature abruptly. As a result, the visible temperature contrast diminished sooner, causing a less accurate FWHM measurement.

To verify this finding, a test was conducted on the model where it is split into an upper and lower deck as illustrated in Figure 5.11. Observations were made by varying the mesh sizes in these regions. The setup of $d = 1$ mm, $t_R = 7$ mm, $D_s = 10$ mm was taken as the experimenting model for 8 mm plate thickness. Initially, fine meshing was introduced to the upper deck while the lower deck mesh remained constant (case 2). Then, the alternative was implemented (case 3). The meshing summary can be found in Table 5.4 and Figure 5.12.

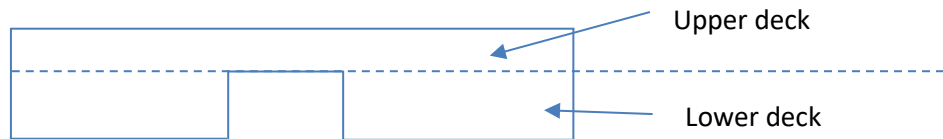


Figure 5.11 One-dimensional view of the plate model for meshing inspection. Dotted lines separate the plate model into two sections: upper and lower deck

Table 5.4 Meshing inspection for upper and lower deck as described in Figure 5.12.

	Lower Deck	Upper Deck
Case 1	1 mm element size	0.5 mm element size
Case 2	1 mm element size	0.25 mm element size
Case 3	0.25 mm element size	0.5 mm element size

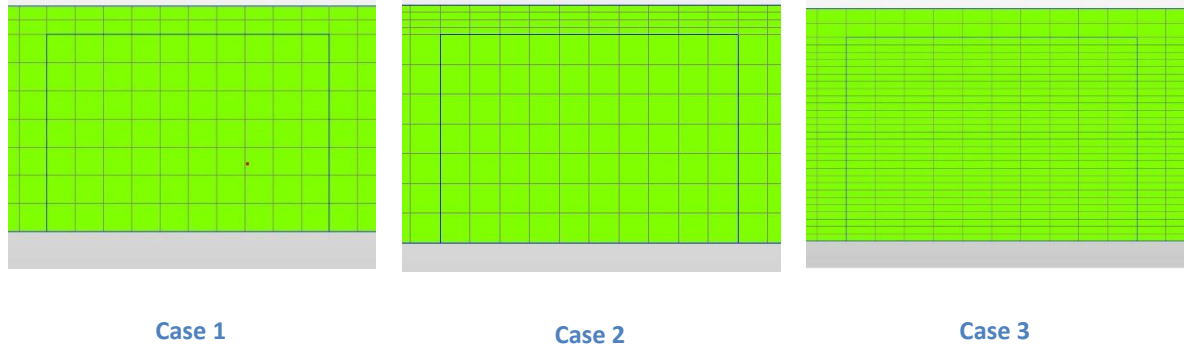


Figure 5.12 Illustration of differences in mesh setup for all 3 cases.

The FWHM measurements for a range of observation time were similar between Case 1 and 2 whereas Case 1 and 3 showed slight differences. In terms of final defect size prediction, Case 1 and 2 share identical results of $D_{SE} = 9.67$ mm (3.3% error from $D_s = 10$ mm) while Case 3 showed an improved accuracy of $D_{SE} = 9.79$ mm (2.1% error). It is concluded that the volume of the upper deck region had no effect on surface temperature responses and FWHM measurements. Oppositely, the volume at the lower deck region affects the prediction outcome. This part of the investigation had subsequently explained the lower prediction accuracy when a thick plate of 8 mm was used. The larger volume at the lower deck affected the temperature response measurements. Meanwhile, the use of finer meshing for improved predictions cost an increase of 3 times the disk space and simulation time. Therefore, it was not implemented in this study. The global mesh size of 1.0 mm suggested in Section 4.2.3 is sufficient to produce a valid and accurate result. In summary, any future work on this area of research should consider this major factor.

5.2.4 Thick plate test ($d = 2$ mm)

In this section, a test model with $d = 2$ mm with $t_R = 6$ mm is used. The defect sizes, D_S tested were 5 mm, 8 mm, 10 mm and 20 mm.

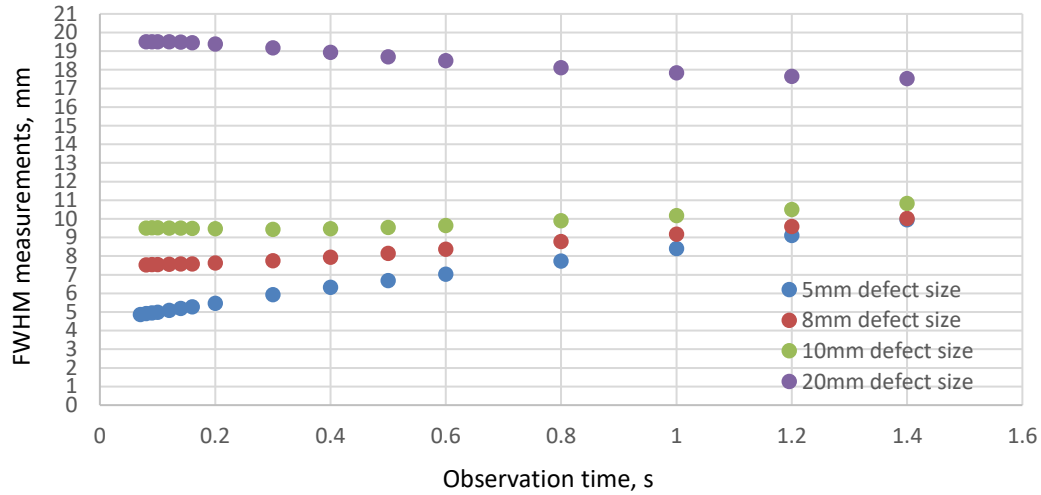


Figure 5.13 FWHM measurement plots for defect at $d = 2$ mm, $t_p = 8$ mm with varying underside defect sizes, D_S .

Table 5.5 Comparison between $d = 1$ mm and 2 mm in a plate model.

	$d = 1$ mm; $t_R = 7$ mm		$d = 2$ mm; $t_R = 6$ mm	
Actual defect size, D_S	Predicted defect size, D_{SE}	Prediction differences	Predicted defect size, D_{SE}	Prediction differences
5 mm	4.41 mm	0.59 mm	4.67 mm	0.33 mm
8 mm	7.61 mm	0.39 mm	7.46 mm	0.54 mm
10 mm	9.67 mm	0.33 mm	9.62 mm	0.38 mm
20 mm	19.68 mm	0.32 mm	19.69 mm	0.31 mm

According to Figure 5.13, it is apparent that the 2 mm defect depth plots consist of initial FWHM measurements at a later observation time compared to the 1 mm defect depth. For instance, in the $d = 2$ mm case, the first measurable FWHM value was found at a later observation time. This is a result of the additional 1 mm gap between the plate surface and defect. Since heat diffusion will take a longer time to reach the defect, thus, an observable temperature contrast commenced later. The

downside of this phenomenon is the limited results on early FWHM measurements, which further leads to the low accuracy in back-extrapolation for defect size prediction. Even then, the prediction error was small and acceptable.

According to Table 5.5, for $D_s = 5$ mm, the defect size prediction accuracy was similar to the case of $D_s = 20$ mm. This is an unusual phenomenon to the established trend of small defect size should yield larger prediction discrepancy. For a small defect size such as 5 mm, the occurrence of early edge effect is anticipated prior to an observable temperature contrast. This resulted in an increasing trend of FWHM measurements from the start. To analyse this set of results, the back-extrapolation technique was used on all available FWHM measurements. As a result, the final defect size prediction was fairly accurate. Nonetheless, this is not comparable to the tests on other defect sizes. This is due to the differences in back-extrapolation technique where other cases analyse the region with decreasing trend only.

5.2.5 Thick plate (large t_p) with $d = 4$ mm, 6 mm

As defect depth, d further increases to 4 mm and 6 mm, it is observed in Figure 5.14 that the initial FWHM measurement occurred at a later observation time. This delay causes larger uncertainty to the back-extrapolation results. Using all available FWHM measurements, both test cases were analysed as per usual with the curve fitting and back-extrapolation method. Results in Tale 5.7 show that the defect size prediction is highly inaccurate.

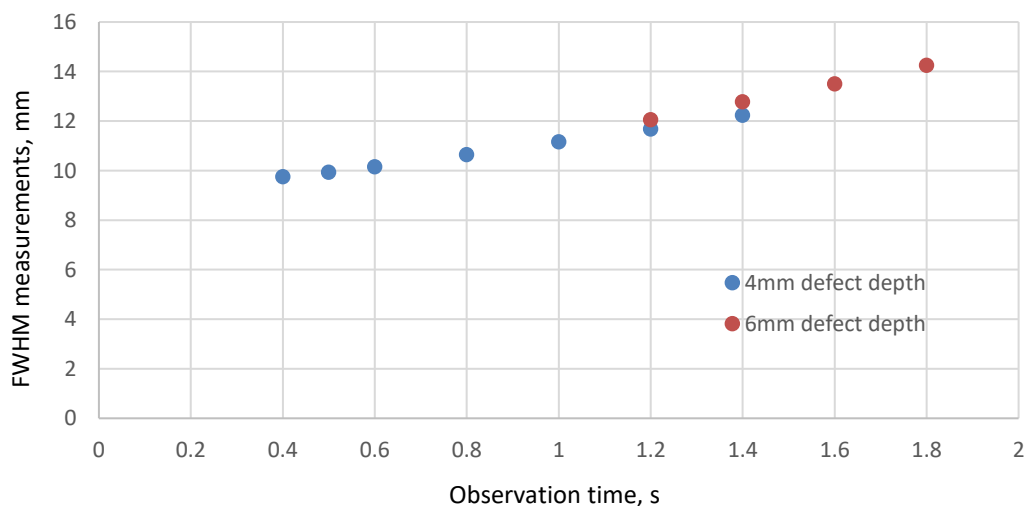


Figure 5.14 Comparison of FWHM measurements for $d = 4$ mm and $d = 6$ mm with $D_s = 10$ mm in an 8 mm thick plate.

Table 5.6 Defect size prediction for $d = 4$ mm and $d = 6$ mm with $D_s = 10$ mm in an 8 mm thick plate.

$t_p = 8$ mm	$d = 6$ mm; $t_R = 2$ mm			$d = 4$ mm; $t_R = 4$ mm		
Actual defect size, D_s	Predicted defect size, D_{SE}	Prediction differences	Temp. contrast at 1.2 s	Predicted defect size, D_{SE}	Prediction differences	Temp. contrast at 1.2 s
10 mm	5.16 mm	4.84 mm	0.099 °C	9.13 mm	0.87 mm	0.388 °C

It is evident in Table 5.6 that for $d = 6$ mm, the estimation error was the largest. The temperature contrast measured at an observation time of 1.2 s for this test was as low as 0.099°C, just sufficient for a valid FWHM measurement. Even then, the inaccurate prediction is likely to be contributed by the lack of early information on FWHM measurements. Meanwhile, for the $d = 4$ mm test, the calculated prediction error of approximately 10% was merely acceptable. For these deep defects, the spreading of thermal energy across the test model volume is significant. The effective thermal diffusion coefficient for edge effect to occur has been achieved prior to the first FWHM measurement. In conclusion, the increasing gap between an observing surface and underside defect will increase the error in defect size predictions.

5.2.6 Proposed modifications for prediction improvement

The prediction of a 6 mm defect depth or larger can potentially be improved by supplying heat at a slightly longer duration. Firstly, this will significantly increase the magnitude of temperature contrast measured, leading to a more accurate FWHM measurement. Secondly, according to the FWHM theory, measurements are taken after the heat source is removed, to observe a temperature contrast. The larger delay in FWHM measurement recording allows for the closer approximation of back-extrapolation. As a result, the uncertainty of back-extrapolation can be minimised. Table 5.7, Figure 5.15 and Figure 5.16 describe the differences when heating is applied for 0.02 s and 0.4 s.

The overall increase in thermal energy provided a larger temperature contrast for results observation. There is, however, a concern for material destruction due to high thermal loading and the introduction of excessive noise [21]. Alternatively, the heating energy can be lowered only if the heating period is sufficiently long for significant temperature contrast and valid FWHM measurement. In addition, the extended heating period may cause surface reflection issues during the heating phase, resulting in the similar disadvantage as a lock-in thermography and step-heating thermography.

Table 5.7 Differences in FWHM measurement at respective observation time when heating period is increased.

0.002 s heating period		0.4 s heating period	
Observation time (s)	FWHM	Observation time (s)	FWHM
0.5	9.09 mm	-	-
0.6	9.8 mm	0.2	8.53 mm
0.8	10.68 mm	0.4	9.99 mm
1.0	11.38 mm	0.6	10.79 mm
1.2	12.06 mm	0.8	11.45 mm
1.4	12.78 mm	1.0	12.13 mm
1.6	13.5 mm	1.2	12.85 mm
1.8	14.25 mm	1.4	13.58 mm

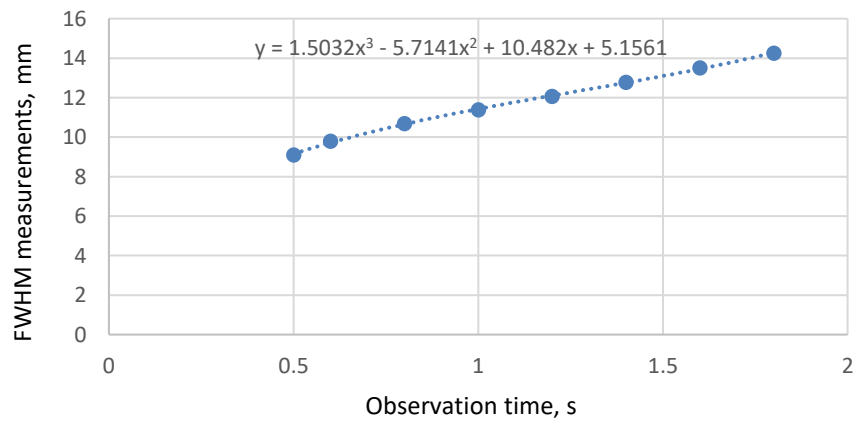


Figure 5.15 FWHM measurements for 0.002 s heating period (short heating). $t_p = 8$ mm, $d = 6$ mm, $t_R = 2$ mm and $D_S = 10$ mm.

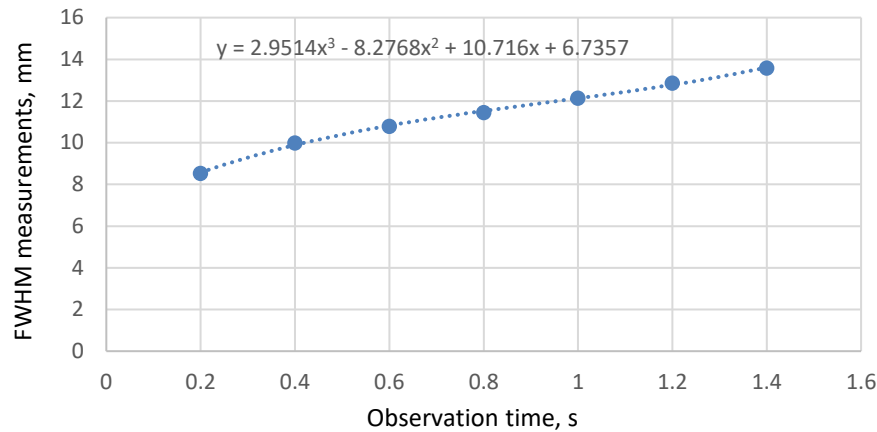


Figure 5.16 FWHM measurements for 0.4 s heating period (long heating). $t_p = 8$ mm, $d = 6$ mm, $t_R = 2$ mm and $D_S = 10$ mm.

Table 5.8 Comparison results of defect size prediction, D_{SE} for 2 ms and 0.4 s heating. Coefficients of determination value of curve fitting are provided in brackets.

Curve fitting	2 ms heating (r value)	0.4 s heating (r value)
Linear fit	7.45 mm (0.9943)	8.16 mm (0.9812)
2nd order polynomial	6.88 mm (0.9968)	7.59 mm (0.9919)
3rd order polynomial	5.61 mm (0.991)	6.74 mm (0.9986)

The effect of increasing the heating period to 0.4 s can be observed by locating the initial FWHM value. For the longer heating period, the first FWHM measurement was discovered at approximately 0.2 s after heat was removed. Oppositely, the shorter heating period had an initial FWHM value measured at 0.5 s after heating. The various curve fitting method in Table 5.8 has also shown that the longer heating period managed to predict a defect size of $D_{SE} = 6.74$ mm, which is closer to the actual size of 10 mm. However, this value is not a justified as the prediction was made based on a trend that is impacted by edge effects.

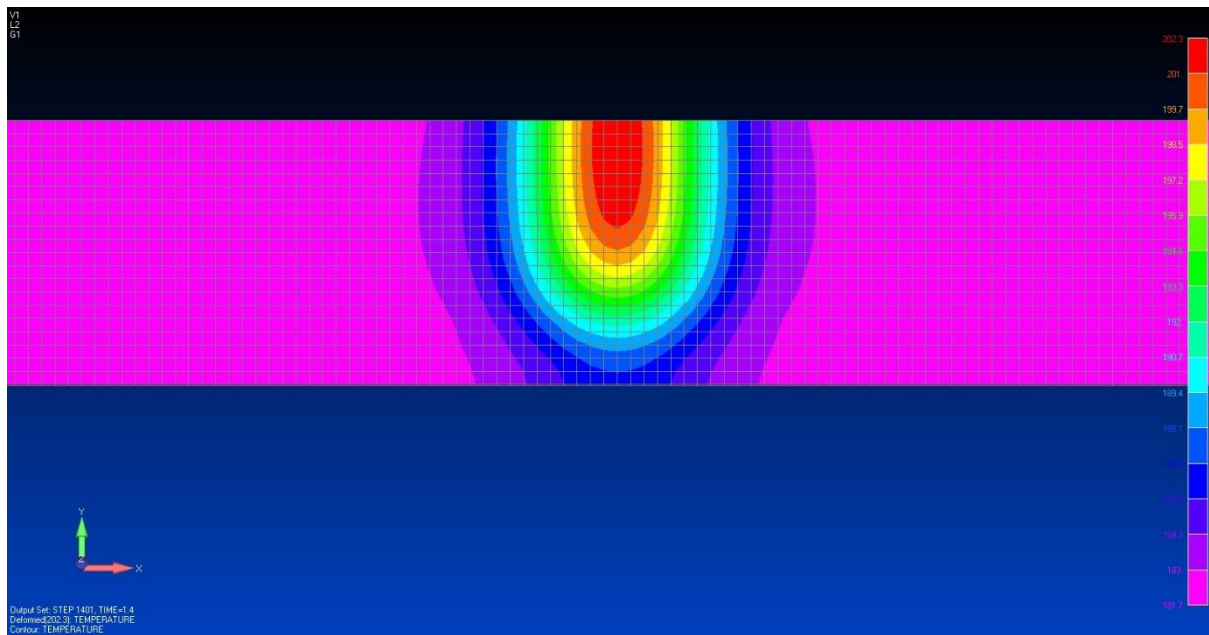


Figure 5.17 Resultant temperature response after 1.0 s of long heating (0.4 s) applied. Image extracted from FEMAP. The maximum contrast between the defective and sound area is 20.6 °C. $t_p = 8$ mm, $d = 6$ mm, $t_R = 2$ mm and $D_S = 10$ mm.

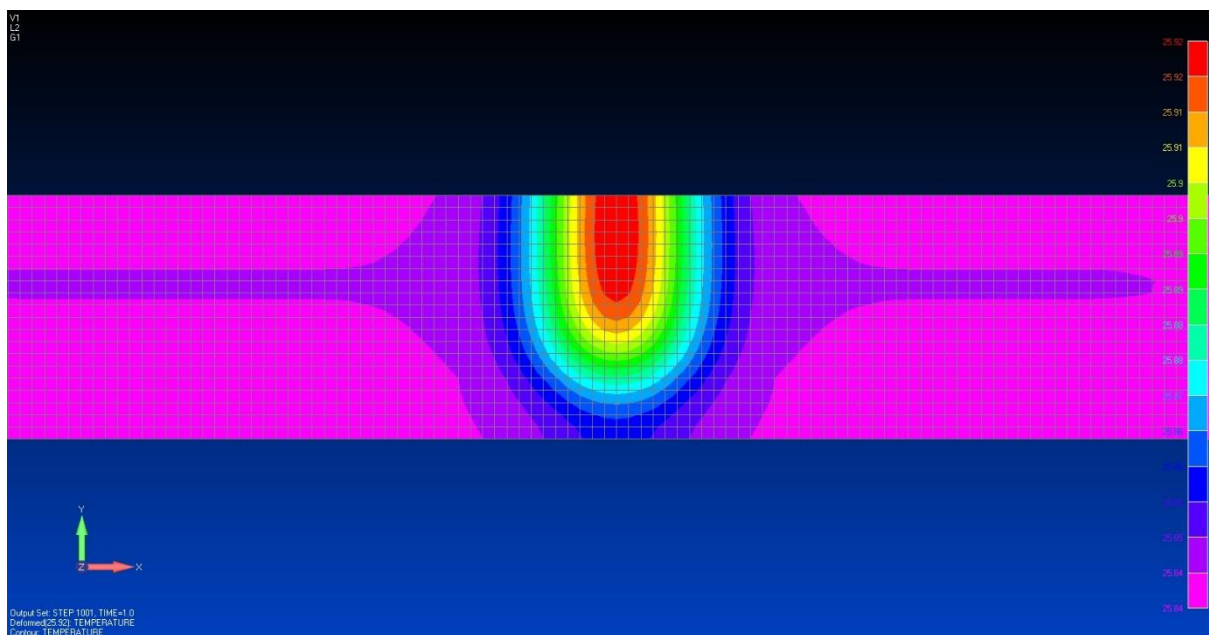


Figure 5.18 Resultant temperature response after 1.0 s of short heating (0.002 s) applied. Image extracted from FEMAP. The maximum contrast between defective and sound area is 0.08 °C. $t_p = 8$ mm, $d = 6$ mm, $t_R = 2$ mm and $D_S = 10$ mm.

The presence of a defect was displayed via the temperature contour contrast regardless of the choice of the heating period used in this study. The only criterion that differentiated the observations is the extent of temperature contrast. The short heating (Figure 5.18) has a smaller temperature contrast compared to the longer heating (Figure 5.17). A small temperature contrast is a limiting factor for most available temperature measuring equipment.

5.3 Chapter Conclusion

The results on stationary heat source showed the limiting defect depth and size that can be measured using the proposed methodologies and setup. This is an important stage in developing a relationship between the stationary and moving heat source tests. In the next chapter, this relationship will be useful for the analysis of moving heat source results.

In this chapter, to begin with, the depth of the defect in a material volume was evaluated. This was accomplished using the second order peak derivative method. The method uses the logarithmic temperature-time profile of each node across a drawn line profile on the model surface, to map out the overall model surface thickness. A defect is detected if any abnormality is present in the measured surface. The test on a thin plate, $t_p = 1.5$ mm and defect at depth 1 mm show that the underside defect size did not affect the accuracy of defect depth prediction. For example, a defect size of 5 mm and 10 mm at the same depth resulted in similar defect depth prediction accuracy. A larger plate thickness was then tested to observe the effect of defect depth and its prediction ability while assuming the independent variable of underside defect size. At $d = 7.5$ mm, the predicted defect depth was approximately 0.38 mm in contrast to the actual value (5.1% error). This is explained by the dominance of lateral heat diffusion at late observation time, high order polynomial curve fitting and the choice of time domain fitting used. In this section, it is concluded that the smaller the gap between the observation surface and defect interface is, the better the depth prediction ability.

The next major focus of this chapter was the prediction of materials underside defect size, D_{SE} . For this analysis, the Full-Width Half Maximum (FWHM) method was used. If a defect is present, the temperature spatial profile will yield a peak. The width of the peak at half-maximum is referred to the apparent defect size. A series of FWHM measurements (apparent defect size) were then used to predict the actual defect size by performing back-extrapolation. Using a thin plate model of $t_p = 1.5$ mm with defect located at $d = 1$ mm, varying defect sizes, D_s were tested. Results confirmed that the largest defect size allowed for the highest accuracy in prediction. However, as defects were located at a deeper location, the accuracy of size prediction began to deviate significantly. For a defect depth of 6 mm, the defect size prediction from the back-extrapolation of FWHM measurements yielded an error of about 50%. This part of the results has also shown the vulnerability of prediction accuracy due to the increase in defect depth location.

Next, the defect was relocated nearer to the surface of the thick plate (small D_s , large t_R). It resulted in a similar trend as the thin plate test. However, it was found that the overall plate thickness had a significant impact on the final defect size prediction. A mesh test was conducted to find that the 'lower deck' of the plate improved prediction accuracy when a finer mesh was implemented. The

investigation of the thesis main objective will be conducted in Chapter 6 using the close approximation to stationary heating. The size and depth location of the defect at the underside of material was predicted using the moving heat source with the knowledge established in this chapter.

6. Moving Heat Source

The tests with stationary heat source in the previous chapter was used to develop and analyse results outcome for a moving heat source test in this chapter. The limitations and methodologies in the stationary heat source test were assumed to be similar to moving heat source test. This assumption helps in simplifying the complexity of moving heating. To set up, a model surface was subdivided into equal segments where heat was applied sequentially. This is unlike stationary heating setup where simultaneous heating on the model surface was conducted. The thesis aim is achieved using computational simulation setup. An underside defect size and its depth in a model are determined by allowing the motion of a heating device across the test model.

The moving heat source uses a time delay between heating segments to produce a motion-like temperature response. To measure the underside defects, similar approaches to stationary heating analysis were adopted. The full width at half maximum (FWHM) of a temperature-spatial profile was used to measure apparent defect sizes over a range of observation time. Then, this series of measurements were used to back-extrapolate for the estimation of actual defect size. Meanwhile, the second order peak derivative of the logarithmic temperature-time plot was used to predict the local thicknesses across the model surface. Using the measured peak time and relevant equation, the local thickness of a point can be evaluated. Both methods were previously implemented for the study on stationary heating. However, it is important to account for the effect of heating delay between each segment in a moving heat source test. The approach to each analysis will require minor modifications.

The structure layout for this chapter is similar to Chapter 5. The prediction of defect depth in a thin plate was first analysed. It is important to understand that since the heat was applied in motion, therefore some regions will experience a delay in temperature rise. Figure 6.1 is an illustration of the moving heat source test.

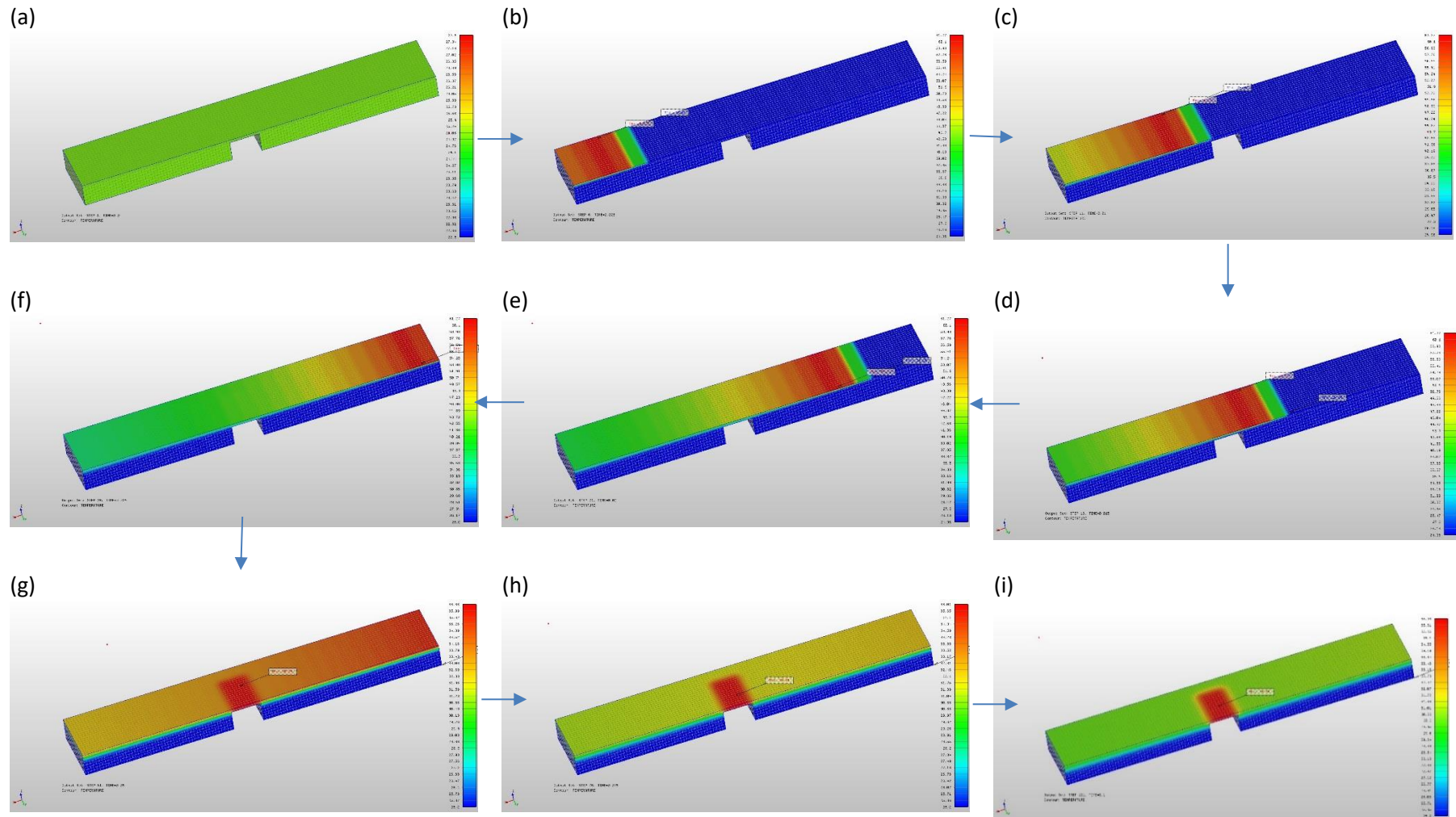


Figure 6.1 The image sequence shows how a moving heat source test develops. (a) The stage where heat has not been applied yet and the test plate is in ambient condition. (b) The heat source initiates from the left end of the plate. (c) – (f) Heat source gradually moves from left to right. (g) - (i) Development of the 'hot region', indicating the presence of an underside defect.

6.1 Defect Depth Prediction

To predict the depth of a defect, the second order peak derivative method was used. The procedure to this is identical to stationary heating. First, the temperature-time profile of each node across the drawn line profile is recorded. Then, the time at which the peak occurs in the second order derivative log temperature-time plot is used to calculate the material local thickness. It is anticipated that each nodal response will experience heating at a different observation time.

6.1.1 Thin plate test

Two plates with 1.5 mm thickness were investigated. Both plates have a defect located at $d = 1$ mm with defect size at $D_s = 5$ mm and $D_s = 10$ mm respectively. The heat was applied for 2 ms per segment, with 1 ms heating delay between segments. The resulting temperature-time profile for the moving heat source test was slightly different from the stationary heating test. This is observed in Figure 6.2. For this test setup, the calculated heating speed is 18 km/hr. The details in achieving this value are outlined in Appendix A.

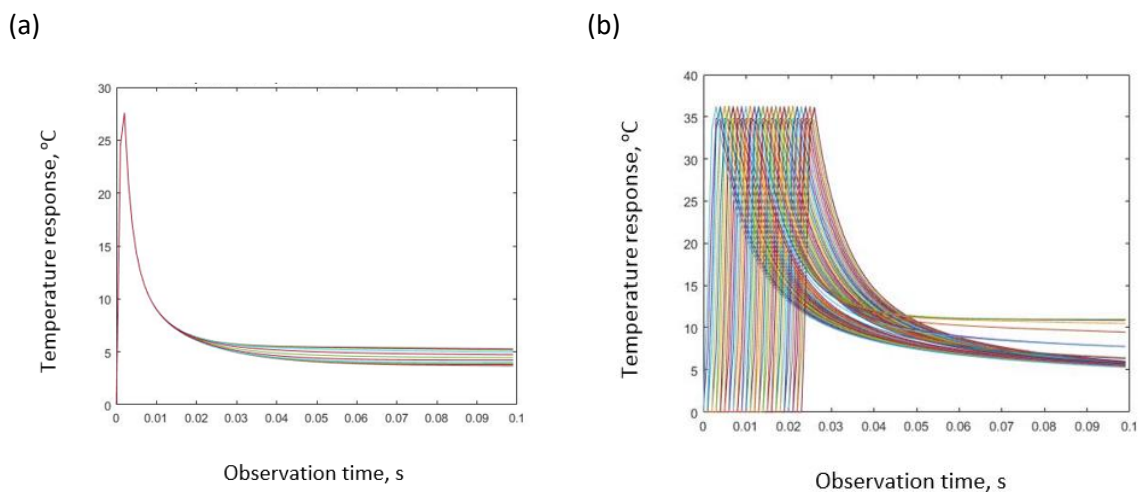


Figure 6.2 Temperature-time profile of each node for (a) stationary heating and (b) moving heat source.

The clear difference between both plots in Figure 6.2 is the presence of multiple peaks in the moving heat source test and a single peak in the stationary heating test. The reason to this is the effect of heating time delay on each node, resulting in the achievement of respective maximum temperature at different observation time. When using the second order derivative method, the peak time, t^* is measured after heat is removed. Coincidentally, this methodology is derived such that analysis is performed after a maximum surface temperature is achieved, which often occurs just after heat is removed.

The measured local thickness for the 5 mm and 10 mm defect size test plate is shown in Figure 6.3. The time domain fitting used for each analysis was referred to Chapter 5. This ensures a consistent comparison between the moving heat source and stationary heating results.

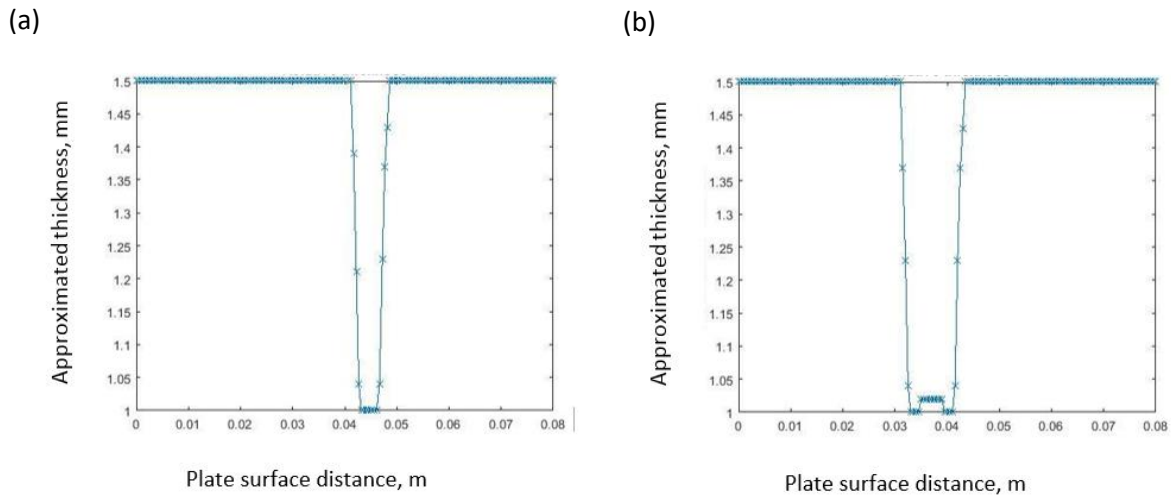


Figure 6.3 Approximated plate thickness for $t_p = 1.5$ mm with (a) $D_s = 5$ mm and (b) $D_s = 10$ mm, both with $d = 1$ mm.

Based on Figure 6.3, both plots were similar where the resulting plate thickness at the non-defective region was about $t_p = 1.5$ mm. The measured defect depth was approximately 1 mm. This set of prediction results matches the actual model geometry. In addition, this finding is closely matching to the stationary heating in Section 5.1.1. An initial inference suggests that the lateral motion of heat source was sufficiently fast that lateral heat diffusion is insignificant. Therefore, it results in proximity as a stationary heating effect. Furthermore, an analysis was conducted in the transient cooling phase where heating procedure is not involved.

Apart from the differences in defect sizes, there were no observable discrepancies in terms of defect depth measurements. In Figure 6.3b, a small fraction of unevenness can be observed at the defective region. This is likely due to the local concentration of thermal energy at the onset of edge effects. This is however not the case for the $D_s = 5$ mm as the edge effects may have fully developed, causing an equal spread of thermal energy across the top surface of the defective region.

6.1.2 Thick plate test

A plate with an overall thickness of $t_p = 8$ mm was modelled for this part of the test. The defect was set up for two cases: one with $d = 1$ mm and another with $d = 2$ mm. The speed of the moving heat source was kept at 18 km/hr.

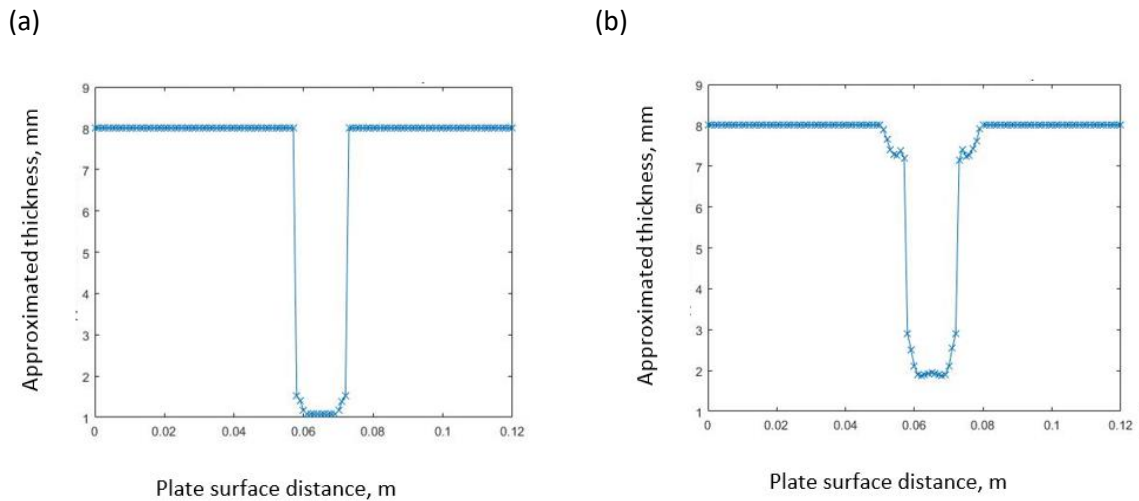


Figure 6.4 Heating speed of 18 km/hr for a $t_p = 8$ mm model with (a) $d = 1$ mm and (b) $d = 2$ mm. Both cases have $D_s = 5$ mm.

The results show that the prediction of defect depth and the material local thickness is accurate. It is able to clearly map out the overall plate thickness of $t_p = 8$ mm with the defect at $d = 1$ mm in Figure 6.4a and $d = 2$ mm in Figure 6.4b. As predicted, due to the large differences in local thicknesses, the analysis procedure required the constant adjustment of the time domain fitting frame to locate the potential defects at various depths. From Figure 6.4b, it is also apparent that the approximated thickness was inconsistent in some region. Despite a reasonable prediction measurement, it fell short of accuracy when compared to the case of $d = 1$ mm. This is mainly due to the effect of having a deeper defect. As shown previously in the stationary heating investigations, a deeper defect causes a higher error in defect depth prediction. Therefore, based on this matching relationship, the test for deeper defect in moving heat source is anticipated to result in similarly low accuracy as stationary heating. In summary, proximity of defect and model surface will result in a good accuracy of defect depth prediction for a moving heat source test.

6.2 Defect Size Prediction

The prediction and measurement of defect sizes in this section utilises the FWHM method. First, the temperature spatial profile of a line of nodes is tabulated. If a defect is present, a peak can be observed at the profile. Then, the full width at half maximum of the profile is recorded at a time of interest. This is repeated for a series of observation time and plotted in FWHM measurements versus observation time graph. The back-extrapolation of this series is used to predict the actual defect size. Compared to the technique used in Chapter 5, the difference is the inclusion of heating time delay. This must be removed during analysis to produce a comprehensible result.

6.2.1 Thin plate test

The effect of heating time delay is significant to the results, therefore requires necessary modifications to the raw data collected. The temperature data collected has to account and remove for the delay taken during heating. In this setup, a 1.5 mm plate thickness (Figure 6.5) with defect located at $d = 1$ mm was modelled in two cases with defect sizes of $D_s = 5$ mm and $D_s = 10$ mm. The setup consists of $l_s = 5$ mm segment sizes, heating duration of 2 ms per segment and successive segments heating delay of 1 ms. It simulated a moving heat source speed of 18 km/hr. The accuracy of defect size prediction was promising and similar to the stationary heating.

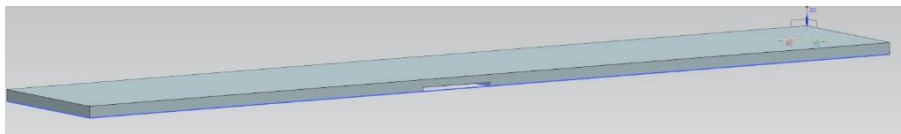


Figure 6.5 Overview of a thin plate with defect at $d = 1$ mm.

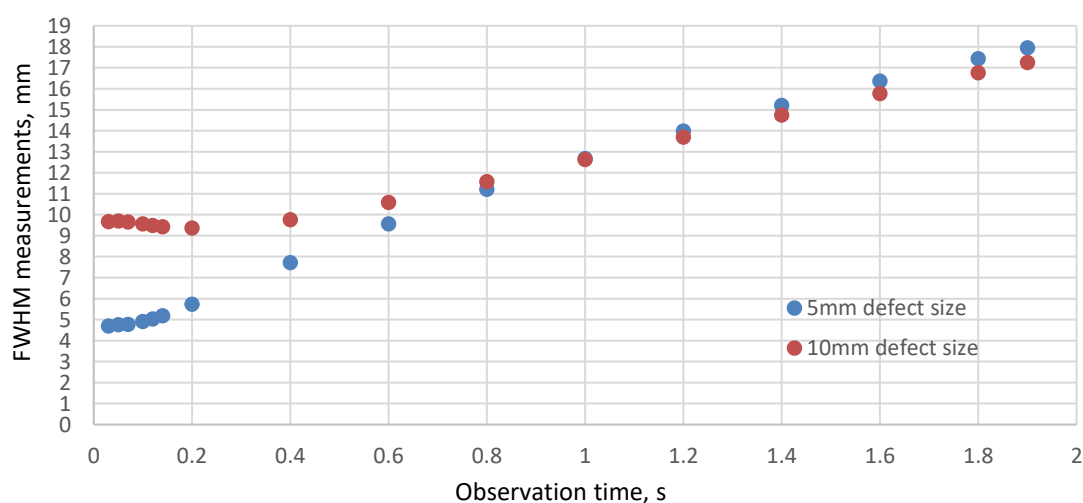


Figure 6.6 FWHM measurements for plate with $t_p = 1.5$ mm, tested with $D_s = 5$ mm and $D_s = 10$ mm at $d = 1$ mm using moving heat source.

In Figure 6.6, the $D_s = 5$ mm test show similarity in trends to the stationary heating test. None of the sets of results presented any FWHM measurement region with a descending trend. Therefore, to analyse this result, all data points on the plot was used to estimate the actual defect size, D_{SE} . Meanwhile, for the $D_s = 10$ mm setup, a 3rd order polynomial curve fitting was used to describe the region of a descending trend. The back-extrapolation technique resulted in the following outcome in Table 6.1.

Table 6.1 Results of moving heat source test for thin plates with defect at $d = 1$ mm.

Actual defect size, D_s	Predicted defect size, D_{SE}	Differences
5 mm	4.66 mm	0.34 mm
10 mm	9.71 mm	0.29 mm

The results show that for a larger defect size, the prediction results gained accuracy. It had the same trend as the stationary heating results. Edge effect commenced at a later observation time for the $D_s = 10$ mm setup, thus allowing a larger range of decreasing trend to be curve fitted for back-extrapolation.

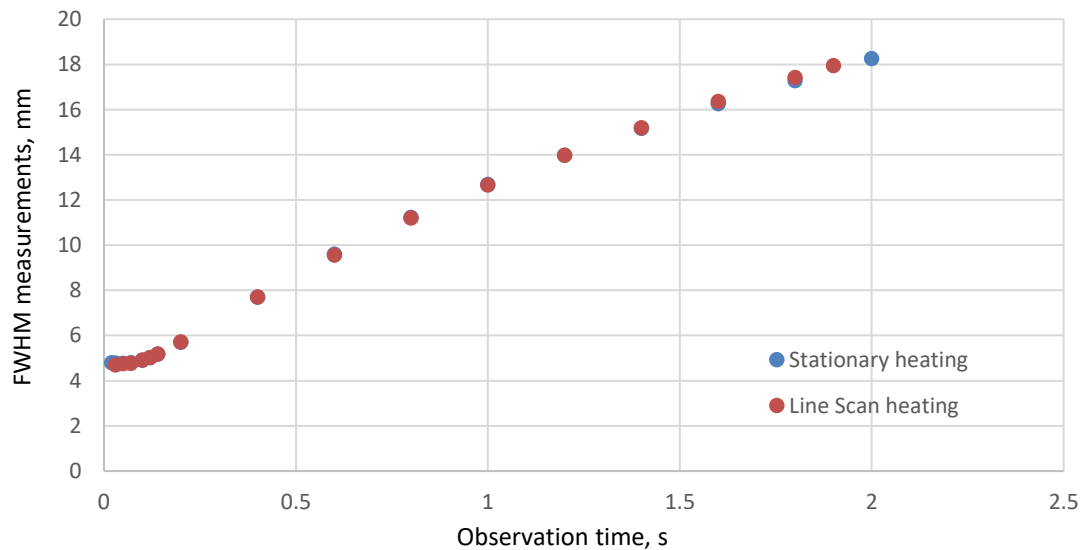


Figure 6.7 FWHM measurements comparison for stationary and moving heat source test. $t_p = 1.5$ mm, $d = 1$ mm, $D_s = 5$ mm.

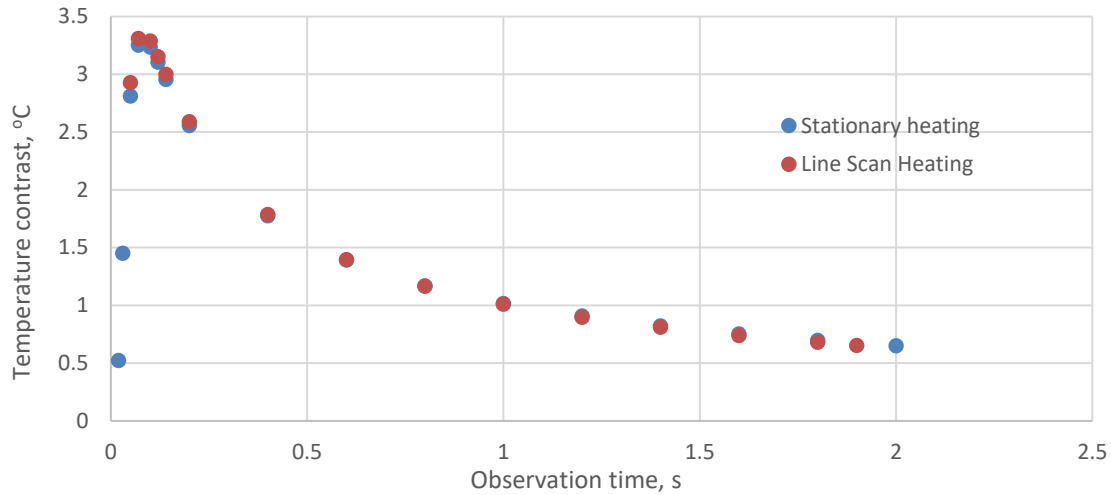


Figure 6.8 Comparison of temperature contrast profile in stationary and moving heat source test for $t_p = 1.5$ mm, $d = 1$ mm, $D_s = 5$ mm.

Figure 6.7 and Figure 6.8 show that the resulting FWHM and temperature contrast plot for moving heat source test are identical to the stationary heating. Both findings had an initial increment in FWHM measurements due to the unique circumstances of a small defect size such as $D_s = 5$ mm. This was discussed earlier in the stationary heating section. Meanwhile, the moving heat source result plotted lesser data at early observation time. The reason to this is the additional time taken for a moving heat source to heat up the full model plate surface completely.

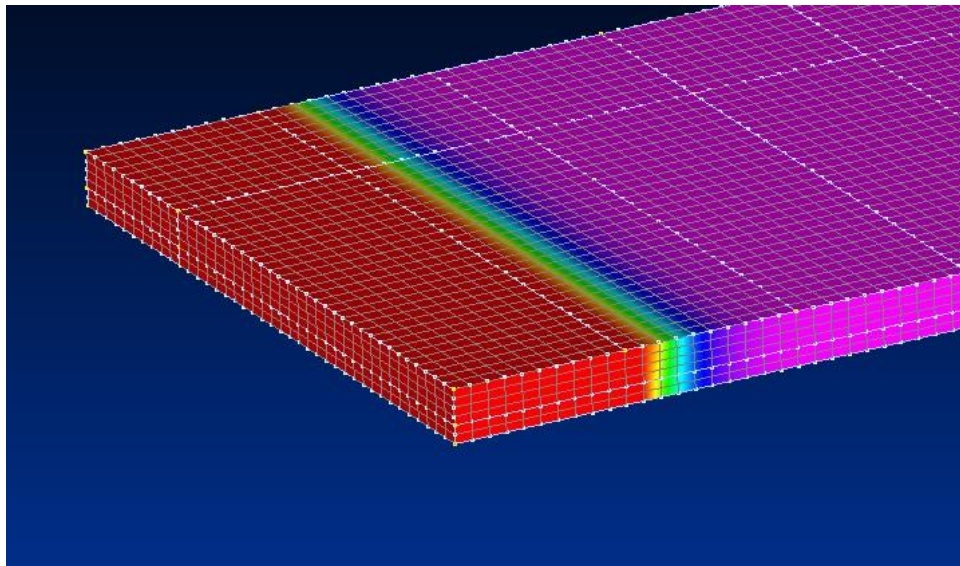
The setup of stationary heating used a short heating period of 2 ms, which is similar to the effective heating period of the moving heat source test. The resulting temperature contrast was similar, suggesting that the lateral effect of heat diffusion during the fast motion of moving heat source was insignificant, hence negligible. The plotting of FWHM measurements also shows minimum differences in the effect of heating motion. This can be further verified by evaluating the effective thermal diffusion length formula.

For the moving heat source speed of 18 km/hr, the total time taken for the heat source to travel across the 120 mm plate length was 0.024 s. Considering only the first segment of the plate surface, thermal waves were expected to diffuse laterally by approximately 1.2 mm in 0.024 s based on the effective thermal diffusion length. However, this number is smaller than the size of each subdivided surface segment (5 mm), in addition to its comparable size with the meshing setup (1 mm). Therefore, the effect of heating motion is insignificant and does not alter the temperature profile of adjacent nodes drastically.

In a circumstance where heating speed is slow, the effect of lateral heat diffusion during the use of moving heat source can be significant. This will affect the rate at which temperature increases for neighbouring regions. The minimum speed of heat source calculated for this lateral effect to be significant is approximately 6 km/hr or slower. It will result in an effective thermal diffusion length of about 2 mm at the end of heating, which would have travelled at least 2 element spaces for this setup. Nevertheless, this is only theoretical-based and was not tested in this context by simulation.

Therefore, for the rest of the test runs in this chapter, the speed of heating source exceeding 18 km/hr will only account for the effect of total thermal energy transferred. The effect of lateral heat diffusion during heating is ignored.

(a)



(b)

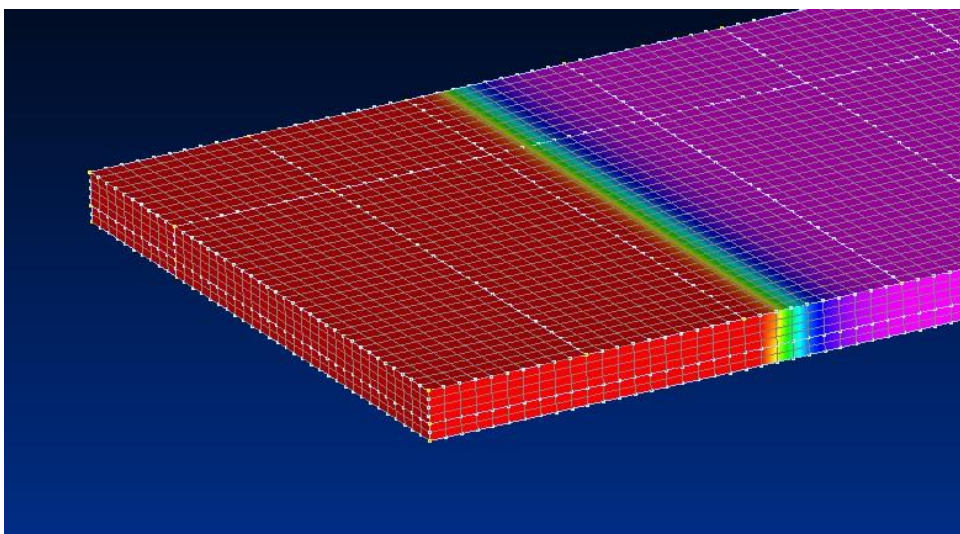


Figure 6.9 Image sequence of moving heat source with slow speed at 0.2 km/hr. Figure (a) at 0.18 s and (b) at 0.38 s.

Figure 6.9(a) shows that at 0.18 s, the adjacent region has begun to experience heating prior to the subsequent motion of heat source. The temperature contour scale was set at 25 – 100 °C, suggesting that there is a significant temperature rise. Figure 6.9(b) also shows that at 0.38 s, the non-heated region has a gradual increase in temperature. This is clearly affected by the extent of lateral heat diffusion due to the slow heating speed. This will, in turn, affect the overall temperature contrast and defect size prediction.

6.2.2 Thick plate with near surface defect

Defect depth at 1 mm

An 8 mm thick model, with $D_s = 10$ mm is located at $d = 1$ mm. The heating speed is set to 18 km/hr, similarly to the previous tests. By removing the appropriate heating time delay, the resulting temperature responses is used to determine the FWHM measurements at different observation time for analysis.

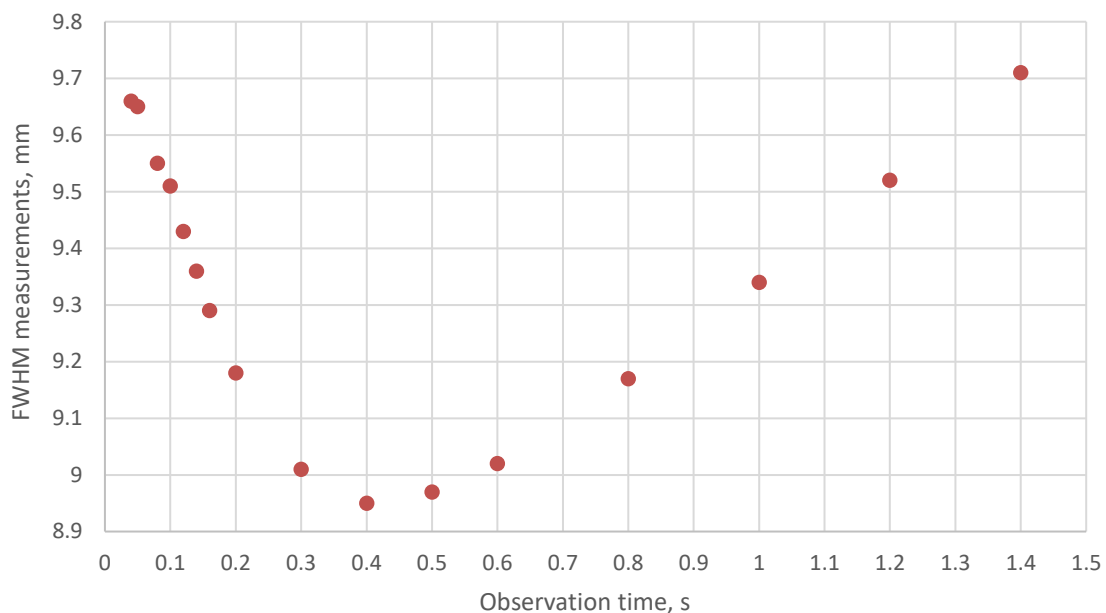


Figure 6.10 FWHM measurements for model $t_p = 8$ mm with $D_s = 10$ mm at $d = 1$ mm. Moving heat source speed at 18 km/hr.

In Figure 6.10, the initial decrease followed by an increment in FWHM measurements is explained by the edge effects, similarly to the stationary heating phenomenon. Initially, the defect size was large enough that thermal energy from the defect edges gradually diffuses to the middle over time, leading to a diminishing trend. At a cut-off time, these edge effects will eventually meet at the centre and reflect off each other to broaden the local temperature concentration at the top surface of the plate.

The FWHM measurement will increase with observation time as the full plate surface reaches thermal equilibrium or minimum temperature contrast where the Gaussian curve becomes flatter. The time at which this occurs is dependent on the effective area of inspection. In this study, the effective area of inspection is equivalent to the size of plate modelled, which is 120 mm.

Considering only the descending trend of the FWHM measurement plot, a 3rd order polynomial was curve fitted and extrapolated to the start time (Figure 6.11). This start time represents the point where heating of each surface segment has been removed. It is not ideal to measure the FWHM at a point where the plate has not experienced heating.

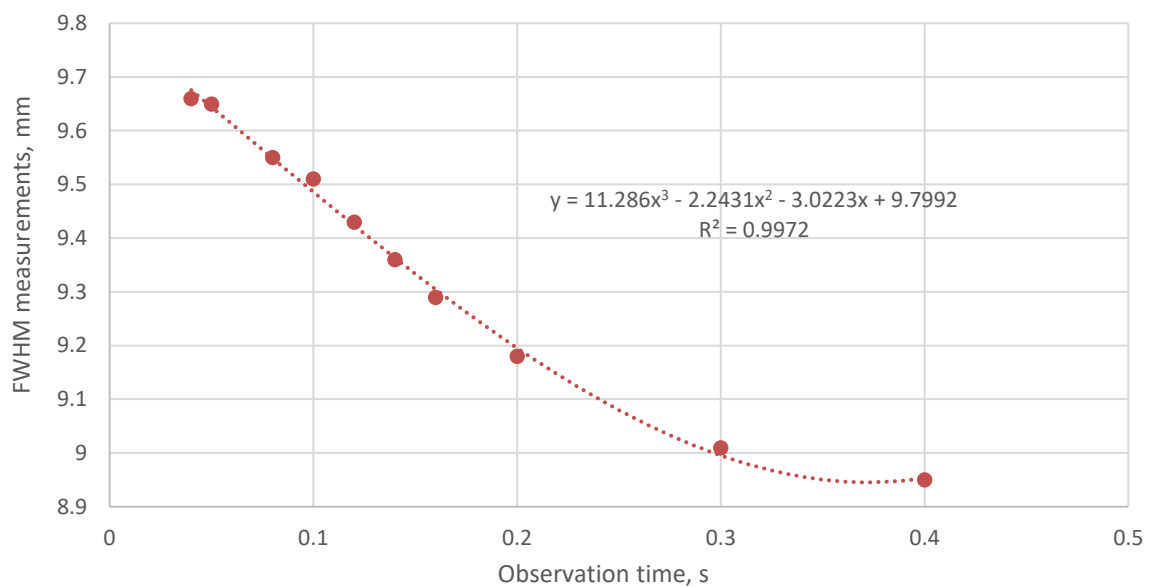


Figure 6.11 The curve fitting and back-extrapolation for the descending trend of FWHM measurements.

Based on the equation generated in Figure 6.11, the predicted defect size of 9.8 mm was compared to its actual size of $D_s = 10$ mm. This is close to the prediction made using the stationary heating technique at 9.67 mm (Table 5.3). Additionally, the 18 km/hr moving heat source test result was more accurate than the stationary heating test setup. This is explained by the slight increase in a period of heating for the moving heat source setup at an average of 3 ms compared to 2 ms in a stationary case. The increase in thermal energy transfer resulted in larger maximum temperature achieved, hence a higher rate of diffusivity causing significant temperature differences across regions with variation in the substructure. Nonetheless, the differences in defect size measurement were small.

When comparing both stationary and moving heat source tests, it is also important to observe that the first recorded FWHM measurement for moving heat source test will usually be found at a later observation time compared to stationary heating. As the heat source travels across the plate, the far

end of the test model will only experience heating later. It will require a slightly later time for surface temperatures to be observed with minimal contrast for analysis purposes. Otherwise, it is shown that the moving and stationary heating results were almost matching. This also applies to other cases where D_s vary between 3 mm, 5 mm, 8 mm and 20 mm.

Defect depth at 2 mm

A new set of simulation and analysis was made for a model with defect located at $d = 2$ mm. This is to validate the test for moving heat source technique.

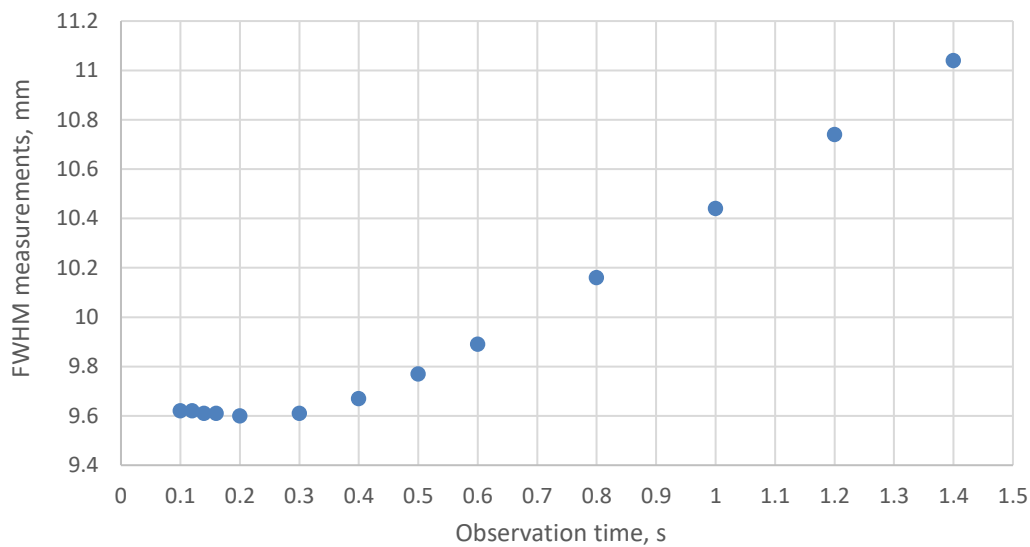


Figure 6.12 FWHM measurements for $t_p = 8$ mm model with $D_s = 10$ mm at $d = 2$ mm. Moving heat source speed at 18 km/hr.

It is clear from Figure 6.12 that the $d = 2$ mm model had an initial FWHM measurement deviating to a later observation time as compared to the $d = 1$ mm model. This is due to the additional 1 mm gap introduced between the plate surface and defect. The temperature responses only began to show visible contrast as illustrated in Figure 6.13 and feasibility for FWHM measurement at a time of 0.08 s after heating, compared to 0.04 s after heating in the $d = 1$ mm model. The other clear differences between the two models are the extent to which the FWHM value increases over time. At 1.4 s after heating, the $d = 2$ mm model had an FWHM measurement of 10.81 mm compared to 9.33 mm of the other model. Since heat had to propagate an extra distance to reach the defect, edge effects will be significant when surface temperature contrast is measured. As a consequence of that, the diminishing FWHM trend was smaller causing larger increment in FWHM measurements.

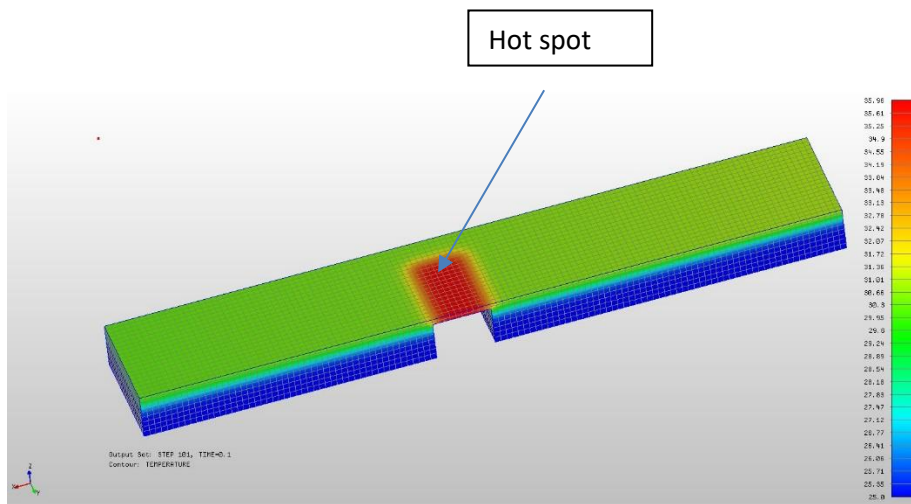


Figure 6.13 A 'hot spot' illustration during the transient cooling of the material.

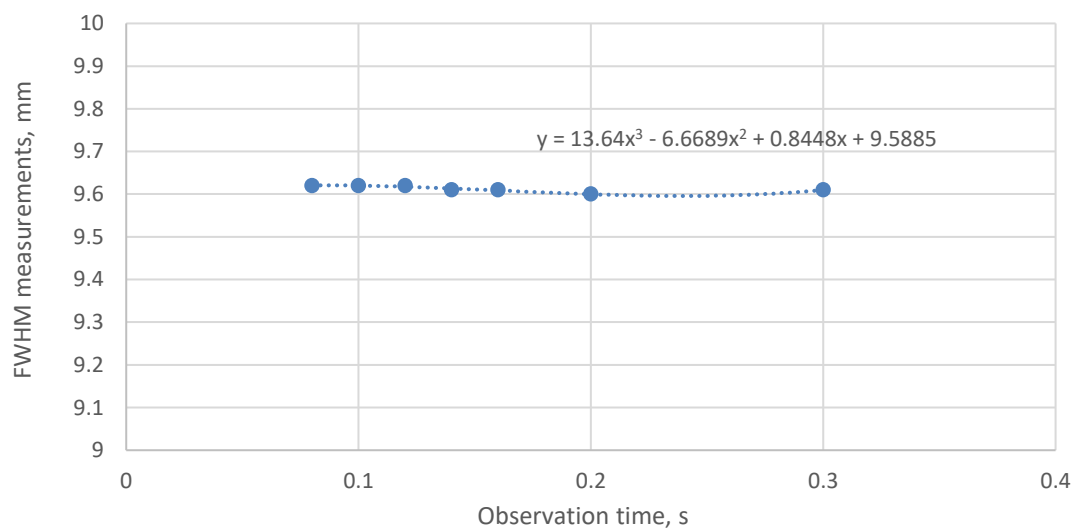


Figure 6.14 Curve fitting and back-extrapolation for the $t_p = 8$ mm model with $D_s = 10$ mm at $d = 2$ mm.

Moving heat source speed at 18 km/hr.

The resulting curve fit in Figure 6.14 shows a defect size prediction of $D_{SE} = 9.59$ mm in this case. This is a less accurate finding, due to its higher uncertainty over its back-extrapolation region. This is closely related to the time at which the initial FWHM measurement is recorded. In fact, the trend matches closely with the stationary heating again. The larger the gap between the plate surface and defect, the larger is the error of predictions. Despite this, the model setup provided predictions to a certain extent of accuracy.

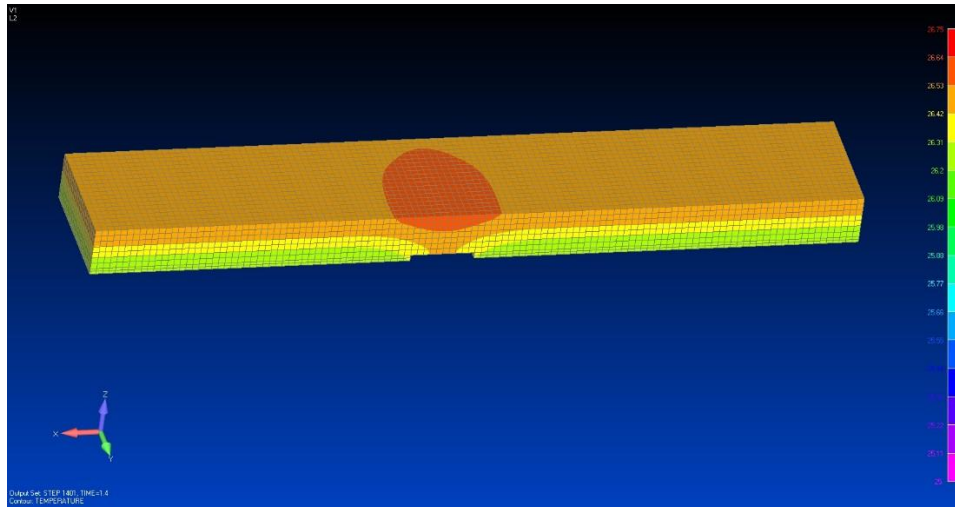
Defect depth larger than 4 mm

For a defect located deeper into the material volume, the time taken to obtain a measurable temperature contrast on the plate surface extends. The first measurable FWHM will occur at a later time. In addition, this FWHM measurement will be strongly affected by edge effect and result in a large value. Consequently, the back-extrapolation approach for defect size prediction will lack accuracy due to the lack of initial FWHM measurements and the significant impact of the edge effect. This has been shown previously in the stationary heating test. The results in Table 6.2 show that the predicted defect size for a defect located at $d = 6$ mm has a high error percentage of 45.4%. The FWHM measurement plot used a linear curve fitting for back-extrapolation, as the 2nd and 3rd order polynomial resulted in a negative defect size prediction.

Table 6.2 Comparison of predicted defect sizes at different depth location into the material volume using moving heat source.

Defect depth, d	Actual defect size, D_s	Predicted defect size, D_{SE}	Differences	Percentage difference
1 mm	10 mm	9.8 mm	0.2 mm	2%
2 mm	10 mm	9.59 mm	0.41 mm	4.1%
6 mm	10 mm	5.46 mm	4.54 mm	45.4%

(a)



(b)

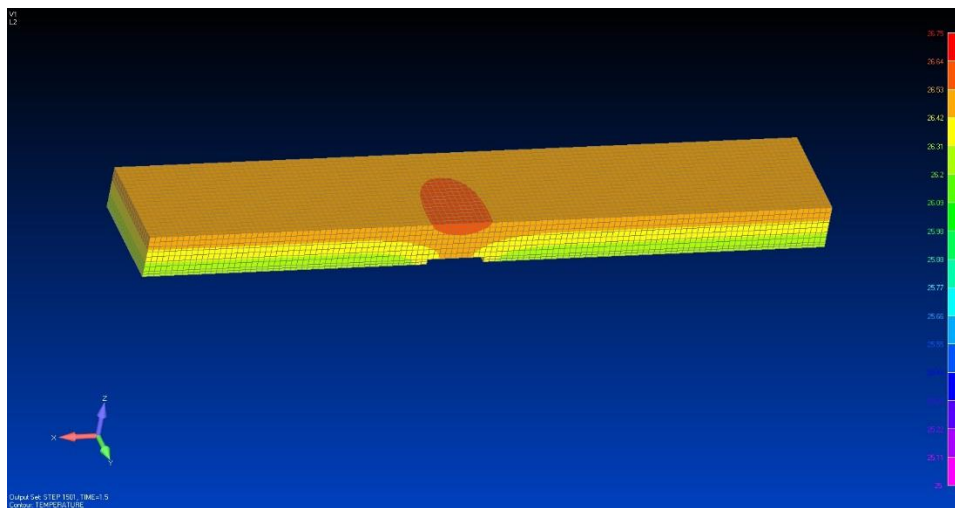


Figure 6.15 Screenshot of transient cooling for a moving heat source test at observation time (a) 1.4 s and (b) 1.5 s with temperature contour at 25 °C – 26.75 °C. Model setup with $t_p = 8$ mm, $d = 6$ mm, $D_s = 10$ mm.

Even with the highly inaccurate defect depth prediction, the moving heat source technique is able to qualitatively detect the presence and position of an underside defect clearly. Figure 6.15 shows that for a thick plate model of $t_p = 8$ mm with a defect at $d = 6$ mm, the surface temperature contrast shows a region of concentrated heat, indicating the presence and position of a potential defect. The size of this concentrated heat region, however, diminishes over an observation time of 1.4 s to 1.5 s. It was important to understand that the temperature contrast between the defective and sound region was small.

6.2.3 Speed Effect

In this section, the effect of moving heat source speed on defect depth prediction accuracy is studied. The same model of $d = 1$ mm was used with an increased heating motion of 54 km/hr. By theory, this implies that each surface segment is transferred with a lower total thermal energy. Despite that, the measurement for defect depth and material local thickness was still possible.

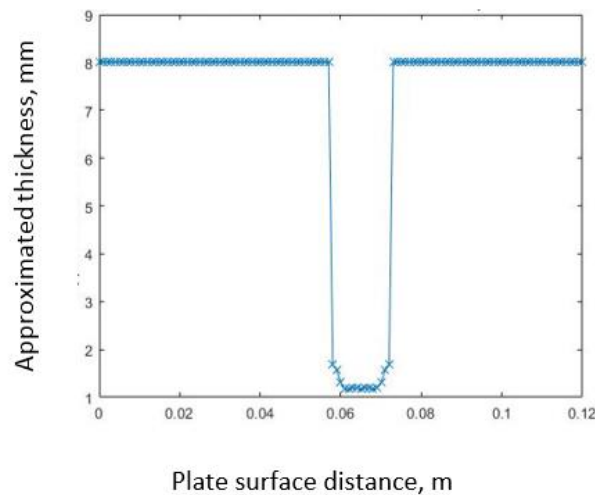


Figure 6.16 Defect depth location in a plate model ($t_p = 8$ mm) with 54 km/hr heating speed.

It is observed from Figure 6.16 that the prediction of defect depth was less accurate compared to the previous test with slower heating speed. The plot shows a defect at a depth of approximately 1.2 mm in oppose to the 1 mm actual depth. This is explained by the reduced maximum achievable temperature as a result of a smaller amount of total heat energy transfer. A lower maximum temperature will achieve similar second order peak derivative time constant, t^* however with a lower plateau temperature. Figure 6.17 demonstrates the plateau temperature profile for higher and lower maximum temperature achieved. The closer proximity of plateau temperature to thermal equilibrium state will subsequently increase the difficulty in accurately predicting the cooling gradient variation in the temperature-time profile. The effect of heating speed on defect size prediction is further discussed in later sections.

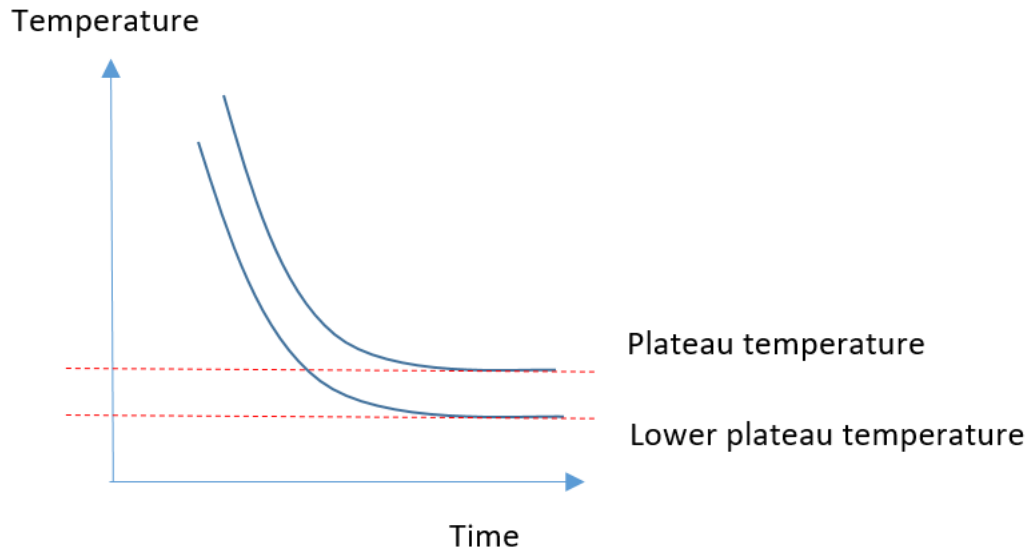


Figure 6.17 Plateau temperature

6.3 Effect of Heating Segment Size (l_s)

In terms of engineering industrial application, the moving heat source technique is ideally able to simulate a heating speed comparable to a moving vehicle such as cars or trains. The two parameters affecting the setup of heating speed are the size of heating segments, l_s and the heating duration of each segment. The size of heating segments is also referred to the size of the heating device. Assuming that there is a large accessibility to different sizes of moving heat source, the first part of this section will vary the heating size while keeping the heating duration constant.

6.3.1 Segment size, $l_s = 10$ mm, heat source speed, $v = 36$ km/hr

For $l_s = 10$ mm with 2 ms heating duration on each segment, the simulated speed of the heat source is 36 km/hr. The model has a thickness of $t_p = 8$ mm with the defect located at $d = 1$ mm. Given that only the size of a heating segment has changed, the total thermal energy applied per unit area remains constant and is not accounted for its effect. The effect of intensity on moving heat source is discussed and reported later.

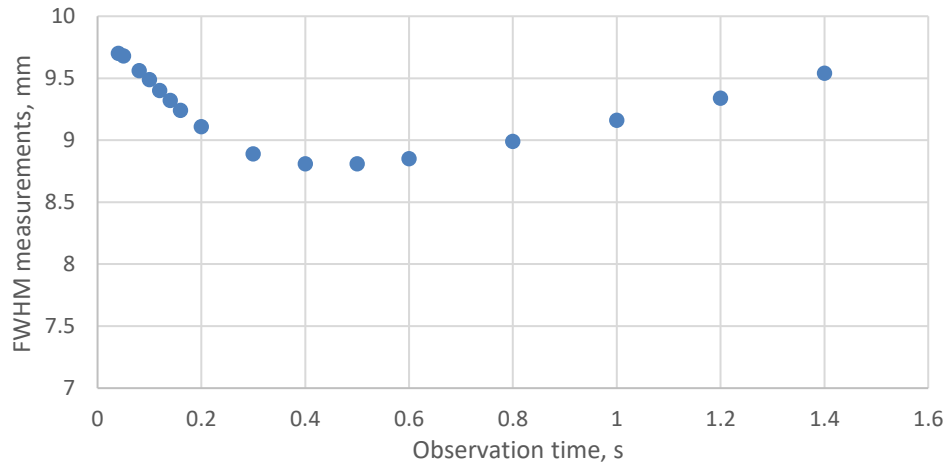


Figure 6.18 FWHM measurements for a model with $l_s = 10$ mm, $t_p = 8$ mm, $d = 1$ mm and $D_s = 10$ mm.

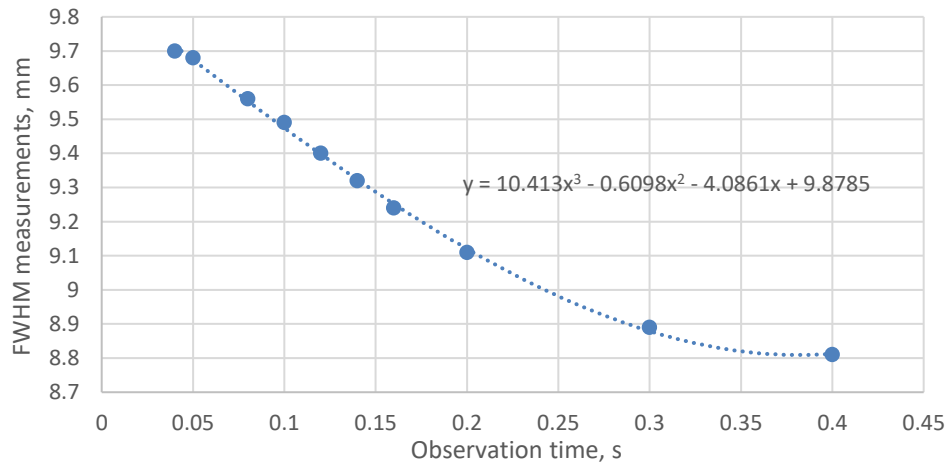


Figure 6.19 Curve fitting and back-extrapolation for defect size estimation.

According to Figure 6.18 and Figure 6.19, the estimated defect size is $D_{SE} = 9.88$ mm. This is a minor improvement from 9.8 mm at 18 km/hr heating speed with $l_s = 5$ mm (Section 6.2.2).

6.3.2 Segment size, $l_s = 15$ mm, heat source speed, $v = 54$ km/hr

For $l_s = 15$ mm with 2 ms heating duration on each segment, the heating speed was calculated as 54 km/hr. All other variables were unchanged on the $l_s = 10$ mm setup as before. The results are displayed and analysed as follows.

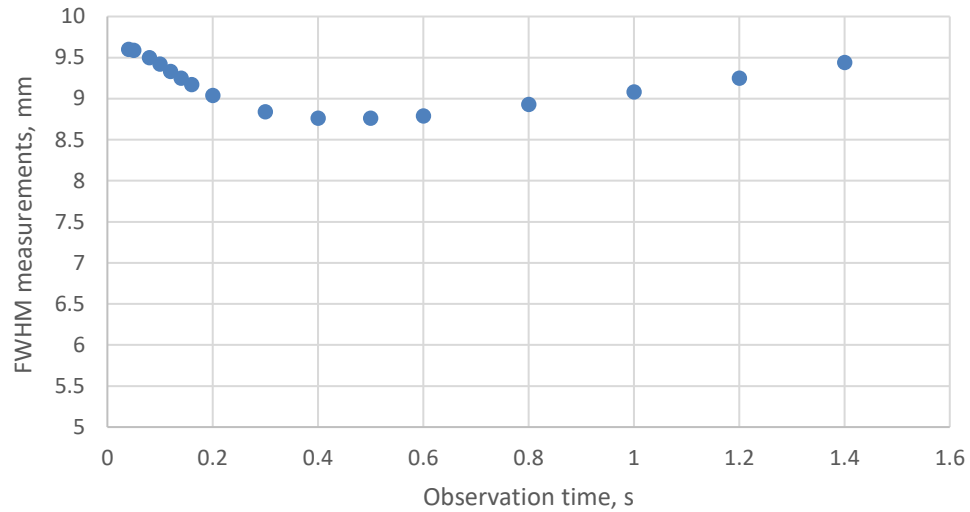


Figure 6.20 FWHM measurements for $l_s = 15$ mm, $t_p = 8$ mm, $d = 1$ mm and $D_s = 10$ mm.

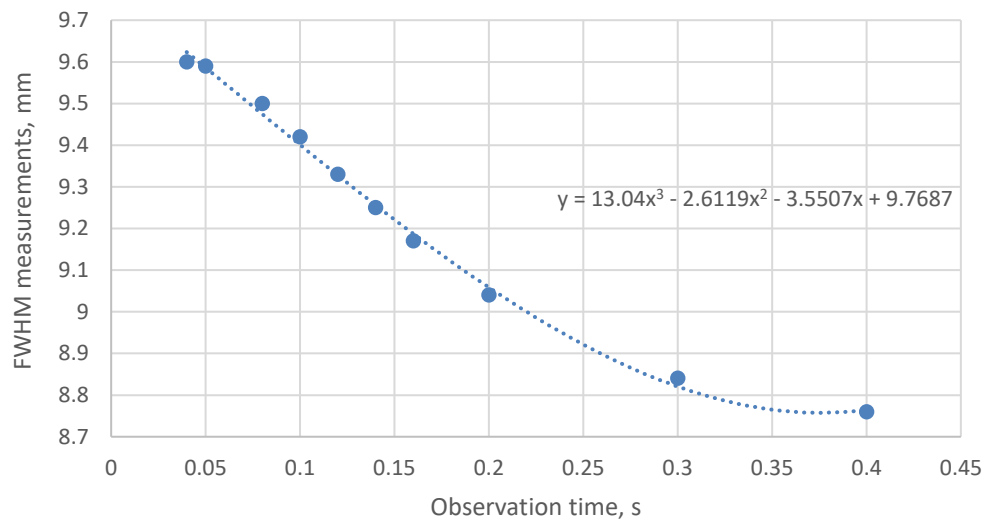


Figure 6.21 Curve fitting and back-extrapolation for defect size estimation.

It can be seen in Figure 6.20 and Figure 6.21 that the estimation accuracy for the 54 km/hr heating speed has dropped to $D_{SE} = 9.77$ mm as compared to the two other heating speed. Table 6.3 shows the comparison summary of different heating segments along with their respective prediction outcome.

Table 6.3 Defect size prediction for different sizes of heating segment size.

Heating speed, v	Size per heating segment, l_s	Actual size, D_s	Defect size prediction, D_{SE}	Differences
18 km/hr	5 mm	10 mm	9.80 mm	0.2 mm
36 km/hr	10 mm	10 mm	9.88 mm	0.12 mm
54 km/hr	15 mm	10 mm	9.77 mm	0.23 mm

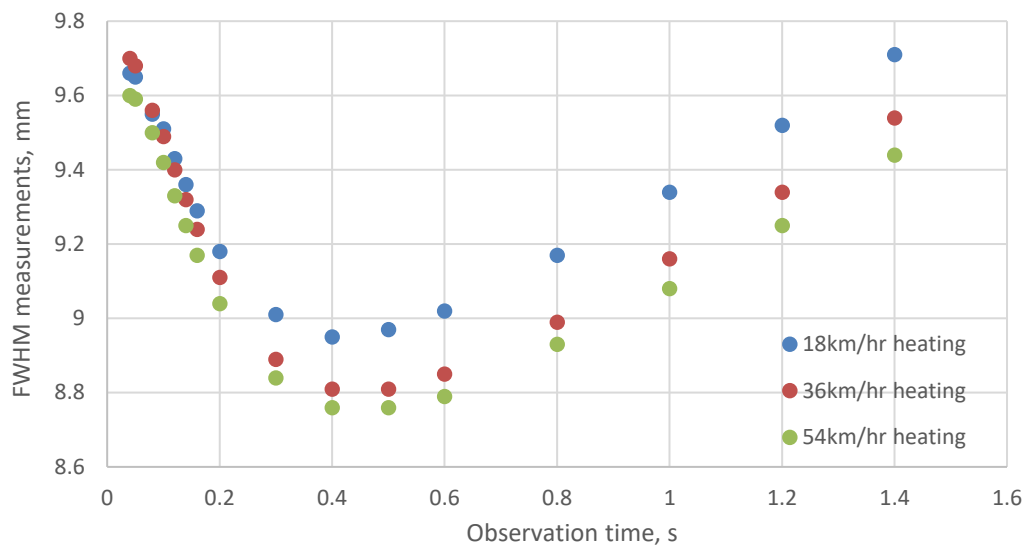


Figure 6.22 FWHM measurement profile for 3 setups with different heating segment sizes, l_s and resulting heating speed, v . Model plate has a thickness of $t_p = 8$ mm, $D_s = 10$ mm, $d = 1$ mm.

Despite the differences in heating speed, the initial FWHM measurements for the three setups were similar as displayed in Figure 6.22. The initial values had a negligible difference of 0.1 mm. Meanwhile, the FWHM measurement differences in later times are explained by the maximum achievable temperature and its respective temperature contrast in Table 6.4 and Table 6.5.

Table 6.4 Temperature contrast.

	Temperature Contrast (°C)		
Time	18 km/hr	36 km/hr	54 km/hr
0.04	2.823	2.789	2.789
0.08	5.087	5.088	5.088
0.1	5.663	5.681	5.68
0.12	6.074	6.11	6.109
0.14	6.379	6.434	6.433
0.16	6.609	6.683	6.681
0.2	6.91	7.019	7.018
0.4	7.029	7.22	7.22
0.6	6.439	6.629	6.629
0.8	5.733	5.904	5.903

Table 6.5 Maximum achievable temperature.

	Maximum Temperature (°C)		
Time	18 km/hr	36 km/hr	54 km/hr
0.04	36.36	36.32	36.32
0.05	36.11	36.1	36.1
0.08	35.97	35.97	35.97
0.1	35.94	35.95	35.95
0.12	35.9	35.93	35.93
0.14	35.85	35.9	35.9
0.16	35.79	35.86	35.86
0.2	35.65	35.76	35.76

The heating rate per unit area is independent of the heating segment size, l_s used. This ideally should lead to a similar temperature contrast and maximum achievable temperature. Nonetheless, there are slight differences in results from Table 6.4 and Table 6.5. The differences in temperature contrast for $v = 18$ km/hr with the pair of $v = 36$ km/hr and $v = 54$ km/hr is due to the setup of the heating width size. For the 18 km/hr heating speed, the l_s of 5 mm width only had partial coverage of the 10 mm underside defect area while heating is in progress. Meanwhile, the heating speed of 36 km/hr and 54 km/hr had l_s of 10 mm and 15 mm width which covered the full defect size during heating. This suggests that full-size defect was exposed to longer heating for a small heating size as compared to the other setups. More heat is concentrated and captured in the region, causing an initial rise in temperature contrast. Since higher temperature is achieved, the material volume is expected to dissipate heat at a higher rate, resulting in the lowered temperature and FWHM measurement variation at a later observation time.

6.4 Effect of Heating Duration per Segment

Previously, the size of the heating segment was varied to simulate a range of heating speed while maintaining the heating duration of each segment in the previous section. This section will investigate the alternative. The heating segment size, l_s will now be fixed at 10 mm while the heating duration of each segment is set to 1 ms. For this circumstance, the heating speed, v was calculated as 72 km/hr. Since the heating duration is halved, the total thermal energy per unit area is also halved as they have a proportionate relationship. The eventual temperature contrast measured at the model surface is lowered. In addition, the maximum temperature at respective observation time is also reduced. This is due to the shorter exposure period to the heat source. Figure 6.23 and Figure 6.24 express the FWHM measurements recorded for this test and the respective curve fitting for back-extrapolation.

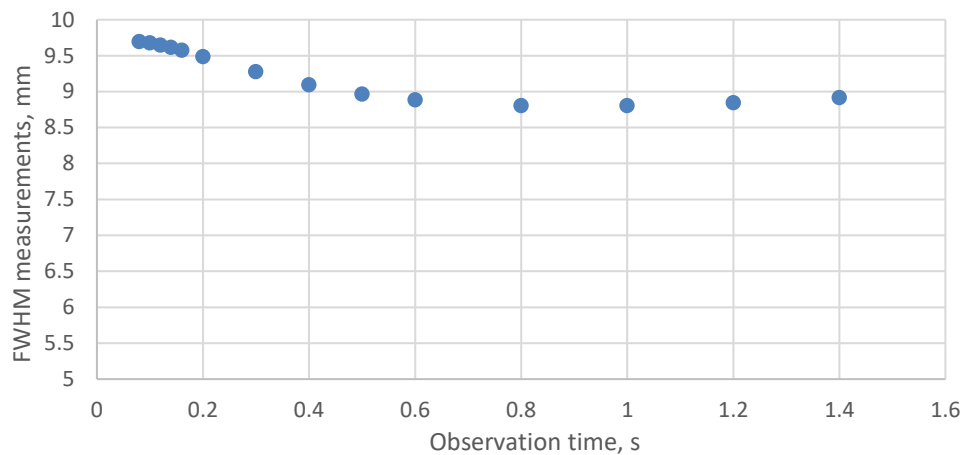


Figure 6.23 FWHM measurement profile for 1 ms heating duration per segment for a model of $t_p = 8$ mm, $d = 1$ mm and $D_5 = 10$ mm.

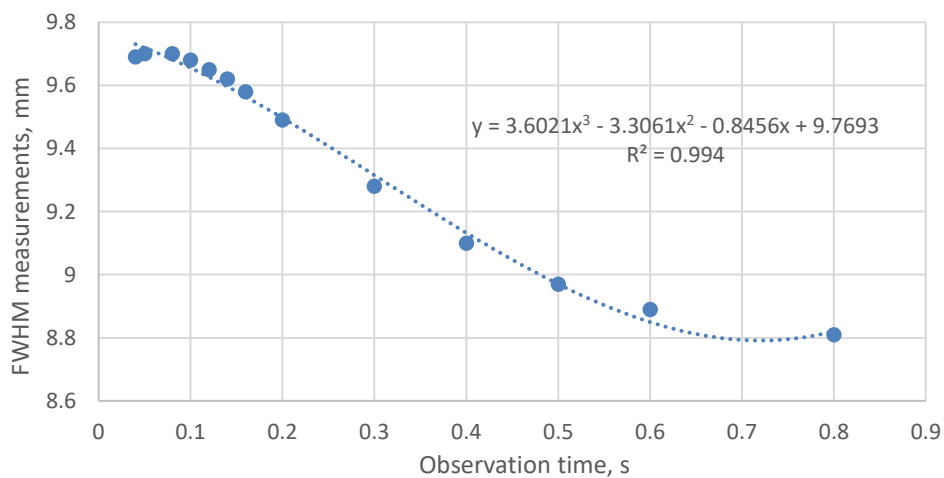


Figure 6.24 Curve fitting and back-extrapolation for defect size estimation.

This model setup has shown potential in forecasting the defect size at high speed. However, it is important to notice that the initial FWHM measurement has gradually shifted to later observation time. When collecting results at early observation time (i.e. 0.04 s and 0.05 s), it was found that even though the temperature contrast threshold of 0.1°C was achieved, the graph was not ideal for analysis. There were significant noises at the tail end of the plot, suggesting errors in the temperature profile. Therefore, only FWHM measurements at 0.08 s and later were taken into consideration. This resulted in larger uncertainty for back-extrapolation.

The setup for $v = 72$ km/hr is similar to the test setup of $v = 36$ km/hr. Both test model has characteristic of $l_s = 10$ mm, $D_s = 10$ mm and $d = 1$ mm. The heating duration on each segment is different nonetheless: one at 2 ms heating while the other at 1 ms heating. This led to the clear observation on temperature contrast results. For the setup with shorter heating, the total amount of thermal energy transferred is subsequently lowered, leading to a reduced maximum temperature. The temperature contrast across the model surface for three different heating speeds can be seen in Figure 6.25.

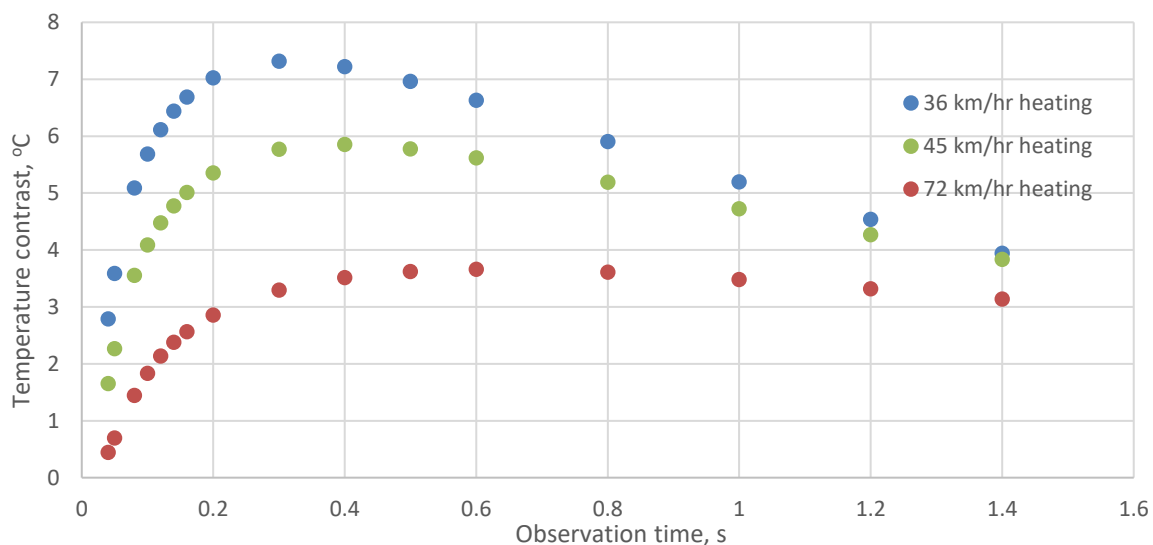


Figure 6.25 Comparison of temperature contrast for three different heating duration setup.

When comparing the FWHM measurement for the heating speed of 36 km/hr and 72 km/hr, both tests had initial FWHM measurement at approximately 9.7 mm. However, the change in FWHM measurement differs with time as suggested in Figure 6.26. This is explained by the rapid diffusion in the $v = 36$ km/hr setup, where temperature contrast is higher. The faster rate of diffusion indicates that the FWHM measurements will decrease abruptly at an early observation time, and increase rapidly at a later observation time. In terms of defect size prediction accuracy, the faster heating speed (72 km/hr) had a larger error in prediction of 0.23 mm, compared to 0.12 mm of the slower heating

speed. This is explained by the lack of temperature contrast for the high-speed heating. Regardless of the findings, the fast heating speed is able to provide fair accuracy of prediction.

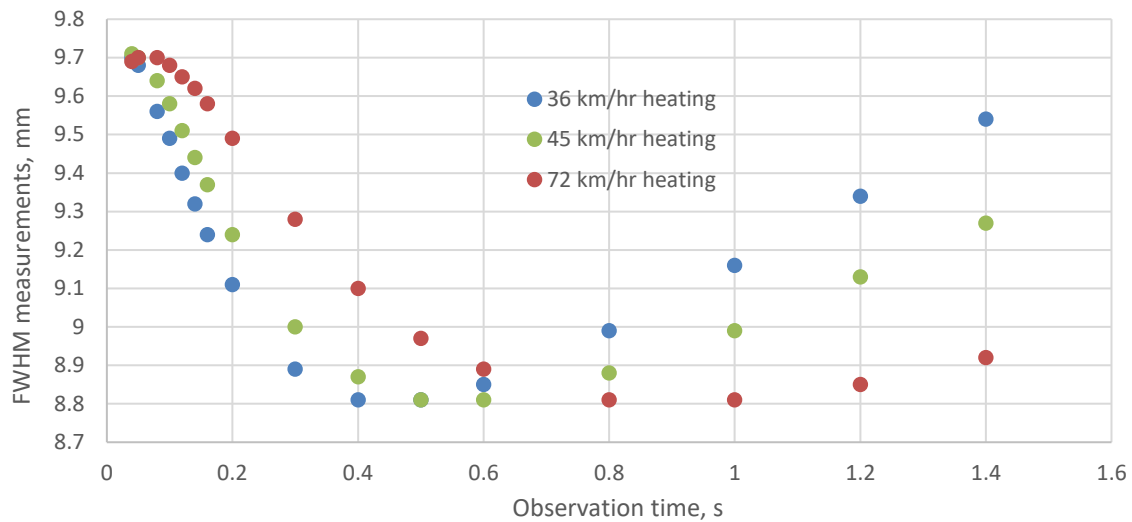


Figure 6.26 FWHM measurement profile comparison for three different heating duration in a model of $t_p = 8$ mm, $d = 1$ mm and $D_s = 10$ mm.

The third set of test was also conducted for an intermediate heating speed of $v = 45$ km/hr. It is anticipated that the resulting temperature contrast and FWHM measurements trend fell between the 36 km/hr and 72 km/hr speed setup. All results were tabulated in Table 6.6 for comparison.

Table 6.6 Summary for defect size prediction under different heating duration per segment.

Heating duration	Moving heat source speed, v	Actual defect size, D_s	Predicted defect size, D_{SE}	Differences
3 ms	36 km/hr	10 mm	9.88 mm	0.12 mm
2.4 ms	45 km/hr	10 mm	9.84 mm	0.16 mm
1.5 ms	72 km/hr	10 mm	9.77 mm	0.23 mm

In practice, the temperature contrast threshold is useful information in determining the separation distance between the heat source and thermal detector while both mounted on a moving platform. In a setup of 18 km/hr with a defect at 2 mm depth in a plate model, the average separation distance required is 0.12 m. This allows a total observation time of 0.024 seconds for temperature contrast to exceed the threshold value.

6.5 Chapter Conclusion

The propagation of moving heat source in this chapter is simulated by creating multiple stationary heating on the model surface segments over a length of time. Each segment is heated sequentially with a heating time delay. For the analysis of moving heat source test, the removal of heating time delay is predicted to result in a similar outcome as the stationary heat source test. Thus, the understanding of the results in Chapter 6 can be referred to the discussions developed in the stationary heating test. The limitation in measurements for the moving heat source test is ideally similar to the stationary heating setup given the assumptions made.

First, the estimation of defect depth was conducted. It was found that for the $t_p = 2$ mm model with a defect at $d = 1$ mm, the predicted defect depth was accurate. Minor discrepancies were found while increasing the defect size; nonetheless, it still offered a relatively good prediction. As the defect depth increased, this accuracy began to deteriorate. The results from this section showed that there is a matching relationship between the moving heat source and stationary heating results. Using this understanding, predictions of deep defects were justified based on prior knowledge.

The FWHM method for moving heat source was tested with a thin plate (small t_p) with varying defect sizes and thick plate (large t_p) with near surface defect (small d). All tests showed good accuracy. For the prediction of defect sizes in a defect depth of $d = 6$ mm, previous work in stationary heating showed that FWHM measurements were inaccurate and a bad accuracy prediction was achieved. This suggested that the moving heat source will have the same outcome. It was also found that the magnitude of the heating speed does not affect the accuracy of defect size and depth prediction. It has been simulated in this section that high-speed heating was able to provide fair accuracy of predictions. The size of the heating device (segment size) and the heating duration of each segment were the main influences of results outcome in moving heat source test. A heating segment size, l_s smaller than the defective region will cause local temperature concentration. A shorter heating duration per segment will reduce maximum achievable temperature and temperature contrast.

In conclusion, the maximum detectable defect size and depth for a moving heat source test is closely related to a stationary heat source setup. The maximum detectable depth of any defect sizes, d is approximately 6 mm, while minimum detectable defect size at near surface is $D_s = 5$ mm. Meanwhile, when considering the speed factor of the heat source, the accuracy of predictions will change.

7. Conclusion and Recommendations

The need for constant inspection on rail track defects is undoubtedly necessary. It can reduce fatalities and minimise financial losses that are due to unfortunate events. With that in mind, the aim of this research is to study the potential of mounting a heat source on a moving bogie, to perform motion-heating across a rail track base at high speed. The device will be able to quantitatively and qualitatively measure for any underside defects. In this research, to begin with, the tests on stationary heating was initially performed with a flat plate model that represents a complex rail structure. This also allows the study on the developed methodologies. Later, a model with moving heating was created and tested. Results in this study can be useful for future work when integrating this study onto an actual rail base and moving bogie.

Based on literature reviews, it is best to perform structural inspection with non-contact and preferably non-destructive evaluation methods. The infrared thermography technique is safe, cheap, fast and more portable than any of the other NDE methods available. In addition, it is able to inspect complex geometry such as the rail base structure. Meanwhile, pulsed thermography was also preferred due to its smaller thermal loading and fast inspection time compared to lock-in thermography and step-heating thermography.

7.1 Main Findings and Discussions

The main objective of this thesis was approached with computational modelling. To begin with, a flat plate model was created with a fixed dimension of 120 mm x 20 mm with varying thickness as part of the investigation variable. An underside defect was created with varying sizes. The preliminary investigation of this research applied heat on the model surface using a stationary heat source. This is an important aspect of the research as it provided a better insight and knowledge on thermography testing. It also allowed a better understanding of the quantitative measurement techniques such as second order peak derivative method and full width at half maximum (FWHM). The second order peak derivative method was used to evaluate the material local thickness and defect depth, whereas the FWHM was used to measure the underside defect sizes.

Stationary heating (defect depth)

In the stationary heating test, a defect is defined present if the resulting material local thickness measurements showed unevenness in profile. The depth of the defect then corresponds to the local thickness at that point.

- (i) For a 2 mm thin plate with defect located at 1.5 mm beneath the surface, the variation in underside defect size did not affect the prediction accuracy of defect depth.
- (ii) For defects in close proximity to the plate surface (2 mm gap) in a thick plate (8 mm), the prediction of defect depth was the most accurate. As defect depth increases (in the range of 4 mm to 7 mm), the prediction accuracy for the depth deteriorates.

An 8 mm plate thickness with a defect at 7.5 mm depth showed the largest error in results. For deep defects, the significant effect of lateral heat diffusion caused the surface temperature to be lowered, moreover affecting the point in time where one-dimensional assumption deviates. Apart from that, results were also affected by the high order polynomial fitting that may have removed information from non-fitted data. Lastly, the Fourier time domain fitting which was used may be inappropriate for each circumstance, causing increased in prediction error. This section provided an initial study on defect depth and sizes limitations.

Stationary heating (defect lateral size)

The following investigation on stationary heating focused on the measurement of underside defect size. Using the FWHM method, a defect is present if a minimal contrast of 0.1 °C is observed from the temperature profile.

- (i) Results showed that the defect size prediction is most accurate when a large defect is present in a thin plate with near-surface location. During the transient cooling phase, edge effects commence at a later time as the opposite edges of the defect were located further apart. The resulting diminishing FWHM trend became more significant, allowing higher efficiency in data back-extrapolation.
- (ii) Despite the increment in overall plate thickness, prediction accuracy of defect size is promising provided the defect is located near the surface of inspection.
- (iii) For a large area of material thinning in a thick plate model, it was found that the defect vicinity will alter the accuracy of prediction outcome.
- (iv) Results also showed that the prediction error increases as the defect is located deeper into the material volume. Thermal energy dissipates to the surrounding as it propagates towards the deep defect. This led to a lowered temperature response and a smaller temperature contrast. The eventual results will lack accuracy as it will also be affected by the significance of edge effects due to long observation time as discussed earlier.

The limitation on defect size prediction can be overcome by extending the heating period. This approach allows the longer saturation of heat at the surface of the material, furthermore allowing a

shorter transient cooling phase that will transition to two-dimensional heat transfer at later observation time. Nevertheless, it was important to avoid producing a step-heating thermography scenario. Additionally, the total amount of thermal energy transferred has to be monitored.

Moving heat source (defect depth)

The analysis on a stationary heating test was crucial as it acts as a reference setup to the moving heat source test. The major difference between the two testings was the heating procedure. Instead of simultaneous heating on the full model surface, moving heat source test was conducted by the sequential heating of subdivided surface segments. The measured temperature responses will have a motion-like feature. When analysed, the results were mostly similar to the stationary heating.

- (i) The removal of heating time delay resulted in an accurate prediction of defect depth in particular for a thin plate model (2 mm) when using moving heat source.
- (ii) The deeper location of a defect in a material volume showed deteriorating trends of prediction ability.

In comparison to results ascertained from stationary heating, both tests had matching behaviour. It is, therefore, suggested that the detection ability of stationary heating is similar to moving heat source in most aspects.

Moving heat source (defect lateral size)

As for the prediction of defect sizes in moving heat source test, simulations were mainly conducted on thin plates with varying defect sizes and thick plates with near surface defects. The results collected and analysed had great similarity to the stationary heating test. This further highlighted the approximation of both types of heating. In conjunction to this assertion, the measurement of defect sizes at a deep location into the material volume was briefly discussed. The high speed moving heat source can qualitatively detect underside defects regardless of the defect depth location.

The effect of heating speed was tested and concluded as below.

- (i) The heating speed has no significant impact on the accuracy of the prediction results.
- (ii) For a heating segment size comparable to the actual defect size, local temperature concentration will take place, thus increasing the maximum temperature achieved.
- (iii) The longer heating period on each subdivided surface segment will result in shorter transient cooling phase, allowing larger temperature contrast to be achieved.

7.2 Implications

Stationary heating is a safe and efficient non-destructive evaluation test method. The maximum measurable temperature in the stationary heating test was in the range of 40 °C to 50 °C. It is harmless to the experimenter and material. The use of a 2 ms pulse heating resulted in low temperature yet fast inspection rate. However, for inspection on large structures such as a distance of rail tracks, the use of stationary heating is not a feasible option. The alternative and innovative technique of using a moving heat source can counter this problem. At a heating rate of 0.1 s per designated segment, the use of a moving heat source allows up to 60 km/hr of inspection speed. This is able to cover a great length of rail tracks for inspection. It is a more reasonable approach than performing stationary heating on one segment after another. For moving heat source to success, a maximum separation of 0.13 m between the source and thermal detector is crucial as it defines the optimum observation time frame for temperature response.

The moving heat source is approximated as multiple stationary heating on model segments. Due to the high-speed motion of the heat source, the measured temperature response is matching with a stationary heating setup. The introduction and purpose of the moving heat source study are to implement the technique on rail monitoring and conditioning. A typical rail base has a thickness gradient varying between 8 mm to 11 mm [60], therefore there is the wide usage of thick plates up to 8 mm in this research. The investigation on thin plates for both stationary and moving heat source is an initial study to the potential limitations in a thicker plate.

For the case where rail base fractures, indentations (defect) are usually originated at the edge of the rail base and grow into the rail base. At a critical growth of 12.7 mm (1/2 inch), the rail base will experience a full rupture [61]. The moving heat source in this research has shown the ability to detect large defect sizes confidently. At a 5 mm defect size, the quantitative ability is highly reliable and improves as defect size increases. However, this is limited when the location of the defect is deep into the rail base. The occurrence of base fracture is common near the base of the rail base. This research shows poor accuracy in quantitative measurements despite its superior qualitative ability. The limiting measuring depth of 6 mm is approximately 2 mm to 5 mm short of an actual rail base geometry. Any increment in defect depth will result in low accuracy predictions. Nonetheless, for the random propagation of defect growth as a result of crack propagation or corrosion into the rail web, moving heat source test will be efficient.

In summary, a critical defect of up to 12.7 mm is certainly detectable with the use of moving heat source. In this thesis, depth measurements are limited to defects at the base. However, any subsequent growth towards to the rail base surface will allow for improved size and depth estimation.

The results of this research have shown that the use of moving heat source is able to detect defect sizes and depths in a material volume. The approximation of moving heat source to stationary heating was acceptable as they share similar limitations in prediction measurements. It can be assumed that this approximation is however only valid for high speed moving heat source of 18 km/hr or greater. The approach is valid in the present case as the time constant of heat diffusion process is relatively larger than the speed of heat source. The effect of lateral heat diffusion during the heating phase is insignificant as temperature responses measured were similar to stationary heating. Nonetheless, this is not applicable to a slower heating speed. Likewise, for materials with higher thermal conductivity, refinement of time steps and a shortening of heating zones will be required.

7.3 Limitations and Future Works

There are several limitations to this study that restricted the extent of this research. First, the time restriction and software limitation has hindered the possibility of creating large plate models with fine meshing and extended simulation time. A longer simulation time with finer meshing will allow better insight on defect detection of thicker plates (8 mm or more). Next, there may be alternate techniques to improve the defect prediction accuracy at a deep location. The FWHM and second order peak derivative clearly showed limitations in deep defects analysis. Finally, the assumptions made in this simulation study were unable to account for many other external factors such as atmosphere humidity and surrounding air flow. These factors will contribute to larger discrepancies as compared to ideal simulation test result.

The concept of developing a moving heat source as a form of structural inspection over a rail base is promising. This thesis has shown that high speed moving heat source is possible given that certain assumptions were made. In terms of computational modelling, further works can be done on a rail base model. This is especially different and poses greater difficulty due to the unsymmetrical shape of rail base. It has an I-beam shape with a slope, raising concerns about heat transfer behaviour. On top of that, the findings in this thesis can be put onto validation by performing experimental tests on test plates as an initial step, followed by a more complicated shape similar to the rail base.

In this study, it was found that limiting the subdivided segment sizes or restricting the heating time for simulation purposes was challenging. Alternatively, the heating speed can be modified in a different approach. For future attempts, one can use multiple heat sources to create similar heating speed with longer exposure time and coverage of heating. The idea of the setup is similar to Figure 7.1. This will allow the use of high speed moving heat source in a more efficient approach with a larger amount of thermal energy transfer.

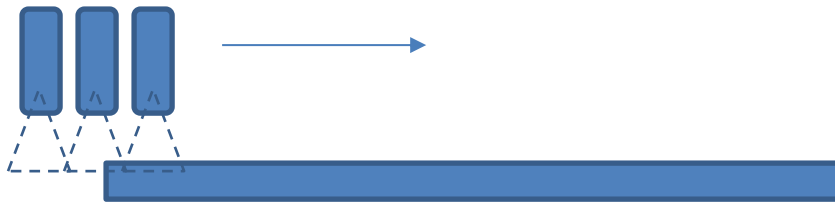


Figure 7.1 Illustration of multiple heating sources stacked one after another.

A series of test results on a range of defects deeper than 6 mm can be tested to tabulate a standardised table for defect size estimation. Taking into account for the relative inaccuracy in respective results, the table can be used as a prediction tool for the field since the critical size of 12.7 mm is known.

In conclusion, it has shown that the use of moving heat source for defect measurement has great potential. It is assumed to have a similar behaviour to a stationary heat source when heat is applied at a high-speed propagation. Despite the effort, it was proven difficult to measure defects that are located deep within the material volume, especially with the use of short time heating.

8. References

1. Rose, J., M. Avioli, and W. Song, *Application and potential of guided wave rail inspection*. Insight, 2002. **44**(6): p. 353-358.
2. Wilkinson, A. *Long range inspection and condition monitoring of rails using guided waves*. in *Proc. 12th Int. Conf. Exhib., Railway Eng., London, UK*. 2013.
3. Rizzo, P., et al., *Ultrasonic guided waves-based monitoring of rail head: laboratory and field tests*. Advances in Civil Engineering, 2010. **2010**.
4. Service, E.N. *The Indian Express*. 2014 [cited 2014 October]; Available from: <http://indianexpress.com/article/india/india-others/chronology-of-major-train-accidents-in-recent-years/2/>.
5. Wooh, S.-C. and A. Clay, *High-Speed Monitoring of Surface Defects in Rail Tracks Using Ultrasonic Doppler Effect*, in *Review of Progress in Quantitative Nondestructive Evaluation*. 1998, Springer. p. 1681-1688.
6. Peng, D. and R. Jones, *Lock-in thermographic inspection of squats on rail steel head*. Infrared Physics & Technology, 2013. **57**: p. 89-95.
7. Tsunashima, H., et al. *Condition monitoring of railway track and driver using in-service vehicle*. in *Railway Condition Monitoring, 2008 4th IET International Conference on*. 2008. IET.
8. Coccia, S., et al., *Noncontact Ultrasonic Guided-Wave System for Rail Inspection: Update on Project at University of California, San Diego*. Transportation Research Record: Journal of the Transportation Research Board, 2011(2261): p. 143-147.
9. Balasubramaniam, P.R. *Indian Institute of Technology Kanpur (IITK)*. [cited 2014 July]; Available from: <http://www.iitk.ac.in/infocell/iitk/newhtml/storyoftheweek60.htm>.
10. Guechaichia, A. and I. Trendafilova. *A simple method for enhanced vibration-based structural health monitoring*. in *Journal of Physics: Conference Series*. 2011. IOP Publishing.
11. Schubel, P., et al., *Review of structural health and cure monitoring techniques for large wind turbine blades*. Renewable Energy, 2013. **51**: p. 113-123.
12. Staszewski, W., S. Mahzan, and R. Traynor, *Health monitoring of aerospace composite structures—Active and passive approach*. Composites Science and Technology, 2009. **69**(11): p. 1678-1685.
13. Diamanti, K. and C. Soutis, *Structural health monitoring techniques for aircraft composite structures*. Progress in Aerospace Sciences, 2010. **46**(8): p. 342-352.
14. Kral, Z., W. Horn, and J. Steck, *Crack propagation analysis using acoustic emission sensors for structural health monitoring systems*. The Scientific World Journal, 2013. **2013**.

15. Chan, T., et al., *Effective Discrimination of Acoustic Emission Source Signals for Structural Health Monitoring*. Advances in Structural Engineering, 2012. **15**(5): p. 707-716.
16. Rabiei, M. and M. Modarres, *Quantitative methods for structural health management using in situ acoustic emission monitoring*. International Journal of Fatigue, 2013. **49**: p. 81-89.
17. Papaelias, M., et al., *Inspection and structural health monitoring techniques for concentrated solar power plants*. Renewable Energy, 2016. **85**: p. 1178-1191.
18. (ASNT), T.A.S.f.N.T. *Introduction to Nondestructive Testing*. 2015 [cited 2014 October]; Available from: <https://www.asnt.org/MinorSiteSections/AboutASNT/Intro-to-NDT>.
19. Rotolante, M.T.a.R., *NDT in Composite Materials with Flash, Transient, and Lock-in Thermography*, I. MoviTHERM, Editor. 2011.
20. Badghaish, A.A. and D.C. Fleming, *Non-destructive inspection of composites using step heating thermography*. Journal of composite materials, 2008. **42**(13): p. 1337-1357.
21. Vavilov, V.P., *Non-contact one-sided evaluation of hidden corrosion in metallic constructions by using transient infrared thermography*. Revista de metalurgia, 2003: p. 235-242.
22. Ahlborn, T., et al., *The state-of-the-practice of modern structural health monitoring for bridges: a comprehensive review*. 2010.
23. Oswald-Tranta, B. and S.M. Shepard. *Comparison of pulse phase and thermographic signal reconstruction processing methods*. in *SPIE Defense, Security, and Sensing*. 2013. International Society for Optics and Photonics.
24. Baek, S., et al., *Nondestructive corrosion detection in RC through integrated heat induction and IR thermography*. Journal of Nondestructive Evaluation, 2012. **31**(2): p. 181-190.
25. Broberg, P. and A. Runnemalm. *Detection of surface cracks in welds using active thermography*. in *18th World Conference on Nondestructive Testing*. 2012.
26. Feng, L., P. Zou, and N. Tao. *Elimination of reflection induced artifacts in flash thermography*. in *Photonics Asia 2010*. 2010. International Society for Optics and Photonics.
27. Oswald-Tranta, B. and M. Sorger, *Scanning Pulse Phase Thermotgraphy with inductive line source*. Proc., QIRT-2012-264, 2012.
28. Huang, S., et al. *NDE of composites delamination by infrared thermography*. in *NDE for Health Monitoring and Diagnostics*. 2003. International Society for Optics and Photonics.
29. Sharath, D., M. Menaka, and B. Venkatraman, *Defect characterization using pulsed thermography*. Journal of Nondestructive Evaluation, 2013. **32**(2): p. 134-141.
30. Shepard, S.M. *Flash thermography of aerospace composites*. in *IV Conferencia Panamericana de END Buenos Aires*. 2007.
31. Pilla, M., et al. *New absolute contrast for pulsed thermography*. in *Proc. QIRT*. 2002.

32. Genest, M., et al. *Comparison of thermography techniques for inspection of CF-18 honeycomb structures*. in *Aircraft Aging 2007 Conference*. 2007.
33. Abidin, I., et al. *Advantages and Applications of Eddy Current Thermography Testing for Comprehensive and Reliable Defect Assessment*. in *Proceedings of 18th World Conference on Nondestructive Testing, Durban, South Africa*. 2012.
34. Kominsky, J.R., J. Luckino, and T. Martin, *Passive infrared thermography—a qualitative method for detecting moisture anomalies in building envelopes*. Tedford and Pond, 2007.
35. Feng, L., R. He, and Y. Zhang. *Measurement of defect depth by peak second derivative method in pulse thermography*. in *International Symposium on Photoelectronic Detection and Imaging 2011*. 2011. International Society for Optics and Photonics.
36. Swiderski, W. *Lock-in Thermography to rapid evaluation of destruction area in composite materials used in military applications*. in *Quality Control by Artificial Vision*. 2003. International Society for Optics and Photonics.
37. Shepard, S.M., J.R. Lhota, and T. Ahmed. *Measurement limits in flash thermography*. in *SPIE Defense, Security, and Sensing*. 2009. International Society for Optics and Photonics.
38. Cantello, C. *Depth determination using thermal imaging*. in *Optics East*. 2004. International Society for Optics and Photonics.
39. Quek, S. and D.P. Almond, *Defect detection capability of pulsed transient thermography*. *Insight-Non-Destructive Testing and Condition Monitoring*, 2005. **47**(4): p. 212-215.
40. Balageas, D. *Thickness or diffusivity measurements from front-face flash experiments using the TSR (thermographic signal reconstruction) approach*. in *Proceedings of 10th Quantitative InfraRed Thermography conference, paper QIRT2010-011 Québec (Canada)*. 2010.
41. Ishikawa, M., H. Hatta, and S. Utsunomiya, *Effects of heating duration on pulse phase thermographic non-destructive testing*. *Infrared Physics & Technology*, 2013. **61**: p. 216-223.
42. Bergman, T.L., F.P. Incropera, and A.S. Lavine, *Fundamentals of heat and mass transfer*. 2011: John Wiley & Sons.
43. Team, L.C. *Convergence and Mesh Independence Study*. 2016 [cited 2016 January]; Available from: <http://www.computationalfluidynamics.com.au/convergence-and-mesh-independent-study/>.
44. Carslaw, H.S. and J.C. Jaeger, *Conduction of heat in solids*. Oxford: Clarendon Press, 1959, 2nd ed., 1959.
45. Shepard, S. and J. Lhota. *Flash thermography modeling based on IR camera noise characteristics*. in *REVIEW OF PROGRESS IN QUANTITATIVE NONDESTRUCTIVE EVALUATION*:

- 34th Annual Review of Progress in Quantitative Nondestructive Evaluation*. 2008. AIP Publishing.
46. Almond, D.P. and S. Lau, *Defect sizing by transient thermography. I. An analytical treatment*. Journal of Physics D: Applied Physics, 1994. **27**(5): p. 1063.
 47. Saintey, M.B. and D.P. Almond, *Defect sizing by transient thermography. II. A numerical treatment*. Journal of Physics D: Applied Physics, 1995. **28**(12): p. 2539.
 48. Shepard, S., et al. *Materials characterization using reconstructed thermographic data*. in *AIP Conference Proceedings*. 2003. IOP INSTITUTE OF PHYSICS PUBLISHING LTD.
 49. Castanedo, C.I., *Quantitative subsurface defect evaluation by pulsed phase thermography: depth retrieval with the phase*. 2005, Université Laval.
 50. Kobayashi, K. and N. Banthia, *Corrosion detection in reinforced concrete using induction heating and infrared thermography*. Journal of Civil Structural Health Monitoring, 2011. **1**(1-2): p. 25-35.
 51. Shepard, S.M. and M.F. Beemer. *Advances in thermographic signal reconstruction*. in *SPIE Sensing Technology+ Applications*. 2015. International Society for Optics and Photonics.
 52. Shepard, S., M. Frendberg, and Y. Hou, *Characterization of Full-Range Time Evolution in Active Thermography*.
 53. Shepard, S., *Approaches to Data Reduction, Visualization and Analysis in Thermographic Signal Reconstruction*.
 54. Wetsel Jr, G.C. and F.A. McDonald, *Resolution and definition in photothermal imaging*. Journal of applied physics, 1984. **56**(11): p. 3081-3085.
 55. Instruments, F. *FLIR TG165 Imaging IR Thermometer Key Features*. 2016 [cited 2015 June]; Available from: <http://www.flir.com.au/uploadedFiles/Instruments/Products/TG165/FLIR-TG165-Brochure-EN.pdf>.
 56. Edge, E. *Thermal Properties of Metals, Conductivity, Thermal Expansion, Specific Heat*. 2000-2016 [cited 2014 December]; Available from: http://www.engineersedge.com/properties_of_metals.htm.
 57. Peabody, H., *Introduction to FEMAP for Thermal Model Generation*, in *Thermal and Fluids Analysis Workshop*, Swales Aerospace, 2006.
 58. Mundrey, J.S., *A. Iron and Steel & B. Rails*, in *Railway Track Engineering, Fourth Edition*. 2009, McGraw Hill Professional, Access Engineering.
 59. Alberta, U.o. *FEM Convergence Testing*. 2010 [cited 2015 October]; Available from: <http://www.mece.ualberta.ca/tutorials/ansys/AU/Converge/Converge.html>.

60. Mississippi Road Information, *RAIL SPECIFICATIONS*. 2007 [cited October 2016]; Available from: www.icrr.net/rails.htm.
61. Nordco Rail Services and Inspection Technologies (NRS&IT), 2016. *Rail Flaw Defects Identification Handbook*. Wisconsin: Nordco. p23-24.

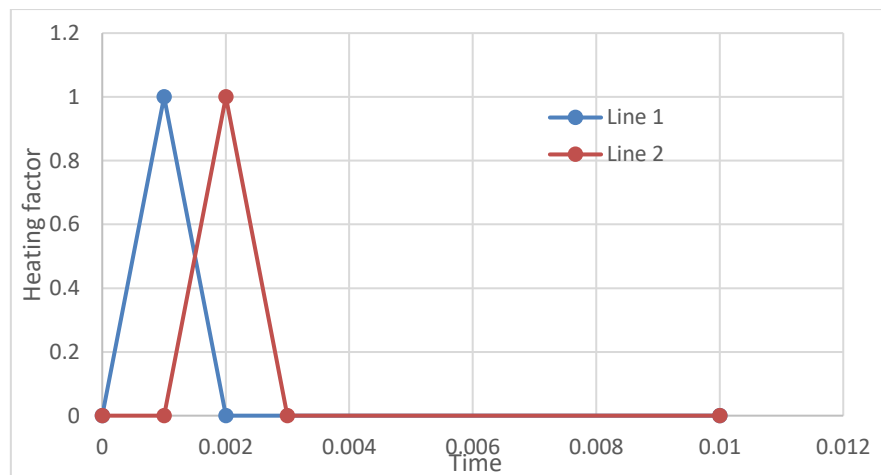
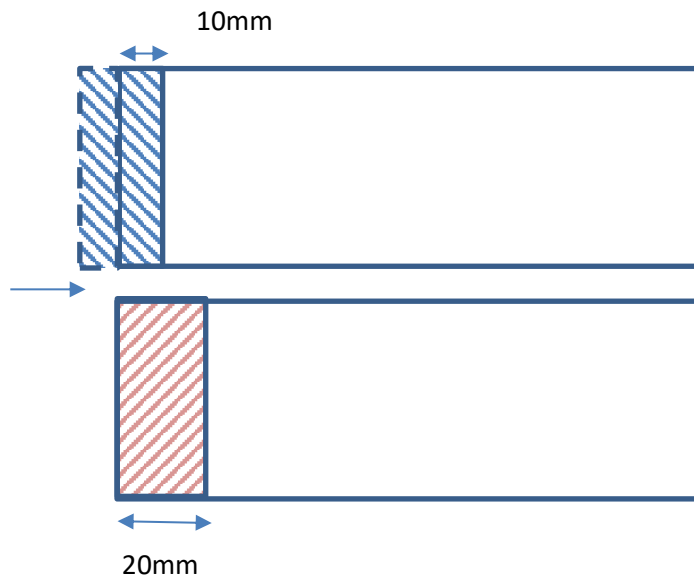
Appendix A: Sample calculation of moving heat source speed

Example 1:

Model Setup: 6.3.1 10mm heating strip – 36km/hr

Line strip thickness – 10mm

Heating duration on each strip – 2ms



The time at which maximum heating factor occur at mid-point of the 'line 2' heating and the mid-point of the second last line heating was used as a reference point.

Final time at mid-point 2 = $120\text{mm}/10\text{mm} \times 0.001\text{s} = 0.012\text{s}$

Total time from mid-point 1 to 2 = $0.012\text{s} - 0.002\text{s} = 0.01\text{s}$

Total distance between mid-point 1 and 2 = $120\text{mm} - 10\text{mm} - 10\text{mm} = 100\text{mm}$

Travel speed in mm/s = $100\text{mm}/0.01\text{s} = 10000\text{ mm/s}$

Also equivalent to 36 km/hr.

Example 2:

Model Setup: 6.3.2 15mm heating strip – 54km/hr

Line strip thickness – 15mm

Heating duration on each strip – 2ms

Note that the setup is similar to Example 1, the only difference is the size of the line strip.

Final time at mid-point 2 = $120\text{mm}/15\text{mm} \times 0.001\text{s} = 0.008\text{s}$

Total time from mid-point 1 to 2 = $0.008\text{s} - 0.002\text{s} = 0.006\text{s}$

Total distance between mid-point 1 and 2 = $120\text{mm} - 15\text{mm} - 15\text{mm} = 90\text{mm}$

Travel speed in mm/s = $90\text{mm}/0.006\text{s} = 15000\text{ mm/s}$

Also equivalent to 54 km/hr.

Appendix B: Minimum Energy

According to Equation 3.16,

$$W > \frac{KLT_{res}}{\alpha}$$

This equation determines the minimum amount of input energy required to result in a temperature contrast comparable or greater than the temperature resolution of a commercial infrared camera.

In this study, the following properties were used.

K, thermal conductivity = 64 W/m.K

L, sample thickness (maximum) = 8 mm

T_{res}, temperature resolution = 0.1°C

α, thermal diffusivity = 1.4057 x 10⁻⁵

Therefore,

$$W > \frac{64 \times 8 \times 10^{-3} \times 0.1}{1.4057 \times 10^{-5}} = 3642.31 \text{ J}$$

The minimum required input energy is 3642.31 J and can be approximated to 4000 J.

Appendix C: MATLAB Script

Second order peak derivative method

```
%%%%%%%%%%%%%%%%%%%%%%%%%%%%%%%%%%%%%%%%%%%%%%%%%%%%%%%%%%%%%%%%%%%%%%%%%%%%%%
% LAST UPDATED AND VERIFIED ON 6/1/2016
%%%%%%%%%%%%%%%%%%%%%%%%%%%%%%%%%%%%%%%%%%%%%%%%%%%%%%%%%%%%%%%%%%%%%%%%%%%%%%

% Created by Yi Chin Tan
% Measuring defect depth across a plate
% Lateral dimension of defect not defined in this context

clear variables
clear all
close all
clc

% DESCRIPTION %
% the purpose of this m.file is to calculate local thickness of a material
% based on the surface temperature data

% The polynomial curve fitting method was applied

% Excel file - .xlsx
% MOD file - .MOD
% NX file - .prt
% Temperature output data from FEMAP

data = xlsread('<insert file name>.xlsx'); % input temperature file
coordinate = xlsread('<insert file name>.xlsx'); % input coordinate file

% %%%%%%%%%%%%%%%%%%%%%%%%%%%%%%%%%%%%%%%%%%%%%%%%%%%%%%%%%%%%%%%%%%%%%%%%%%%
% if there is an extra file due to space limit
% temp_read_2 = xlsread('8mm calib temp (2).xlsx');
% n = input('n = ');
% %%%%%%%%%%%%%%%%%%%%%%%%%%%%%%%%%%%%%%%%%%%%%%%%%%%%%%%%%%%%%%%%%%%%%%%%%%%

% Timestep chosen here is similar to the selected timestep from FEMAP
% analysis setup ie. time interval of 0.001s or 0.01s etc
% timestep value can be changed in model setup (FEMAP)

int = input('timestep interval = ');
final = input('final time value (hint:5.01/5.001; depending on timestep
interval) = ');
timestep = 0:int:final;
plate_thick = input('input plate thickness to closest mm = ');

% theory based time domain
if plate_thick > 7;
    time_start = 0.228; % 0.228 or 0.005
    time_end = 1.45; % 1.45s or final-int

    % special case for if defect thickness much smaller
elseif plate_thick == 4
    time_start = 0.057;
    time_end = 1.821;
elseif plate_thick == 2
    time_start = 0.014;
    time_end = 0.455;
```

```

else
    time_start = 0.005;
    time_end = 0.1
end

% time_start (0.02s) can measure up to 0.001m thickness;
% time_end (0.15s) can measure up to 0.0026m thickness;
% time_start = 0.2;    %time where you are interested away from maximum
% referenced from a Fourier number as suggested from article

% time_end = 0.15 (example)
% time where you want to end your region of interested, usually fixed for
% different thickness of plate**
% time_end = input('input end time of region of interest = ')

ts1 = time_start/(timestep(2)-timestep(1)); %different timestep interval
may affect the location
%of the time selected. this is because, it is the time region that is
%interested of, not the timestep number
tel = time_end/(timestep(2)-timestep(1));

node = zeros (1,1); % default
% writing the number of coordinates extracted from the analysis
dn = length(coordinate);

%%%%%%%%%%%%%%%%%%%%%%%%%%%%%%%%%%%%%%%%%%%%%%%%%%%%%%%%%%%%%%%%%%%%%%%%
%if theres an extra file
[qq, q] = size(data);
ans = find(data(:,1) == data(1,1));
pp = qq/(ans(2)-1);
pp = round(pp);
%finding how many times the a full set of data repeats
%%%%%%%%%%%%%%%%%%%%%%%%%%%%%%%%%%%%%%%%%%%%%%%%%%%%%%%%%%%%%%%%%%%%%%%%

% Re-organising data into arrays
% for i=1:1502 ; % looping for 1502 output data sets
for i = 1:pp
    for j=i+((dn+1)*(i-1)) ; % extracting data for every nodes
        for z=1:1:dn ; % listing all the nodes with their results in the
            same matrix
                node(z,i) = data (j+(z-1),2)-25 ;% node represents each node's
data in defect area
            end
        end
    end
end

% % % %%%%%%%%%%%%%%%%%%%%%%%%%%%%%%%%%%%%%%%%%%%%%%%%%%%%%%%%%%%%%%%%%%%%%%%%%
% % %
% % % %loading the second file into the node system:
% % % [ee,e]=size(temp_read_2);
% % % ans1 = find(temp_read_2(:,1) == temp_read_2(1,1));
% % % jj = ee/(ans(2)-1);
% % % jj = round (jj);
% % %
% % %
% % % % for iii = pp:1:n
% % % for i = 1:jj

```

```

% % %      for j=i+((dn+1)*(i-1)) ; % extracting data for every nodes
% % %
% % %      for z=1:1:dn ; % listing all the nodes with their results
in the same matrix
% % % %      disp('test')
% % %      node2(z,i) = temp_read_2(j+(z-1),2) - 25;% node
represents each node's data in defect area
% % % %      disp('gsdgsdgsdg')
% % %      end
% % %      end
% % %      end
% % % % end

% % node = zeros(dn, n);
% % node(:,1:pp) = node1(:,:);
% % node(:, pp+1:n) = node2(:,:);
%%%%%%%%%%%%%%%%%%%%%%%%%%%%%%%%%%%%%%%%%%%%%%%%%%%%%%%%%%%%%%%%%%%%%%%%

%%%%%%%%%%%%%%%%%%%%%%%%%%%%%%%%%%%%%%%%%%%%%%%%%%%%%%%%%%%%%%%%%%%%%%%%
% Looking for the time at which maximum temperature is achieved
% This is to compute the time at which cooling begins, hence observing only
% the cooling period

[rr,cc]= size(node);
% rr is the number of rows, cc is the number of columns

% locating the max temp and its respective position for each nodes
for counter1 = 1:rr
    [A(counter1,1),A(counter1,2)] = max(node(counter1,:));
    name{counter1} = ['Node ' num2str(counter1)];
    name2{counter1} = ['poly' num2str(counter1)];
end

% making the position of max temp as an seperate 'array' variable
array = A(:,2);

% finding the max temp achieved in all cases - for later use
maxtemp = max(A(:,1));

% creating the array of data to show the location of maximum temperature
% occurred for different nodes up to the last data
B7 = zeros(rr,cc+ts1);
for counter4 = 1:length(array)
    B8 = node(counter4 , array(counter4):end);
    B7(counter4 , 1:length(B8)) = B8;
end

% picking data between the desired region
% ts1 is a literature value suggesting that the window frame
% should be taken after that amount of transient cooling
B9 = B7(:, ts1:tel);

%%%%%%%%%%%%%%%%%%%%%%%%%%%%%%%%%%%%%%%%%%%%%%%%%%%%%%%%%%%%%%%%%%%%%%%%
data_node = node(:, :);

% plotting the raw data
figure % GRAPH 1
plot(timestep(:), data_node,'LineWidth',2)
box off; grid on

```

```

title('Graph for Raw Temperature vs Time')
xlabel('Time')
ylabel('Temperature')
% legend(name)
figure

%%
% Converting data into logarithmic form
%%%%%%%%%%%%%%%%%%%%%%%%%%%%%%%%%%%%%%%%%%%%%%%%%%%%%%%%%%%%%%%%%%%%%%%%
% only extracting part where maximum temperature begins %
%%%%%%%%%%%%%%%%%%%%%%%%%%%%%%%%%%%%%%%%%%%%%%%%%%%%%%%%%%%%%%%%%%%%%%%%

% timestep 0 now begins at where the maximum temperature starts
% timestep = 0:int:(final-((B6-1)*int)); % timestep has grown smaller, as
we have
% now removed B6 numbers of data due to occurrence of max temp
log_datanode = log(B9);

times = log(timestep)';

times1 = times(tsl:tel); % do not need to translate the position of time
because
% since the temperature data has been brought forward to time '0', hence
% there is no need to move the 'time'

% Alternatively, if the first value of heating is of interest, then
plotting it will
% just be adding one more number in

%%
% plotting in the logarithmic form
% GRAPH 2
plot(times1, log_datanode, 'LineWidth',2)
box off; grid on
title('Logarithmic form of Temperature and time')
xlabel('Log Time')
ylabel('Log Temperature')
% legend(name)
figure

%%
%%%%%%%%%%%%%%%%%%%%%%%%%%%%%%%%%%%%%%%%%%%%%%%%%%%%%%%%%%%%%%%%%%%%%%%%
% Polynomial Curve Fitting Method %
%%%%%%%%%%%%%%%%%%%%%%%%%%%%%%%%%%%%%%%%%%%%%%%%%%%%%%%%%%%%%%%%%%%%%%%%

log_datanode1 = log_datanode';

% Using polynomial to the power of 9 fitting to curve fit the region of the
% graph where cooling is expected to commence

% First and Second order derivative of the logarithmic terms
for counter2 = 1:rr
    eval(['poly' num2str(counter2) '= fit(times1,
log_datanode1(:,counter2),'poly9');']);
    eval(['eqn = poly' num2str(counter2) ]);

    % first derivative and second derivative
    [dev_poly1(:,counter2),dev_poly2(:,counter2)] = differentiate (eqn,
times1); % Differentiating the 1st node two times;

```

```

end

%%
% Comparing the first order derivative
% GRAPH 3
plot (times1, dev_poly1,'LineWidth',2)
box off; grid on
title('First order derivative of the log temperature and log time graph')
xlabel('Log Time')
ylabel('Log Temperature')

% Comparing the second order derivative
% GRAPH 4
figure
plot (times1, dev_poly2, 'LineWidth',2) % graph 4
box off; grid on
title('Second order derivative of the log temperature and log time graph')
xlabel('Log Time')
ylabel('Log Temperature')

% using the stop technique
% selecting points where the first order derivative is larger than 1
% % % [length1, width] = size(dev_poly1);
% % % stop = zeros(1, width);
% % % for gg = 1:width
% % %     ans = find(dev_poly1(:,gg)>0);
% % %     stop(gg) = ans(1);
% % % end

%% Finding the time at which this first maximum occurs
for counter3 = 1:rr
    counter = 1;
    grad = dev_poly2(counter+1,counter3) - dev_poly2(counter, counter3);
    % looking for a point where the gradient changes from -ve to a
    % +ve. this is the minimum point (need not use the 'stop' idea
    if grad < 0
        while grad < 0
            counter = counter + 1;
            grad = dev_poly2(counter+1,counter3) - dev_poly2(counter,
counter3);
            if grad > 0
                pos1(counter3) = counter;

% % %
% % %
% % % while grad>0
% % %     grad = dev_poly2(counter+1,counter3) -
dev_poly2(counter, counter3);
% % %     if grad < 0
% % %
% % % while grad < 0
% % %     grad = dev_poly2(counter+1,counter3) -
dev_poly2(counter, counter3);
% % %     if grad > 0
% % %         end1(counter3)= counter;
% % %     break
% % %     end
% % %     end
% % %     end
% % %     end

```

```

        break
    end
end
elseif grad > 0

    while grad > 0
        counter = counter + 1;
        grad = dev_poly2(counter+1,counter3) - dev_poly2(counter,
counter3);

        if grad < 0
            pos1(counter3) = counter;

%%
%%
%% while grad<0
%% grad = dev_poly2(counter+1,counter3) -
dev_poly2(counter, counter3);
%% if grad > 0
%%
%% while grad > 0
%% grad = dev_poly2(counter+1,counter3) -
dev_poly2(counter, counter3);
%% if grad < 0
%%
%% while grad < 0
%% grad = dev_poly2(counter+1,counter3) -
dev_poly2(counter, counter3);
%% if gradn > 0
%% endl(counter3) = counter;
%% break
%% end
%% end
%% end
%% end
%% end
%% end
break
    end
end
end

[value(counter3),pos(counter3)] =
max(dev_poly2(pos1(counter3):end,counter3));

% the calculation for material thickness only work for after heat
% applied
maxx(counter3) = (pos(counter3)*int) + (pos1(counter3)*int) +
time_start;%+ array(counter3)*int - 0.002;
end

% Material properties (all in SI units)
thermal_cond = 64;
heat_cap = 580;
density = 7850;

% Calculating the thermal diffusivity, alpha
therm_diff = thermal_cond/(density*heat_cap);

```



```

% This equation from Steven M. Shepard et. al., from 'Measurement limits in
% flash thermography' is deduced to be able to measure either the depth or
% diffusivity of the material. In other words, measuring the local depth of
% the material will be able to suggest whether a material has experienced
% thinning or so.

% Suggestion on the t* (max_timestep) value obtained from maximum of second
% order derivative

mat_thickness1 = sqrt(pi*therm_diff*maxx);
mat_thickness2 = mat_thickness1*1000;
mat_thickness = roundn(mat_thickness2, -2);

% assume relative shifting
shift = mode(mat_thickness) - plate_thick;
for pp = 1: length(mat_thickness)
    if mat_thickness(pp) > plate_thick
        mat_thickness_mod(pp) = plate_thick;
    else
        mat_thickness_mod(pp) = mat_thickness (pp) - shift;
    end
end

%%%
%sorting the material thickness based on nodal position
%sorting the coordinate from the excel file
m = length(coordinate);
sel_coord = input('coordinate system input = ','s');

if sel_coord == 'y'
    sel_coord = 5;
    ques = 2;
else sel_coord == 'x'
    sel_coord = 4;
    ques = 1;
end

coord = zeros(m,2);
for i = 1:m
    coord(i,1) = coordinate(i,1);
    coord(i,2) = coordinate(i,sel_coord);
    coord(i,3) = mat_thickness(1,i);
    coord(i,4) = mat_thickness_mod(1,i);
end

% putting them in order
[~, index2] = sort(coord(:,2));
sort_coord = coord(index2,:);

figure
% GRAPH 5
plot(sort_coord(:,2), sort_coord(:,3), '-x')
title('Material thickness variation across the plate')
xlabel('Position')
ylabel('Approximated Thickness')

% GRAPH 6

```

```
figure
plot(sort_coord(:,2), sort_coord(:,4), '-x')
title('Relative thickness')
xlabel('Position')
ylabel('Approximated Thickness')
```

Full Width Half Maximum (FWHM)

% measuring the lateral dimension of defect from the top side of the plate
% defect is located at the underside of the plate

% Created by Yi Chin Tan
% Last Modified: 7/4/2016

```
format short
cl = input('do you want to close all plots? (y-Yes, n-No)', 's');
if cl == 'y'
    close all
    clear variables
    clear all
    clc

else cl == 'n'
    clear variables
    clear all

end

% reading the coordinates and temperature values of the nodes selected
coordinate_read = xlsread('chap 522 test coord.xlsx');
temp_read = xlsread('chap 522 test temp.xlsx');

% % % % %%%%%%%%%%%%%%%%%%%%%%%%%%%%%%%%%%%%%%%%%%%%%%%%%%%%%%%%%%%%%%%%%%%%%%%%%%y
%%%%%%%%%%%%%%%%%%%%%%%%%%%%%%%%%%%%%%%%%%%%%%%%%%%%%%%%%%%%%%%%%%%%%%%%%
% % % % %if there is an extra file due to space limit
% % % % temp_read_2 = xlsread('8mm ncalib temp (2).xlsx');
% % % % %%%%%%%%%%%%%%%%%%%%%%%%%%%%%%%%%%%%%%%%%%%%%%%%%%%%%%%%%%%%%%%%%%%%%%%%%%
%%%%%%%%%%%%%%%%%%%%%%%%%%%%%%%%%%%%%%%%%%%%%%%%%%%%%%%%%%%%%%%%%%%%%%%%%

% n is the number of iterations/results collected based on timestep
% selected
% n = 2002;
n = input('n = ');
heating = input('heating type? 1 - stationary, 2 - line = ');
delay = 0.001;
% input('please input delay = ');
int = 0.001;
% this is the time increment interval in 'Analyses'
% input('please input analysis time interval = ');
line1 = 5;
line = line1*1e-3;
% input('please input line thickness (0.005m) = ');

delay = delay/int;
for input_time = [<range of input time>];%i.e.
150,160,170,180,190,200,220,240,260,280];
% input_time = input('timestep number = ');
input_time = input_time + 2;

% m is the number of nodes selected to be investigated
m = size (coordinate_read);
m = m(1,1);

% pre-setting zeros matrix to speed up iteration and data extraction
node = zeros(m,1);
```

```

%%%%%%%%%%%%%%%%%%%%%%%%%%%%%%%%%%%%%%%%%%%%%%%%%%%%%%%%%%%%%%%%%%%%%%%%
%if theres an extra file
[qq, q]=size(temp_read);
ans = find(temp_read(:,1) == temp_read(1,1));
pp = qq/(ans(2)-1);
pp = round(pp);
%%%%%%%%%%%%%%%%%%%%%%%%%%%%%%%%%%%%%%%%%%%%%%%%%%%%%%%%%%%%%%%%%%%%%%%%

for i = 1:pp
    for j=i+((m+1)*(i-1)) ; % extracting data for every nodes
        for z=1:1:m ; % listing all the nodes with their results in the
same matrix
            node(z,i) = temp_read(j+(z-1),2) ;% node represents each node's
data in defect area
        end
    end
end

% % % % %%%%%%%%%%%%%%%%%%%%%%%%%%%%%%%%%%%%%%%%%%%%%%%%%%%%%%%%%%%%%%%%%%%%%%%%%
%%%%%%%%%%%%%%%%%%%%%%%%%%%%%%%%%%%%%%%%%%%%%%%%%%%%%%%%%%%%%%%%%%%%%%%%
% % % % %loading the second file into the node system:
% % % % [ee,e]=size(temp_read_2);
% % % % ans1 = find(temp_read_2(:,1) == temp_read_2(1,1));
% % % % jj = ee/(ans(2)-1);
% % % % jj = round (jj);
% % % %
% % % % % for iii = pp:1:n
% % % % for i = 1:jj
% % % %     for j=i+((m+1)*(i-1)) ; % extracting data for every nodes
% % % %
% % % %         for z=1:1:m ; % listing all the nodes with their
results in the same matrix
% % % % %         disp('test')
% % % % %         node2(z,i) = temp_read_2(j+(z-1),2) ;% node
represents each node's data in defect area
% % % % %         disp('gsdgsdgsdg')
% % % % %     end
% % % % end
% % % % end
% % % % % end
% % % %
% % % % node = zeros(m, n);
% % % % node(:,1:pp) = node1(:,,:);
% % % % node(:, pp+1:n) = node2(:,,:);
% % % % %%%%%%%%%%%%%%%%%%%%%%%%%%%%%%%%%%%%%%%%%%%%%%%%%%%%%%%%%%%%%%%%%%%%%%%%%

%%
% establishing the coordinate position of each nodes selected

% pre-setting zeros
coord = zeros(m,n+2);

% restating the nodes
for i = 1:m
    coord(i,1) = coordinate_read(i, 1);
end

% re-stating the coordinate system
for i = 1:m

```

```

        coord(i,2) = coordinate_read(i,4);
    end

    a = size(node);
    aa = a(1,1);
    plotnode = zeros(aa,1);

    %%
    % allocating nodal and coordinate with respect to temperature results
    for i=1:m
        coord(i,(3:end)) = node(i,:);
    end

    % sorting out the nodes

    [~, index2] = sort(coord(:,2));
    sort_temp = coord(index2,:);

    % sort_temp = sort_temp (1:2:end, :);
    % each node is represented by its own coordinates and temperature in order

    %% GRAPH ONE
    % plotting the temperature with respect to the coordinate position
    figure
    plot(sort_temp(:,2), sort_temp(:, input_time), '*-')
    box off
    grid on
    title('Temperature response over spatial domain')
    xlabel('Coordinate position on model')
    ylabel('Temperature responses')
    hold on

    % resp = input('Do you want to enter a new timestep? (y-Yes, n-No) ','s');
    resp = 'n';
    if resp == 'y';
        while resp == 'y'
            input_time = input('please input timestep number again = ');
            input_time = input_time + 2;

            figure
            plot(sort_temp(:,2), sort_temp(:, input_time), '*-')
            box off
            grid on
            title('Temperature response over spatial domain')
            xlabel('Coordinate position on model')
            ylabel('Temperature responses')
            legend('name')
            hold on

            % contrast = max(sort_temp(:,input_time)) - min(sort_temp(:,
            input_time))
            resp = input('Do you want to enter a new timestep again? (y-Yes, n-
            No) ','s');
        end
    else resp == 'n'
        input_time = input_time;
    end
end

```

```

if heating == 1;
% for a stationary heating scenario
sort_temp(:,3) = sort_temp(:, input_time);
% else
%%%% %%% %%%
% % including the time delay here
%     s = size(sort_temp);
%     sort_temp(1,3) = sort_temp(1, input_time);
%     for ii = 1:(s(1,1) - 1)
%         l(ii) = sort_temp(ii+1,2) - sort_temp(1,2);
%         nn = floor( l(ii)/line );
%         sort_temp1(ii+1,3) = sort_temp(ii+1, input_time +
(nn*delay) );
%     end

else
% % %           This is for the end point heating scan
% % % including the TIME DELAY here
s = size(sort_temp);
sort_temp(end,3) = sort_temp(end, input_time);
l = zeros(s(1,1) , 1 );
for ii = 1:(s(1,1) - 1)
    l(end-ii) = abs(sort_temp(end-ii,2) - sort_temp(end,2));

    % during line scanning, a same line of action is affected
    % as line scan runs across. this set of codes serve to average
    % the temperature response at these lines
    if rem(l(end-ii), line) == 0
        nn = floor( l(end-ii)/line );
        sort_temp(end-ii,3) = (sort_temp(end-ii, input_time +
((nn-1)*delay)) + sort_temp(end-ii, input_time + (nn*delay)))/2;
    else
        nn = floor( l(end-ii)/line );
        sort_temp(end-ii,3) = sort_temp(end-ii, input_time +
(nn*delay) );
    end

% %           nn = floor( l(end-ii)/line );
% %           sort_temp(end-ii,3) = sort_temp(end-ii, input_time +
(nn*delay) );
end
end

%%%%%%%%%%%%%%%%%%%%%%%%%%%%%%%%%%%%%%%%%%%%%%%%%%%%%%%%%%%%%%%%%%%%%%%%
% removing line edges of heating strip %
%%%%%%%%%%%%%%%%%%%%%%%%%%%%%%%%%%%%%%%%%%%%%%%%%%%%%%%%%%%%%%%%%%%%%%%%
if heating == 2;
[g1,g2] = size(sort_temp);

sort_temp1(1,:) = sort_temp(2,:);
gg = 2;
for hh = 3:g1
    if rem(sort_temp(hh,2)*1e3, line1)~=0
        sort_temp1(gg,:) = sort_temp(hh,:);
        gg = gg + 1;
    else
        gg = gg;
    end
end
clear sort_temp

```

```

sort_temp = sort_temp1;
else
    sort_temp = sort_temp(2:end-1,:);
end

figure
plot(AA, BB1, '*') % Graph 2
% ylim([min(sort_temp(:,3))-1 , 10+min(sort_temp(:,3))]);
box off
grid on
title('Temperature response over spatial domain (TIME DELAY REMOVED)')
xlabel('Coordinate position on model')
ylabel('Temperature responses')
hold on
%% %%%%%%%%%%%%%%%%%%%%%%%%%%%%%%%%%%%%%%%%%%%%%%%%%%%%%%%%%%%%%%%%%%%%%%%%%
%%
% cubic spline interpolation
x = AA;
y = BB1;
maxy = max(y);
f = find(y==maxy);
cp1 = x(f);
cp = median(cp1);
y1= y./maxy; %normalising the results with the max value
ydatawr(:,1) = y1;
ydatawr(:,2) = x;
newFit1=find(x>= cp);
newFit2=find(x < cp);
c1 = ydatawr(min(newFit1):max(newFit1),:);
c2 = ydatawr(min(newFit2):max(newFit2),:);

% xx = (max(ydatawr2(:,1)) + min(ydatawr2(:,1)))/2 ;
xx = (1 + min(c1(:,1)))/2 ;
yy = (1 + min(c2(:,1)))/2 ;

%% %%%%%%%%%%%%%%%%%%%%%%%%%%%%%%%%%%%%%%%%%%%%%%%%%%%%%%%%%%%%%%%%%%%%%%%%%
% linear interpolation technique

%%% first half of curve %%%

% (higher end - does not require the method in lower end)
% because the first minimum point will be located whereas the lower end
% will locate ALL the minimum point

% finding the minimum point
% using the idea of needing at least 3 points to have a gradient as small
% as 1e-4, to be considered a flat baseline

% finding and isolating the maximum points for a start
% rounding up numbers to locate maximums
cc11 = round(c1,4);

% finding the location/position of the maximum point
findmax = find(cc11 == max(cc11(:,1)));
ok = max(findmax); % default k value to begin with

% NOTE: this is usually 1e-4 for stationary, and 1e-3 for line moving
% NOTE: the difference is usually 3 nodes, now change to 2 nodes for
% line
% limit and lim_pt varies for different heating approach, this is to

```

```

% satisfy the baseline curve
if heating == 1
    limit = 1e-4;
    lim_pt = 3;
% elseif input_time < 100 % early time observation will show wiggles at the
tails
%     limit = 5e-3;
% % limit = 1e-4;
%     lim_pt = 3;
else
    limit = 1e-4;
    lim_pt = 1;
end

% k = 1; % default
for k = ok+2:length(c1)-lim_pt % '+2' is to begin gradient measurements
away
    % from the first and second maximum node
    if abs(c1(k+lim_pt,1)-c1(k,1)) >= limit
        %
        k = k + 1;
        slope0 = 0;
    else abs(c1(k+lim_pt,1)-c1(k,1)) < limit
        slope0 = k;
        break
    end
end

if slope0 == 0
    modil = 0;
    midxx = NaN;
else
    % performing interpolation within a selected region
    if heating == 1
        slope0 = slope0 + 3;
    else
        slope0 = slope0 + 1;
    end

    midxx = (1+c1(slope0,1))/2;
    dif_pt = c1(ok:slope0,1) - midxx;

    %%%%%%%%%%%%%%%%%%%%%%%%%%%%%%%%%%%%%%%%%%%%%%%%%%%%%%%%%%%%%
    % looking for the 2 points that is bounding the midxx and midyy value
    for i=1:length(dif_pt)
        if dif_pt(1)>0
            if dif_pt(i)>0
                first = i;
            else
                second = first + 1;
                break
            end
        elseif dif_pt(1)<0
            if dif_pt(i)<0
                first = i;
            else
                second = first + 1;
                break
            end
        end
    end
end

```



```

end
%%%%%%%%%%%%%%%%%%%%%%%%%%%%%%%%%%%%%%%%%%%%%%%%%%%%%%%%%%%%%%%%%%%%%%%%%%%%%%
c11 = c1(ok:slope0,:);

modi1 = interp1(c11(first:second,1),c11(first:second,2),midxx);
end

%%%%%% second half of curve (lower end) %%%%%

% checking the need to perform this run if first half of curve failed
if modi1 ~= 0;
% finding and isolating the maximum points for a start
cc22 = round(c2,4);
% finding the location/position of the maximum point
findmax_2 = find(cc22 == max(cc22(:,1)));
ok2 = min(findmax_2); % default k value to begin with

kk = ok2-2; % '-2' is to begin gradient measurements away
               % from the first and second maximum node

% if there is a flat curve at the peak, then the if statement will
% check for it
% ideally for large defect size
if abs(c2(kk-lim_pt,1) - c2(kk,1)) >= limit
    while abs(c2(kk-lim_pt,1) - c2(kk,1)) >= limit
        kk = kk - 1;
        slope00 = 0;
        if kk-lim_pt == 0
            slope00 = 0;
            modi2 = 0;
            FWHM2 = NaN;
            disp('test')
            break
        elseif abs(c2(kk-lim_pt,1) - c2(kk,1)) < limit
            slope00 = kk;
            break
        end
    end
    %
    %
    %
    end
end

else
    kk = kk - 1;
    disp('abc')
    while abs(c2(kk-lim_pt,1) - c2(kk,1)) < limit
        kk = kk - 1;
        slope00 = 0;
        if abs(c2(kk-lim_pt,1) - c2(kk,1)) >= limit
            %%%%%%%%%%%%%%%%%%%%%%%%%%%%%%%%%%%%%%%%%%%%%%%%%%%%%%%%%%%%%%%%%%%%%%%%%%%%%%%
            while abs(c2(kk-lim_pt,1) - c2(kk,1)) >= limit
                disp('check 2')
                kk = kk - 1;
                slope00 = 0;
                if kk-lim_pt == 0
                    slope00 = 0;
                    break
                elseif abs(c2(kk-lim_pt,1) - c2(kk,1)) <
limit
                    slope00 = kk;
                    break
                end
            end
        end
    end
end

```

```

                                end
                                %%%%%%%%%%%%%%%%%%%%%%%%%%%%%%%%%%%%%%%%%%%%%%%%%%%%%%%%%%%%%%%%%%%%%%%%%
                                break
%                                else
                                end
                                end
                                end
                                % c22 = round(c2,4); % rounding up the numbers to obtain a get all the
                                minimum value
                                % a1 = find(c22 == min(c22(:,1)));
                                % almax = max(a1);

                                if slope00 == 0
                                    modi2 = 0;
                                    FWHM2 = NaN;
                                else
                                    midyy = midxx;
%                                    midyy = (1+c2(slope0,1))/2; % uses slope0 instead of slope00
because                                % they should be the same

%%%%%%%%%%%%%%%%%%%%%%%%%%%%%%%%%%%%%%%%%%%%%%%%%%%%%%%%%%%%%%%%%%%%%%%%
                                dif_pt2 = c2(slope00:ok2,1) - midyy;
                                % looking for the 2 points that is bounding the midxx and midyy value
                                for i=1:length(dif_pt2)
                                    if dif_pt2(1)>0
                                        if dif_pt2(i)>0
                                            first1 = i;
                                        else
                                            second1 = first1 + 1;
                                        break
                                    end
                                elseif dif_pt2(1)<0
                                    if dif_pt2(i)<0
                                        first1 = i;
                                    else
                                        second1 = first1 + 1;
                                    break
                                end
                                end
                                end
                                %%%%%%%%%%%%%%%%%%%%%%%%%%%%%%%%%%%%%%%%%%%%%%%%%%%%%%%%%%%%%%%%%%%%%%%%%
                                cc2 = c2(slope00:ok2,:); %cc2 re-represent c2 for modi2 interpolation

                                modi2 =
                                interp1(cc2(first1:second1,1),cc2(first1:second1,2),midyy); %using the
                                original data w/o rounding
                                % modi2 = interp1(c2(slope00:ok2,1), ....
                                % Method 1 FWHM using linear interpolation
                                Fullw2 = abs(modi2 - modi1);
                                FWHM2 = round(Fullw2/1e-3, 2);
                                end
                                else
                                    FWHM2 = NaN;
                                    modi2 = NaN;
                                    midyy = NaN;
                                end
                                % contrast = max(sort_temp(:,input_time)) - min(sort_temp(:, input_time));

```

```

contrast = max(BB1) - min (BB1);
contrast = round(contrast, 3);
maxtemp = max(BB1);
%%%%%%%%%%%%%%%%%%%%%%%%%%%%%%%%%%%%%%%%%%%%%%%%%%%%%%%%%%%%%%%%%%%%%%%%
% table form
FWHM = [FWHM2; contrast; maxtemp; input_time-2];
Category = {'Linear Interpolation(mm)'; 'Contrast'; 'Maximum Temp'; 'Input
Time'};
TT = table(FWHM, 'RowNames', Category)

%%%%%%%%%%%%%%%%%%%%%%%%%%%%%%%%%%%%%%%%%%%%%%%%%%%%%%%%%%%%%%%%%%%%%%%%
% plottings
figure;
% s(1) = subplot(2,1,1);
% plot(xx1,sp11,xx2,sp22,xx,sp1,'o',yy,sp2,'o',midxx,
modi1,'*',midyy,modi2,'*')

s(2) = subplot(2,1,2);
plot(c1(:,1),c1(:,2),c2(:,1),c2(:,2),midxx, modi1,'*',midyy,modi2,'*')
% xx,sp1,'o',yy,sp2,'o',
% title(s(1),'Spline Interpolation')
title(s(2),'Original plot')
end

%%

```